MODELING AND SIMULATION OF A GENERIC HYPERSONIC VEHICLE

By

Shahriar Keshmiri

M.S., California State University, Los Angeles, 2004

Submitted to the graduate degree program in Aerospace Engineering and the Faculty of the Graduate School of the University of Kansas in partial fulfillment of the requirements for the degree of Doctor of Philosophy

_____

Chairperson: Dr. Richard Colgren

Committee members

_____

Dr. Ron Barrett

_____

Dr. David Downing

_____

Dr. Saeed Farokhi

_____

Dr. Weizhang Huang

_____

Dr. Eddy Lan

_____

Dr. Maj Mirmirani

_____

Dr. Ray Taghivi

Date defended: _____

The dissertation committee for Shahriar Keshmiri certifies that this is the approved version of the following dissertation:

MODELING AND SIMULATION OF A GENERIC HYPERSONIC VEHICLE

Committee members

_____
Chairperson: Dr. Richard Colgren

_____
Dr. Ron Barrett

_____
Dr. David Downing

_____
Dr. Saeed Farokhi

_____
Dr. Weizhang Huang

_____
Dr. Eddy Lan

_____
Dr. Maj Mirmirani

_____
Dr. Ray Taghivi

Date approved _____

Objectives

Horizontal take-off and horizontal landing hypersonic vehicles are a subject of great interest for future space launch missions. The ramjet/scramjet engine has the potential to enable a new class of spacecraft, missiles, and launch vehicles. This research covers the six degrees-of-freedom (6-DoF) modeling and simulation of a generic hypersonic vehicle (GHV) including a ramjet/scramjet propulsion system and an aerodynamic database. Newton's and Euler's equations are used to develop the longitudinal and the lateral-directional equations of motion. Analytical methods are employed to find the aerodynamic and propulsion models. The optimized trajectory for a generic hypersonic vehicle is developed exclusively for modeling and simulation purposes. The key contributions of this research are:

1. This model is the first complete and comprehensive 6-DoF simulation of an airbreathing hypersonic vehicle in the open literature. This model uses both traditional lookup tables as well as a unique approach using nonlinear analytical expressions. The developed simulation framework includes:
    A. The aerodynamic model is developed using wind tunnel experimental investigations and the best available CFD results from high fidelity and engineering level codes (STARS and APAS) uniquely integrated and verified. This technique in developing the aerodynamic model is used efficiently in a multidisciplinary manner to improve the CFD results for the generic hypersonic vehicle.
    B. The integrated aero-propulsion system model is the first analytical model for a generic hypersonic vehicle published including

regenerative cooling effects. The mathematical model of the aerodynamics and the propulsion system can be implemented easily within a conceptual design frame. The propulsion system model is applicable to hypersonic missiles, manned aircraft, unmanned aerial vehicle systems, and access-to-space systems.

C. The developed aerodynamic and propulsion systems for the generic hypersonic vehicle allow a trajectory to be optimized for the vehicle. The optimized trajectory for the generic hypersonic vehicle is uniquely designed including both thrust and aerodynamic forces rather than the simple point mass model usually seen in the open literature.

2. The linearized model of the generic hypersonic vehicle includes all pertinent lateral-directional states. This is the exception for published hypersonic vehicle models in the open literature. The combined longitudinal and lateral-directional models of the generic hypersonic vehicle can be used for control and navigation research.

3. The developed generic hypersonic vehicle model contains aerodynamic, propulsion, atmospheric, and mathematical modules. The modular structure of the simulation makes it easy to change any module efficiently according to the design criteria.

TABLE OF CONTENT

LIST OF FIGURE

LIST OF TABLES

Nomenclature

A.O.A	angle of attack, deg
alt.	altitude, ft
a. n.	normal acceleration
B	body frame coordinate
b	lateral-directional reference length, span, ft
c	longitudinal reference length, mean aerodynamic chord, ft
C_D	total drag coefficient, n. d.
C_{Da}	drag increment coefficient for basic vehicle, n. d.
$C_{D,\,da}$	drag increment coefficient for right elevon, n. d.
$C_{D,\,de}$	drag increment coefficient for left elevon, n. d.
$C_{D,\,dr}$	drag increment coefficient for rudder, n. d.
$C_{D,\,dc}$	drag increment coefficient for canard, n. d.
C_L	total lift coefficient for basic vehicle, n. d.
C_{La}	lift increment coefficient for basic vehicle, n. d.
$C_{L,\,da}$	lift increment coefficient for right elevon, n. d.
$C_{L,\,de}$	lift increment coefficient for left elevon, n. d.
$C_{L,\,dr}$	lift increment coefficient for rudder, n. d.
$C_{L,\,dc}$	lift increment coefficient for canard, n. d.
C_p	specific heat at constant pressure
C_Y	total side force, n. d.
C_{YB}	side force with sideslip derivative for basic vehicle, n. d.
$C_{Y,\,da}$	side force increment coefficient for right elevon, n. d.

$C_{Y,\,de}$	side force, increment coefficient for left elevon, n. d.
$C_{Y,\,dr}$	side force, increment coefficient for rudder, n. d.
C_l	total rolling moment coefficient, n. d.
C_{lB}	rolling moment with sideslip derivative for basic vehicle, n. d.
$C_{l,\,da}$	rolling moment increment for right elevon, n. d.
$C_{l,\,de}$	rolling moment increment for left elevon, n. d.
$C_{l,\,dr}$	rolling moment increment for rudder, n. d.
C_{lp}	rolling moment with roll rate dynamic derivative, n. d.
C_{lr}	rolling moment with yaw rate dynamic derivative, n. d.
C_m	total pitching moment coefficient, n. d.
C_{ma}	pitching moment increment coefficient for basic vehicle, n. d.
$C_{m,\,da}$	pitching moment increment coefficient for right elevon, n. d.
$C_{m,\,de}$	pitching moment increment coefficient for left elevon, n. d.
$C_{m,\,dr}$	pitching moment increment coefficient for rudder, n. d.
$C_{m,\,dc}$	pitching moment increment coefficient for canard, n. d.
C_{mq}	pitching moment pitch rate dynamic derivative, n. d.
C_n	total yawning moment coefficient, n. d.
$C_{n\beta}$	yawing moment with sideslip derivative for basic vehicle, n. d.
$C_{n,\,da}$	yawing moment increment coefficient for right elevon, n. d.
$C_{n,\,de}$	yawing moment increment coefficient for left elevon, n. d.
$C_{n,\,dr}$	yawing moment increment coefficient for rudder, n. d.
C_{np}	yawing moment roll rate dynamic derivative, n. d.
C_{nr}	yawing moment yaw rate dynamic derivative, n. d.

c.g.	vehicle center of gravity
DOF	degree of freedom
e	Oswald efficiency factor
e_s	span efficiency
f	fuel air ratio, n.d
F_{st}	Stoichiometry fuel air ratio
ii	isolator inlet
ie	isolator exit
h_c	film cooling mass flux
h	altitude
I_{sp}	engine specific impulse, sec.
I_{XX}, I_{YY}, I_{ZZ}	roll, pitch, and yaw moments of inertia respectively, slg-ft^2
M	Mach number, n.d.
Mol	molecular weight of dry air M = 0.0289644 kg/mol
n.a.	normal acceleration
n.d.	nondimensional
ne	nozzle exit
ni	nozzle inlet
P	roll rate
PLA	pilot lever angle, (0%~100%)
Pr	Prandtl number
Q	pitch rate
R	yaw rate

R	universal gas constant R = 8.31447 J/(mol·K)
R_A	aspect ratio
q	heat release (heat input)
q_{lim}	limiting heat addition
q/CpT_0	heat parameter
$\bar{q}$	dynamic pressure
S	stream thrust function
$S_{ref.}$	reference area, theoretical wing area , ft^2
SSTO	Single-Stage-To-Orbit
T	engine net thrust, lbf
thtl.	throttle angle
V	vehicle free stream velocity, ft/sec
W_0	initial value of vehicle weight, lb
W_{con}	weight of fuel consume
wrt (w.r.t.)	with respect to
$X_{cg.}$	longitudinal distance from momentum reference to vehicle c.g., positive
X, Y, Z	total aerodynamic forces (in body coordinate x, y, and z)
y	altitude
α	angle of attack, deg
β	sideslip angle, rad
φ	engine fuel ratio, n.d.

φ_{cs}	cooling equivalence ratio, n.d.
ϕ	Euler angle (deg)
θ	Euler angle (deg)
ψ	Euler angle (deg)
ψ	static temperature ratio
ω	flow turning
π_d	total pressure recovery
η_b	burner efficiency
η_d	kinetic energy efficiency
η_{fc}	film cooling efficiency
γ	ratio of specific heats
[E]	identity matrix
{q}	the rotation quaternion the rotational tensor of body frame wrt Earth frame
$\{Q^{BE}\}$	the rotational tensor of body frame w. r. t the Earth frame
$\boldsymbol{\{}\ \Omega^{BE}\ \boldsymbol{\}}$	angular velocity quaternion of body frame w. r. t. the Earth frame

Chapter 1: Introduction and Technical Background

1.0. Introduction

Horizontal take-off and horizontal landing hypersonic vehicles are a subject of great interest for future space launch missions. The ramjet/scramjet engine has the potential to enable a new class of spacecraft, missiles, and launch vehicles. This dissertation covers the six degrees-of-freedom (6-DoF) modeling and simulation of a generic hypersonic vehicle (GHV) including a ramjet/scramjet propulsion system and an aerodynamic database.

1.1. Early Research on Ramjet Powered Vehicles and their Engines

The story of the ramjet begins with theoretical studies by *Rene Lorin* in France in the years prior to World War I. Fellow Frenchman Rene Leduc actively pursued ramjet development during the 1930s and designed a pioneering ramjet-powered aircraft, the Leduc 0.10, the intervention of World War II prevented it from flying until 1949. Meanwhile, a group of former Soviet Union engineers and scientists pushed ramjet research further than advocates in other nations in the years prior to World War II. In the early 1930s, *Yuri A. Pobedonostsev* and his team bench-tested a small ramjet engine for a couple of minutes. *Pobedonostsev* realized that the ramjet advantages are only relevant at supersonic speeds. He decided to build test ramjets from hollowed-out 76 mm shells, firing them from artillery field pieces. This advanced idea was originally developed by British researchers in 1926. The *Pobedonostsev* team modified the shells by removing the nose caps in favor of aerodynamic inlets. They also used solid fuel (white phosphorus) instead of a bursting charge. To prevent the powder charge of the

cannon from destroying the ramjet as it was fired, Pobedonostsev replaced the baseplate of the shell with a nozzle throat, and a sabot was inserted into the nozzle to support the structure. From 1933 to 1935 the *Pobedonostsev* team tested a series of cannon-launched ramjets, achieving speeds up to Mach 2. The muzzle velocity of the projectile was approximately Mach 1.72, so this early ramjet boosted the projectile's speed by approximately Mach 0.28 or 16%. Although Pobedonostsev was challenged by numerous problems, his tests encouraged Soviet ramjet enthusiasts to build small two-stage rocket-boosted ramjets using solid fuel. A research team led by *Igor A. Merkulov* launched several of these two-stage ramjets in 1939. After successful testing of the two-stage rocket-boosted ramjet up to 6,000 ft above sea level, *Merkulov* and *Aleksei Shcherbakov* decided to test ramjets on aircraft to evaluate their potential as combat boosters; for example, to enable obsolete fighters to engage higher-performance opponents.

Figure 1: Polikarpow I-153

For the first time, in 1940, test pilot *Petr Loginov* flew a modified *Polikarpov* 1-152 biplane fighter powered by two auxiliary liquid-fuel ramjets: this was the first flight by a ramjet-powered aircraft in aviation history. Later on, the Soviets conducted further tests on modified 1-153 and Yak-7 fighters. The rapid development of Soviet gas turbines applying German and British technologies for such auxiliary propulsion in the late 1940s. *W. Trommsdorff* directed German research on ramjet engines before and during World War II. In Nazi Germany another version of the ramjet artillery shell concept was tested and eventually modified Dornier Do 17Z and Do 217E-2 bombers carried out experimental flight of ramjets.

Figure 2: Do-217E

By the end of the war, German designers *Alexander Lippisch* and *Eugen Sanger* were able to demonstrate that artillery shells were fired at Mach 2.9 muzzle velocities, accelerating using ramjet propulsion to speeds of Mach 4.2. The Nazi achievement with ramjet artillery contrasts sharply with the Soviet failure. Their success was in part due to the greater care taken by the Germans to understand inlet and combustion processes and the behavior of a variety of solid and liquid fuels.

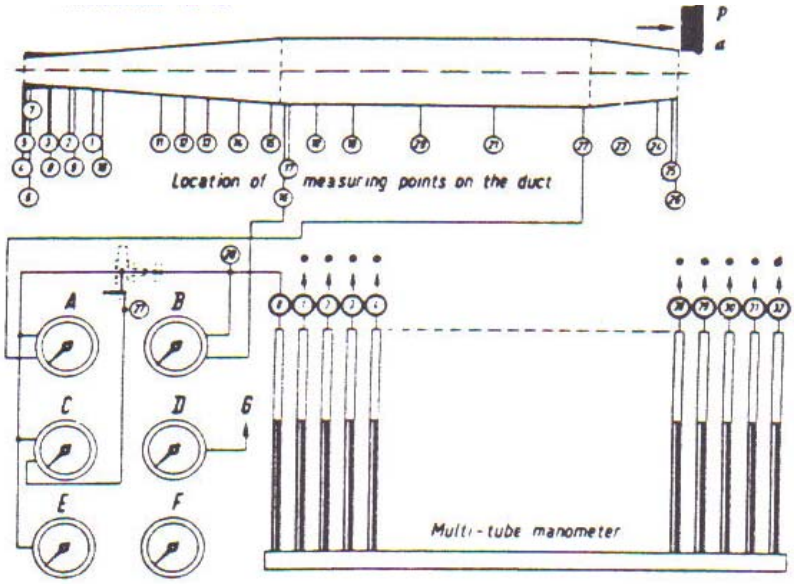

Figure 3: German Ramjet Rig, 1942-43

In the United States, engineer *Roy Marquardt* pioneered ramjet development during World War II, working under a Navy grant with the University of Southern California. The Army Air Force tested some of his engines on modified aircraft in 1945. Two M.I.T. designed 20 in. diameter ramjets mounted on the wingtips of a modified North American P-51D Mustang boosted the fighter's speed by 40 mph during trials in 1945 at Wright Field.

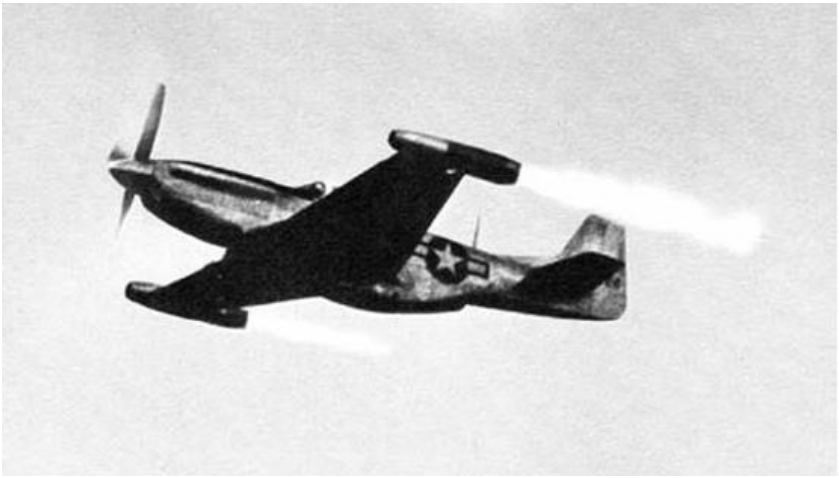

Figure 4: North American P-51D Mustang

Early in 1952, Hiller proposed that the Navy authorize the construction of an evaluation quantity of ramjet powered helicopters. The Hiller HOE (Hornet) was a helicopter powered by ramjets located on the tips of the rotor, and it was produced around 1954. The design was a failure; the vehicle had very poor fuel economy, a low top speed, poor range, and was very noisy. It did have a relatively high lifting capacity. The Army and Navy flew a small number of these aircraft for a short time to test and evaluate the technology.

Figure 5: Hiller HOE

In 1959, a French experimental aircraft called the canard delta Nord 1500 Griffon reached Mach 2.19 (1448 mph) under the combined power of a turbojet and ramjet, with the ramjet contributing approximately 80% of the total thrust of the propulsion system.

Figure 6: Nord 1500 Griffon

The United States Air Force supported Nord research via trans-Atlantic research contracts. These projects were the exceptions; the success of the turbojet overshadowed that of the temperamental and fuel-hungry ramjet. There were some areas where the ramjet excelled, involving primarily the field of missile development. In 1949 and 1950, the NACA tested the more advanced ethylene-fueled F23 ramjet , which reached Mach 3.12 at an altitude of 67,200 feet. NACA also started air-launched ramjet trials, launching them from modified North American F-82 Twin Mustang and McDonnell F2H-2 Banshee fighters. One such test vehicle had a Thiokol T55 solid-fuel rocket booster contained within the ramjet that expelled through the nozzle as the ramjet fired up.

Figure 7: McDonnell F2H-2 Banshee Fighter

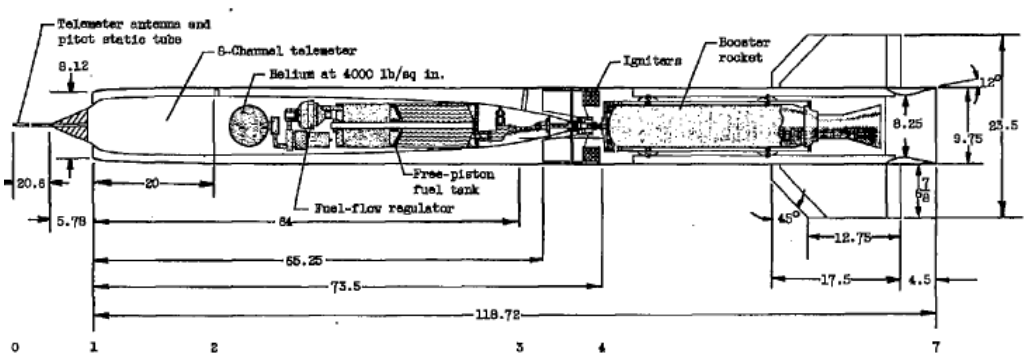

Figure 8: Pentaborane-Fueled Ramjet

This ramjet, designed by the Lewis laboratory, burned pentaborane fuel. In 1956, it demonstrated satisfactory operation using pentaborane up to Mach 3.02 following air-launch from an F2H-2 at 42,000 feet.

1. 2. Ramjet-Scramjet Engines

The National AeroSpace Plane (NASP) program originated in the early 1980s with the intention of designing a jet aircraft that could fly fast enough to attain orbital velocity. A large part of the research and development (R&D) community, NASA, the Air Force, and the Navy supported the program as it promised to produce a research aircraft and advance the hypersonic technology base that would address questions about hypersonic flight. The program advanced hypersonic technology across several disciplines, including the creation and application of Computational Fluid Dynamics codes for predicting airflows and combustion results; production of advanced materials; practical and theoretical work in scramjet engine flowpath performance and the use and storage of hydrogen-based fuels.

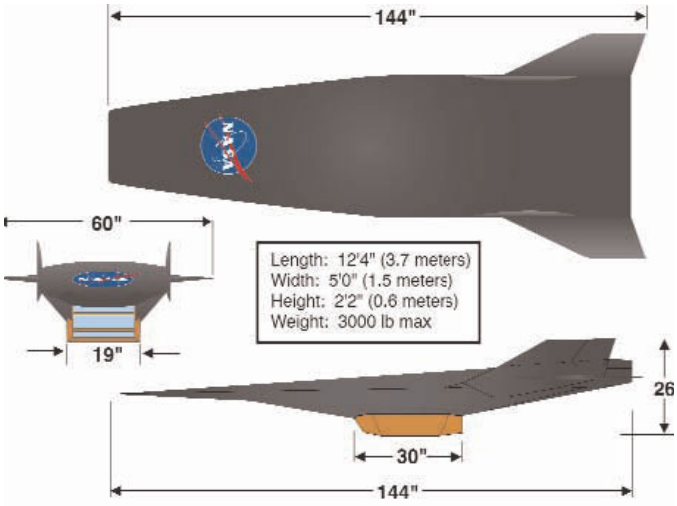

Figure 9: X-43-A

**** References [1], [2], and [3] are the main references for this Chapter.***

NASA made aviation history with the first successful flight of a scramjet-powered airplane, the X-43A, at hypersonic speeds, speeds greater than Mach 5 or five times the speed of sound. At Mach 7 the X-43A research vehicle was traveling at nearly 5,000 mph during the March 2004 flight. Later, in 2005, the world recognized NASA's X-43A scramjet with a new world speed record for a jet-powered aircraft, Mach 9.6, or nearly 7,000 mph.

1. 3. Hypersonic Models

Although NASA and the U.S. Air Force have a long history of hypersonic research there are not many hypersonic vehicle models in the open literature. The first dynamic analytical aeropropulsive/aeroelastic hypersonic vehicle model in the open literature was developed and published by Dr. Frank Chavez and Dr. David Schmidt [4]. In this model, a two-dimensional hypersonic aerodynamic analysis utilizing Newtonian theory, coupled with a one-dimensional aerodynamics/thermodynamics analysis of the flow within a SCRAM jet type propulsion system was used. In 2005,

another nonlinear model for the longitudinal dynamics (3-DoF) of a hypersonic air-breathing vehicle was developed by Air Force Research Laboratory researchers. This model was derived from first principles, and captures a number of complex interactions between the propulsion system, aerodynamics, and structural dynamics [5]. Two additional effects were considered in this dynamic model that were not considered in the references mentioned previously. The first effect considered was the on-design and off-design propulsion system performance resulting from an oscillating bow shock and the second effect they considered the presence of coupling between the rigid-body accelerations and flexible body dynamics. Both models were developed using pure analytical methods and did not included the wind tunnel experimental investigations or the results from CFD code analysis. This research covers the development and mathematical implementation of a 6-DoF model and simulation of a Generic Hypersonic vehicle using analytical methods, experimental wind tunnel investigations, and CFD modeling.

Chapter 2: Simulation of Hypersonic Aerospace Vehicles

2.1. Mathematical Concepts in Modeling

Tensor Elements

Tensors provide a natural and concise mathematical framework for formulating and solving problems in areas of physics such as flight dynamics, elasticity, fluid mechanics, and general relativity. Applying Newtonian mechanics is an adequate way to describe the dynamic of systems. For simplification, in flight dynamics, the Euclidean metric to finite differences Δ, or the Cartesian metric, is:

$$\Delta S^2 = \Delta x_1^2 + \Delta x_2^2 + \Delta x_3^2$$

The elements of Δx_i are reciprocally orthogonal. Using the Pythagorean Theorem ΔS can be calculated.

Coordinate System

Coordinates are ordered algebraic numbers called triples or n-tuples. Coordinate systems are abstract entries that establish the one-to-one correspondence between the elements of the Euclidean three-space and the coordinate [6]. Generally, a coordinate system is a system for assigning a tuple of numbers to each point in an n-dimensional space. Coordinate transformation means relabeling each element in the Euclidean space with new coordinates according to a certain mathematical algorithm.

Cartesian Tensors

A first-order tensor (vector) X is a combination of ordered triples, any two of which satisfy the transformation law as follows:

$$[X]^B = [T]^{BA}[X]^A \tag{2-1}$$

$]^A$ and $]^B$ are any allowable coordinate system.

A second-order tensor is a combination of ordered 9-tuples, any two of which satisfy the transformation law as follows:

$$[X]^B = [T]^{BA}[X]^A\overline{[T]}^{BA} \tag{2-2}$$

where $]^A$ and $]^B$ are any allowable coordinate system.

This approach is useful in two ways:

From a mathematical point of view - because tensors are the total of all ordered n-tuples and are defined in all coordinate systems. Consequently, they are not tied to any particular system.

1. From a physical point of view, tensors describe properties of relating to the essential nature of geometrical or physical objects, i.e. objects that do not depend on the form of presentation (coordinate system).

There are four important rules followed by Cartesian tensors:

Rule 1: Subscript reversal of displacement vectors (tensors) changes their sign.

$$S_{AB} = -S_{BA}$$

Rule 2: Vectors addition of displacement vectors must be consistent with subscript contraction.

$$BC \longleftarrow \underbrace{B\ A + A\ C}_{\text{Contraction}} \tag{2-3}$$

Rule 3: Coordinate systems have no origins.

Rule 4: The displacement vectors can be transformed from one coordinate system to another coordinate system like a first-order tensor [6].

$$[S_{AB}]^B = [T]^{BA}[S_{BA}]^A \qquad (2\text{-}4)$$

Coordinates and Frames

Coordinates systems are abstract entities that establish the one to one correspondence between the elements of the Euclidean three space and the coordinates.

2.2. Frames

A frame is a bounded continuous set of points over the Euclidean three-space with invariant distances and which processes, as a subset, at least three nonlinear points.

Reference Frames

A frame of reference is a particular perspective from which motions are observed. Without reference points and frames, the positions and motions of air vehicles are ambiguous.

Geocentric-Inertial Frame

The most useful inertial frame is collocated with the center of the Earth; the location of the frame is given by the displacement vector SIH of the center of the Earth I with respect to the center of the sun H. Its orientation is described by the base vector $\hat{i}_1$, $\hat{i}_2$ & $\hat{i}_3$. The positive X axis points toward the mean vernal equinox, the positive Z points along the mean rotation axis of the Earth, and the Y positive direction can be found by applying the right-hand rule.

Earth Frame

The base point is at the Earth's center, and the triad consists of the base vectors $\hat{e}_1$, $\hat{e}_2$ and $\hat{e}_3$. One meridian of the Earth assumes a particular significance. It is the prime meridian that traces through the Royal Observatory at Greenwich, located

in a suburb of London. Its intersection with the equator establishes the penetration point of the first vector $\hat{e}_1$. The base vector $\hat{e}_3$, and $\hat{e}_2$ completes the right-hand rule.

Body Frame

Although this system is usually not used as a reference, it is nevertheless important for modeling the location and orientation of vehicles under study. Its base point B is coincident with the center of mass (C.M.) as a function of time. The b_1 base vector is out of the nose, b_2 is out of the right wing, and b_3 is the principal axis defined by right hand rule to be positive in the down direction.

2.3. Coordinate Transformation Matrix

General Transformation Matrix

A first-order tensor $[x]$, and any two allowable coordinate systems $]^A$ and $]^B$ with the transformation $[T]^{BA}$ is introduced using the definition of the first-order tensor equation (2-1):

$$[x]^B = [T]^{BA}[x]^A$$

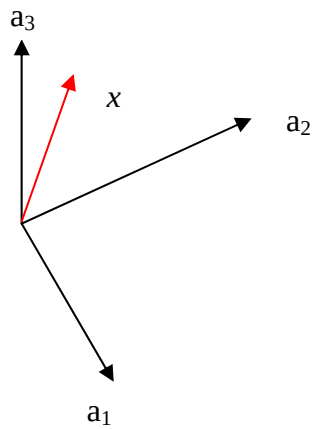

Figure 10: The *x* Vector (triad) in the $]^A$ Coordinate System

The decomposition of x in the $]^A$ coordinate system is as follows [6]:

$$x = x_1^A a_1 + x_2^A a_2 + x_3^A a_3 \qquad \text{(2-5a)}$$

Now if x is expressed in]^B coordinates:

$$x = x_1^A \left[a_1\right]^B + {}_2^A \left[a_2\right]^B + x_3^A \left[a_3\right]^B \qquad \text{(2-5b)}$$

The equation can be written in linear algebra matrix form as follows:

$$\left[x\right]^B = \left[\ \left[a_1\right]^B \ \left[a_2\right]^B \ \left[a_3\right]^B\right] \times \begin{bmatrix} x_1^A \\ x_2^A \\ x_3^A \end{bmatrix} \qquad \text{(2-6)}$$

Comparing equation (2-6) with the first-order tensor transformation, the representation of the transformation matrix becomes:

$$\left[T\right]^{BA} = \left[\left[a_1\right]^B \left[a_2\right]^B \left[a_3\right]^B\right] \qquad \text{(2-7)}$$

The *x* vector in the]^B coordinate system is decomposed as:

$$x = x_1^B b_1 + x_2^B b_2 + x_3^B b_3 \qquad \text{(2-8)}$$

The coordinate *x* in the] ^{A} system is:

$$\left[x\right]^A = x_1^B \left[b_1\right]^A + x_2^B \left[b_2\right]^A + x_3^B \left[b_3\right]^A = \left[\left[b_1\right]^A \left[b_2\right]^A \left[b_3\right]^A\right] \left[x\right]^B \qquad \text{(2-9)}$$

Solving for $\left[x\right]^B$ and comparing it with the first-order tensor transformation yields another representation of $\left[T\right]^{BA}$ which is:

$$\left[T\right]^{BA} = \begin{bmatrix} \left[\overline{b_1}\right]^A \\ \left[\overline{b_2}\right]^A \\ \left[\overline{b_3}\right]^A \end{bmatrix} \qquad \text{(2-10)}$$

The representation of $[T]^{BA}$ may be summarized as:

$$[T]^{BA} = \begin{bmatrix} t_{11} & t_{12} & t_{13} \\ t_{21} & t_{22} & t_{23} \\ t_{31} & t_{32} & t_{33} \end{bmatrix} \tag{2-11}$$

Direction Cosine Transformation Matrix

The interpretation of each $[a_i]^B$ i=1, 2, and 3 in equation (2-5) is:

$$[\mathrm{a_i}]^{\mathrm{B}} = \begin{bmatrix} \mathrm{a_{1i}}^{\mathrm{B}} \\ \mathrm{a_{2i}}^{\mathrm{B}} \\ \mathrm{a_{i2}}^{\mathrm{B}} \end{bmatrix} \qquad \mathrm{i} = 1,\ 2,\ 3 \tag{2-12}$$

With this definition of $[a_i]^B$, the transformation matrix $[T]^{BA}$ becomes a 3x3 matrix as:

$$[T]^{BA} = \begin{bmatrix} {a_{11}}^B & {a_{12}}^B & {a_{13}}^B \\ {a_{21}}^B & {a_{22}}^B & {a_{23}}^B \\ {a_{31}}^B & {a_{32}}^B & {a_{33}}^B \end{bmatrix} \tag{2-13}$$

To calculate each element as the cosine of the angle between two base vectors b_i and a_i the scalar product (dot product) is applied and expressed in the $]^B$ coordinate system as:

$$\cos\angle(a_k, b_1) = \left[\overline{a_k}\right]^B [b_1]^B = \begin{bmatrix} a_{1k}^B & a_{2k}^B & a_{3k}^B \end{bmatrix} \begin{bmatrix} 1 \\ 0 \\ 0 \end{bmatrix} = a_{1k}^B \qquad k = 1,\ 2,\ 3 \tag{2-14}$$

The general form is:

$$\cos\angle(a_k, b_i) = a_{ik}^B = t_{ik} \ ; \quad i = 1,\ 2,\ 3 \quad k = 1,\ 2,\ 3 \tag{2-15}$$

Kinematics of Changing Times

The time derivatives of the vector "s" transformed from the A to the B coordinate system is [6]:

$$\left.\frac{ds}{dt}\right]_A = \left.\frac{ds}{dt}\right]_B + \omega \times s \tag{2-16}$$

where ω is the angular velocity between the B and the A coordinate systems.

Applying equation (2-1) through (2-16) follows:

$$[s]^A = [T]^{AB} \times [s]^B \tag{2-17}$$

Taking the time derivative from (2-17) gives:

$$\left[\frac{ds}{dt}\right]^A = \left[\frac{dT}{dt}\right]^{AB} \times [s]^B + \left[\frac{ds}{dt}\right]^B \times [T]^{AB} \tag{2-18-a}$$

then factoring out $[T]^{AB}$ yields:

$$\left[\frac{ds}{dt}\right]^A = [T]^{AB}\left(\left[\overline{T}\right]^{AB} \times \left[\frac{dT}{dt}\right]^{AB} \times [s]^B + \left[\frac{ds}{dt}\right]^B\right) \tag{2-18-b}$$

where $\left[\overline{T}\right]^{AB} = \left[T^{-1}\right]^{AB}$

Also, $\left[\overline{T}\right]^{AB} \times \left[\frac{dT}{dt}\right]^{AB} = [T]^{BA} \times \left[\left(\frac{dT}{dt}\right)^{-1}\right]^{BA}$ so,

$$\left[\frac{ds}{dt}\right]^A = [T]^{AB}\left([T]^{BA} \times \left[\left(\frac{dT}{dt}\right)^{-1}\right]^{BA} \times [s]^B + \left[\frac{ds}{dt}\right]^B\right) \tag{2-19}$$

The angular velocity vector ω corresponds to:

$$\omega = [\mathrm{T}]^{\mathrm{BA}} \times \left[\left(\frac{\mathrm{dT}}{\mathrm{dt}} \right)^{-1} \right]^{\mathrm{BA}} \tag{2-20}$$

2.4. Coordinate Systems and their Transformations

Earth Coordinate System

The transformation matrix [T] ^{EI} from the Earth coordinate frame to the inertial coordinate is obtained by inspection:

$$[T]^{EI} = \begin{bmatrix} \cos\theta & \sin\theta & 0 \\ -\sin\theta & \cos\theta & 0 \\ 0 & 0 & 1 \end{bmatrix} \tag{2-21}$$

The angle between 1^{E} and 1 is called the hour angle θ, and establishes the Greenwich meridian relative to the vernal equinox.

Geographic Coordinate System

At a specific point on the surface of the Earth, with its longitude ι and latitude λ, the geographic coordinate system $]^{G}$ is defined as:

$$[\mathrm{T}]^{\mathrm{GE}} = \begin{bmatrix} -\sin(\lambda)\cos(\iota) & -\sin(\lambda)\sin(\iota) & \cos(\lambda) \\ -\sin(\iota) & \cos(\iota) & 0 \\ -\cos(\lambda)\cos(\iota) & -\cos(\lambda)\sin(\iota) & -\sin(\lambda) \end{bmatrix} \tag{2-22}$$

Body Coordinate System

The body coordinate system is a preferred coordinate system since it is aligned with the body. The transformation from the body coordinate frame to the geometric coordinate can be achieved by completing three transformations using the Euler angles: Yaw, Pitch, and Roll, or ψ, θ, and φ .

$$[T]^{BG} = [T(\phi)]^{BY} \; [T(\theta)]^{YX} \; [T(\psi)]^{XG} \tag{2-23}$$

These three transformations lead us to the body axes through Euler's angles.

$$[\mathrm{T}]^{\mathrm{BG}} = \begin{bmatrix} \cos\psi\cos\theta & \sin\psi\cos\theta & -\sin\theta \\ \cos\psi\sin\theta\sin\phi - \sin\psi\cos\phi & \sin\psi\sin\theta\sin\phi + \cos\psi\cos\phi & \cos\theta\sin\phi \\ \cos\psi\sin\theta\cos\phi + \sin\psi\sin\phi & \sin\psi\sin\theta\cos\phi - \cos\psi\sin\phi & \cos\theta\cos\phi \end{bmatrix} (2-24)$$

2.5. The Six Degrees of Freedom (DoF) Equations of Motion

In this research the flat Earth approximation is used. In many studies, the elliptical Earth assumption is used to simulate the equations of motion for missiles and hypersonic vehicles.

Vector Small Rotation

Consider the vector ***b*** rotation from its initial position $b(t_0)$ to its current position through the rotation tensor R given by:

$$b(t) = R \times b(t_0)$$

Applying vector algebra, the difference between the initial position $b(t_0)$ and the current position of the vector b(t) is shown in Figure 11.

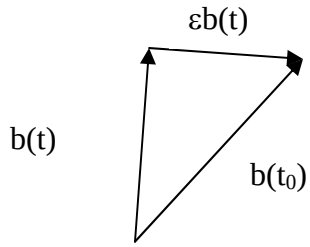

Figure 11: Vector Analysis

$$\varepsilon b(t) = b(t_0) - b(t) \qquad (2\text{-}25)$$

Also, from the rotation tensor definition:

$$b(t) = Rb(t_0) \qquad (2\text{-}26\text{-a})$$

Substitution of equation 2-23 into equation 2-24 yields:

$$\varepsilon b = b(t_0)\left(R - E\right) \qquad (2\text{-}26\text{-b})$$

where E is the identity matrix.

Now the perturbation tensor of rotation can be defined as:

$$\varepsilon R = \left(R - E\right) \qquad (2\text{-}27)$$

$$\varepsilon b = \varepsilon R b\left(t_0\right) \qquad (2\text{-}28)$$

The replacement of the vector b in time t, **εb**, is the result of the multiplication of a tensor **εR** with the initial vector.

The time derivative of the perturbation tensor of rotation **εR** is related to the angular velocity tensor:

$$\frac{d\left(\varepsilon R\right)}{dt} = \Omega^{BA} = D\left(R^{BA} \times \bar{R}^{BA}\right) \qquad (2\text{-}29)$$

Since the tensor **εR** is skew symmetric then so is $\mathbf{\Omega^{BA}}$.

$$\left[\omega^{BA}\right] = \begin{bmatrix} p \\ q \\ r \end{bmatrix} \Leftrightarrow skew\ symmetric\ matrix\ \Omega^{BA} = \begin{bmatrix} 0 & -r & q \\ r & 0 & -p \\ q & p & 0 \end{bmatrix} \qquad (2\text{-}30)$$

The Flat-Earth Equations of Motion

The transitional equations for a flight vehicle are subject to the aerodynamics and proportional force $F_{a,p}$ and the gravitational force *mg.* These are simulated next.

Newton's 2nd law with respect to the inertial frame "*I*" states that the time rate of change of linear momentum equals the externally applied forces. These consist of the aerodynamics and proportional force $F_{a,p}$ and the gravitational force *mg.* This is shown as:

$$mD^{I}\, v_{B}^{I} = f_{a,p} + mg \qquad (2\text{-}31)$$

v_{B}^{I} is the velocity of the center of mass with respect to the inertial reference frame I. The flat Earth assumption lets us take the Earth frame 'E' as an inertial frame. Equation 2-29 becomes:

$$mD^{E}\, v_{B}^{E} = f_{a,p} + mg$$

$$mD^{E}\, v_{B}^{E} = m\left[D^{B}\, v_{B}^{E} + \Omega^{BE} v_{B}^{E} \right] \qquad (2\text{-}32)$$

$$m\left[D^{B}\, v_{B}^{E} + \Omega^{BE} v_{B}^{E} \right] = f_{a,p} + mg$$

Ω^{BE} is the angular velocity between the coordinate system $]^{A}$, $]^{B}$. To generate the ordinary time derivative, all terms should be expressed in the coordinate system $]^{B}$.

$$m\left[\frac{d\, v_{B}^{V}}{dt} \right] + m\left[\Omega^{BE}\right]^{B} \left[v_{B}^{E}\right]^{B} = \left[f_{a,p}\right]^{B} + m\left[g\right]^{B} \qquad (2\text{-}33)$$

The gravitational acceleration $[g]^{B}$ is modeled in a level coordinate system as: $\left[\overline{g}\right]^{L} = [0 \quad 0 \quad g]$.

To transform the]^{B} coordinate system into the]^{L} coordinate system, just apply equation (2-1). The transitional equations in matrix form become:

$$m\left[\frac{d\,v_B^V}{dt}\right]+m\left[\Omega^{BE}\right]^B\left[v_B^E\right]^B=\left[f_{a,p}\right]^B+m\left[T\right]^{BL}\left[g\right]^L \qquad (2\text{-}34)$$

Written in the coordinate form:

$$m\left\{\begin{bmatrix} du/dt \\ dv/dt \\ dw/dt \end{bmatrix}^B+\begin{bmatrix} 0 & -r & q \\ r & 0 & -p \\ -q & p & 0 \end{bmatrix}^B\begin{bmatrix} u \\ v \\ w \end{bmatrix}^B\right\}=\begin{bmatrix} f_{a,p1} \\ f_{a,p2} \\ f_{a,p3} \end{bmatrix}^B+\left[T\right]^{BL}\begin{bmatrix} 0 \\ 0 \\ mg \end{bmatrix}^L \qquad (2\text{-}35)$$

If the matrix multiplications are further developed the transitional differential equations become:

$$\begin{aligned}\frac{du}{dt}&=rv-qw+\frac{f_{a,p1}}{m}+t_{13}\,g\\ \frac{dv}{dt}&=pw-ru+\frac{f_{a,p2}}{m}+t_{23}\,g\\ \frac{dw}{dt}&=qu-pv+\frac{f_{a,p3}}{m}+t_{33}g\end{aligned} \qquad (2\text{-}36)$$

Euler's law states that the time rate of change of angular momentum equals the externally applied moments, and it governs the rotational degrees of freedom. E is picked as an inertial frame.

$$D^E\,I_B^B\,\omega^{BE}=M_B \qquad (2\text{-}37)$$

To transfer the rotational derivative into the body frame:

$$D^B\,I_B^B\,\omega^{BE}+\Omega^{BE}\,I_B^B\,\omega^{BE}=M_B \qquad (2\text{-}38)$$

Expanding the angular momentum vector:

$$D^B(I_B^B\,\omega^{BE})\;=I_B^B\,D^B\omega^{BE}+\omega^{BE}\,D^B I_b^b$$

The term $D^B I_B^B$ is zero because we assumed the airplane as a rigid body.

$$D^B (I_B^B \omega^{BE}) = I_B^B D^B \omega^{BE} \tag{2-39}$$

Then equation (2-38) changes to

$$I_B^B D^B \omega^{BE} + \Omega^{BE} I_B^B \omega^{BE} = M_B \tag{2-40}$$

As a coordinate system, body coordinate is chosen because it expresses the moment of inertia tensor in a constant form [6].

$$\left[I_B^B\right]^B \left[\frac{dw^{BE}}{dt}\right]^B + \left[\Omega^{be}\right]^B \left[I_B^B\right]^B \left[\omega^{BE}\right]^B = \left[M_B\right]^B$$

$$\left[\frac{dw^{BE}}{dt}\right]^B = \left(\left[I_B^B\right]^B\right)^{-1} \left(-\left[\Omega^{be}\right]^B \left[I_B^B\right]^B \left[\omega^{BE}\right]^B + \left[M_B\right]^B\right) \tag{2-41}$$

Figure 12 shows the modeling and simulation flow chart. Now the developed equations of motion can be used for modeling and simulation purposes. As shown in equations (2-34) and (2-41), the simulation of the GHV cannot be done successfully unless the aerodynamic and the propulsion analytical models are developed prior to the simulation process.

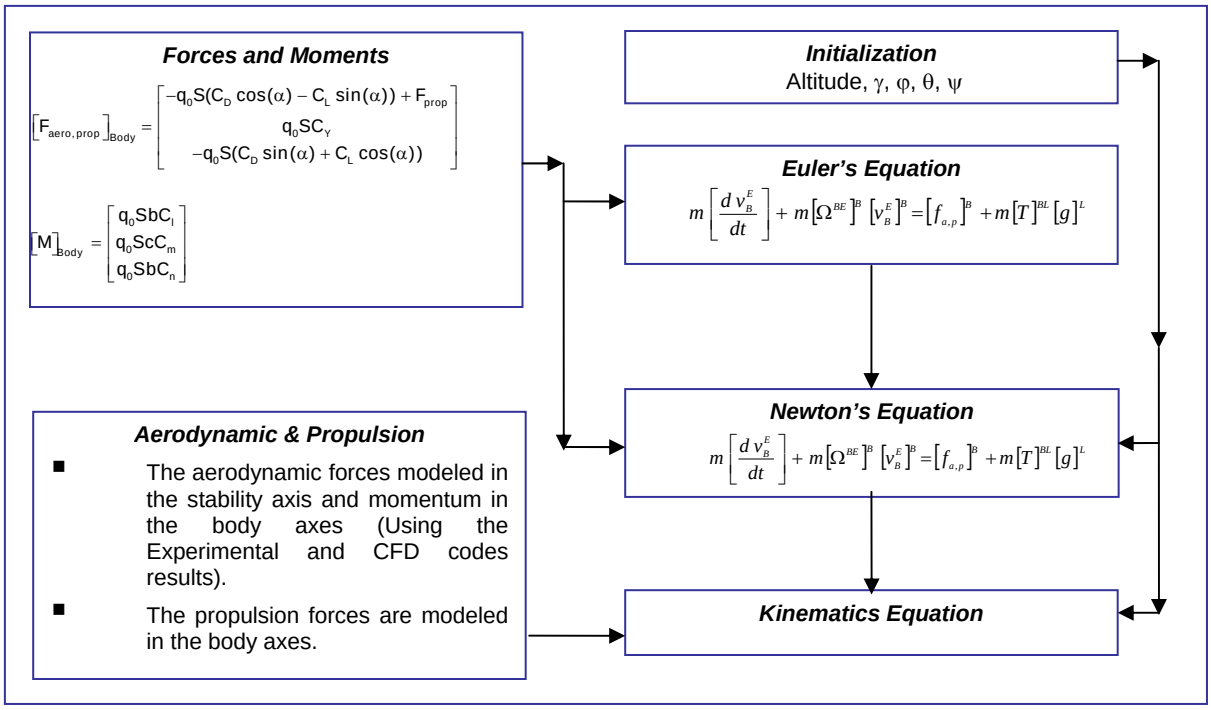

Figure 12: Simulation and Modeling Procedure

The following chapters discuss the aerodynamic and propulsion models of the GHV.

Chapter 3: Aerodynamics

3.0. Introduction

As discussed in chapter two, the aerodynamic forces and moments are required for the six degrees of freedom simulation and modeling effort (see equations (2-34), (2-41)). An overview of the aerodynamic characteristics, along with the process for developing the aerodynamic model using the wind tunnel and the CFD-based results for the Generic Hypersonic Vehicle (GHV), known as the "Winged-Cone," is presented in this chapter [7]. The experimental investigations of the aerodynamic characteristics for the body of the GHV are used as the core of the simulation model. The gaps in the wind tunnel data are filled using the best available CFD results. The aerodynamic characteristics of the vehicle are developed using CFD studies conducted at NASA Langley, Rockwell International [8], and California State University, Los Angeles [9]. These are blended with the wind tunnel results for a similar configuration tested at NASA Langley [8]. For guidance, control, and navigation purposes, analytical expressions for the aerodynamic forces and moments acting on the GHV are developed. The aerodynamic database covers the range of flight Mach numbers, angles of attack, sideslip angles, and control surface deflections. The aerodynamic model is then used for the simulation of the GHV.

3.1. Vehicle Description

The GHV mass model is based on the assumption of a rigid vehicle structure. However, the equations of motion used in the simulation account for the time varying center of mass, the center of gravity, and the moments of inertia. The total mass of

the vehicle, its c.g. location, and the products of inertia vary as fuel is consumed. It is assumed that the c.g. moves only along the body x-axis as the fuel is consumed. Fuel slosh is not considered, and the products of inertia are assumed to be negligible. A sizing analysis of the generic hypersonic vehicle yielded a full-scale gross weight of 300,000 lbs and an overall fuselage length of 200 ft. The top view and side view drawing of the vehicle is given in Figure 13. The geometric characteristics of the vehicle are given in Table 1. Deflections of the elevons are measured with respect to the hinge line (perpendicular to the fuselage centerline). A fuselage-centerline-mounted vertical tail has a full span rudder with its hinge line at 25 percent chord from the trailing edge. Deflections of the rudder are measured with respect to its hinge line. Positive deflections are with the trailing edge left. The small canards (65 A series airfoil) are deployed at subsonic speeds for improved longitudinal stability and control.

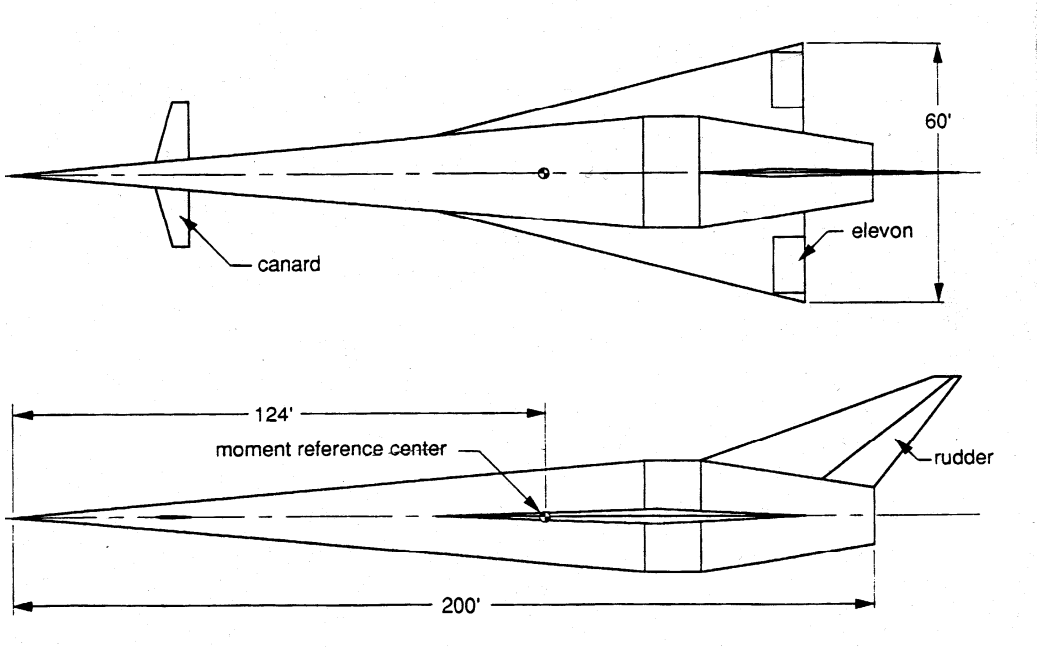

Figure 13: Three View of Generic Hypersonic Vehicle

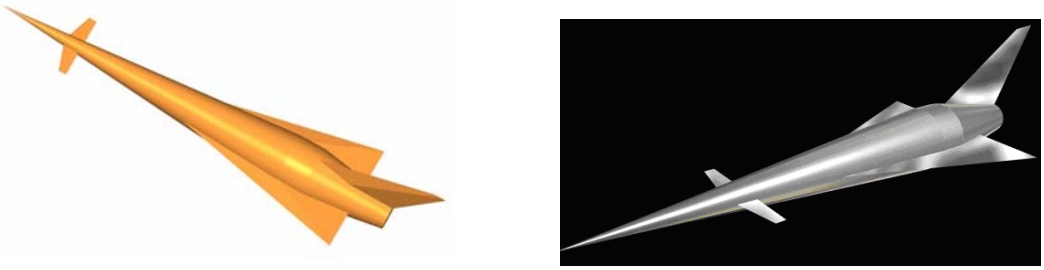

Figure 14: 3-D CAD Model of the GHV

Table 1: Geometric Characteristics of the Generic Hypersonic Vehicle

Wing		
Reference area	ft^2	3603.00
Aspect ratio		1.00
Span	ft	60.00
Leading edge sweep angle	deg.	75.97
Trailing edge sweep angle	deg.	0.00
Mean aerodynamic chord	ft	80.00
Airfoil section	-	diamond
Airfoil thickness to chord ratio	%	4.00
Induced angle	deg.	0.00
Dihedral	deg.	0.00
Wing flap (elevon)		
Area each	ft^2	92.30
Chord (constant)	ft	7.22
Inboard section span location	ft	15
Outboard section span location	ft	27.78
Vertical tail, body centerline		
Exposed area	ft^2	645.70
Theoretical area	ft^2	1248.80
Span		32.48
Leading edge sweep angle	deg.	70.00
Trailing edge sweep angle	deg.	38.13
Airfoil section	-	diamond
Airfoil thickness to chord ratio	%	4.00

Rudder		
Area	ft^2	161.40
Span	ft	22.80
Chord of vertical tail chord ratio, percent	%	25.00
Canard		
Exposed area	ft^2	154.30
Theoretical area	ft^2	5.48
Span	ft	33.60
Leading edge sweep angle	deg.	16.00
Trailing edge sweep angle	deg.	0.00
Airfoil section	-	NACA 65 A 006
Induced angle	deg.	0.00
Dihedral	deg.	0.00
Axisymmetric fuselage		
Theoretical length	ft	200.00
Cone half angle	deg.	5.00
Cylinder radius (maximum)	ft	12.87
Cylinder length	ft	12.88
Boattail half angle	deg.	9.00
Boattail length	ft	40.00
Momentum reference center	ft	124.01

3.2. APAS

For the simulation of the aerodynamic forces and moments, the output data from a subsonic/supersonic/hypersonic analysis code, Aerodynamic Preliminary Analysis System (APAS) [7], is used. The APAS solution is based on the Potential Theory at subsonic/supersonic speeds and the Newton's Impact Theory finite element analysis at hypersonic conditions. The APAS is often used in conceptual design studies due to its short process times and relatively good results. The APAS is actually a front end to two separate analysis codes, the Unified Distributed Panel (UDP) and the Hypersonic Arbitrary Body Program (HABP). The APAS uses the UDP to analyze subsonic and

supersonic runs, and the HABP to analyze hypersonic runs [7]. The APAS estimates the basic vehicle forces (the lift and drag and the side force sideslip) increment coefficient derivatives as functions of angle of attack and Mach number. The program estimates the aerodynamic force increment coefficients for the right and left elevons, and the rudder as functions of angle of attack, surface deflection, and Mach number. Changes in lift, drag, and side force due to body angular rates and aerodynamic coupling between control surface deflections and sideslip are negligible. The APAS estimates the basic vehicle roll and yaw moment sideslip derivatives, the pitch moment increment coefficient, and the roll, pitch and yaw dynamic derivatives as functions of angle of attack and Mach number. The roll and yaw moment increment coefficients for right and left elevon and rudder and the pitch increment coefficients for right and left elevon, and rudder are estimated as functions of angle of attack, surface deflections, and Mach number. These quantities are given relative to the moment reference center. The total moments relative to the c.g. are obtained by adding those caused by lift, drag, and side force to the above quantities. The APAS employs the Transonic Area Rule to calculate the drag coefficient in the transonic region. The Transonic Area Rule states that the wave drag of an aircraft is essentially the same as the wave drag of an equivalent body of revolution when they have a same cross-sectional area distribution as the aircraft [13]. This method works reasonably well in the transonic flight regime when Slender Body Theory is applied to the equivalent body of revolution. The APAS analysis can be done relatively quickly allowing multiple design iterations, and the results usually accurate within twenty percent of actual values. The APAS is good enough for conceptual designs, and the

speed with which they can be achieved allows designers to include aerodynamic calculations in multi-disciplinary design optimization loops. Using the APAS software, aerodynamic data is computed at Mach numbers 0.3, 0.7, 4.0, 6.0, 10.0, 15.0, 20.0, and 24.2 and at angles of attack of -1°, 0°, 2°, 4°, 6°, 8°, 10°, and 12°. At each Mach number and angle of attack combination, coefficients are generated for a range of deflections of the right elevon, the left elevon, and the rudder, each taken separately. Deflections of the rudder of -20 °, -10°, 0°, 10°, and 20° are used for each surface. At two subsonic Mach numbers, 0.3, 0.7, and eight angles of attack, -1°, 0.0°, 2°, 4°, 6°, 8°, 10°, and 12. The increment coefficients caused by control surface deflections are determined as functions of the angle of attack, surface deflections, and the Mach number, and are added to the basic vehicle increments to form total aerodynamic force and moment coefficients. These results are digitized and organized into **more than 80 lookup tables** for the simulation. The lookup tables are available in Appendix A.

3.3. Aerodynamic Model-STructural Analysis RountineS (STARS)

The STARS is a finite element-based program that analyzes a reduced mathematical equivalent of an object. The object is broken down mathematically into several elements of different shapes. The STARS has linear and nonlinear analysis capabilities that include such disciplines as structures, heat transfer, linear aerodynamics, computational fluid dynamics, and controls. Each individual analysis module is general-purpose in nature and is effectively integrated to yield aeroelastic and aeroservoelastic solutions of complex engineering problems [14], [15]. Extensive graphic capabilities exist for convenient model development and post processing of

analysis results. The program is written in modular form in standard FORTRAN (Visual-FORTRAN) language. The core of the nonlinear analysis routine in STARS is a finite element CFD algorithm based on a time-marched solution to the unsteady, compressible Euler equations. The STARS unsteady CFD solutions provide an accurate physical model of the flow field for all flight regimes with the ability to account for nonlinear generation and unsteady movement of shock waves [15].

3.4. Aerodynamic Model-Wind Tunnel

Experimental longitudinal and lateral-directional aerodynamic coefficients are obtained for a GHV configuration. Data is obtained at Mach numbers from 0.6 to 20.0; Reynolds numbers (based on model length) between 2.5×10^{6} and 5.3×10^{6}; and angles of attack from -4 degree to 20 degree. The proposed GHV is expected to take-off from a conventional runway, perform an atmospheric acceleration (using primarily airbreathing propulsion to achieve a low-Earth orbit), re-enter, and land on a runway. As it is expected, extensive use of computational fluid dynamics (CFD) codes are required for the pre-flight analyses of this class of vehicle in different speeds, altitudes, and flight path angles. This increased reliance on CFD codes for future space transportation systems does not reduce the importance of experimental investigations on the GHV. The primary objective of the NASA Langley wind tunnel experiments was to provide timely forces and moments, flow visualization, and the thermal mapping measurements across the Mach number range from M = 0.6 to 20.0 for the GHV configuration [8], [10]. Other objectives were to determine what, if any, modifications in the test technique would be required to perform such a fast-paced

study and to provide early experimental data for comparison with engineering design codes such as HABP.

3.5. Aerodynamic Model- Development of an Aerodynamic Database

An overview of the aerodynamic characteristics, along with the process for developing an aerodynamic database for the (GHV), is presented in this section. The experimental investigations of the aerodynamic characteristics for the body of GHV are presented in section 3.3 and are used as the core of the database. The gaps in the wind tunnel data are filled using the best available CFD results. The following algorithm is used to merge the different sets of aerodynamic data together. The incremental coefficients due to Mach number variation are calculated using either APAS or STARS data.

$$C_i(\alpha,\beta,M_i) = Ci(\alpha,\beta,M_{i-1},WT) + \Delta Ci(APAS)\left(or + \Delta Ci(STARS)\right) \quad (3\text{-}1)$$

$$\Delta Ci(APAS) = \Delta Ci(\alpha,\beta,M_i) - \Delta Ci(\alpha,\beta,M_{i-1}) \quad (3\text{-}2\text{-}a)$$

$$\Delta Ci(STARS) = \Delta Ci(\alpha,\beta,M_i) - \Delta Ci(\alpha,\beta,M_{i-1}) \quad (3\text{-}2\text{-}b)$$

The database is generated and tabulated into lookup tables for different speed regimes. However, in the control system design and trajectory optimization process, lookup tables are not the most suitable. Mathematical methods are applied to each lookup table to find the best analytical expression for each aerodynamic coefficient. Multi-variable curve fitting is a very challenging task. Acquiring an accurate curve to match a set of highly nonlinear data can be a very challenging and also time consuming process. Because of this, interpolation or extrapolation of the lookup table values is more popular method for implementing aerodynamic models.

3.6. Curve Fitting with Multiple Variables

In this research aerodynamic coefficients are a function of several independent variables like the vehicle's angle of attack, Mach number, sideslip angle, and deflection of control surfaces. Numerical optimization techniques are employed to find the best fit to the sets of data. The goal of the Numerical Optimization Curve Fitting (NOCF) program is to solve nonlinear curve-fitting equations using the Least Squares Algorithm. For minimization problems Trust Region Methods are employed. These methods generate a new class of algorithms for minimization problems. Trust Region Methods are powerful, reliable and most important, they have strong convergence properties.

Both the given input (including the independent variables) $\bar{X}$ and the observed output data $\bar{Y}$ are considered as vectors.

The $\upsilon(\bar{X})$ is a predefined function that is fitted to the input data vector $\bar{X}$.

A new function, *F*(x), is defined as follows:

$$F(x) = \frac{1}{2}\left|\upsilon\left(x, \bar{X}\right) - \bar{Y}\right|^2 \tag{3-3}$$

Where "x" is the starting guess for the fitting process and *F*(x) represents the sum of square errors (SSE). The optimization techniques are applied to minimize the *F*(x).

$$\min_x F(x) = \frac{1}{2}\left|\upsilon\left(x, \bar{X}\right) - \bar{Y}\right|^2 \tag{3-4}$$

The algorithm is a Subspace Trust Region Method and is based on the Interior-Reflective Newton method described by Thomas Coleman and Yuying Li [16], [17]. The function *F*(x) takes vector arguments $\bar{X}$, $\bar{Y}$, x and returns scalars. The goal of the minimization process is to move to a point with a lower function value than *F*(x)

from the starting point "x." In this method Function "*F"* is approximated with a simpler function "*G."* This function reflects a fairly similar behavior of function "*F*" in a neighborhood around the starting point "x." This neighborhood is called "*N,"* the trust region. A trial step (increment) "s" is computed by minimizing "*G"* over the trust region.

$$s = x_{i+1} - x_i \tag{3-5}$$

$$\min_x G = \min_x \left\{ \frac{1}{2} s^T \cdot Hf_i \cdot s + s^T \cdot q_i \ \textit{such that} \ \left\| D_i s \right\| \le \Delta_i \right\} \tag{3-6}$$

Where H_f is a symmetric approximation to a Hessian matrix $\nabla^2 F(x)$, $q \equiv \nabla F(x)$, D_i is a scaling matrix, and Δ_i represents the trust region size (a scalar).

$$Hf = \begin{bmatrix} \frac{\partial^2 F}{\partial x^2_1} & \frac{\partial^2 F}{\partial x_1 \partial x_2} & \cdots & \frac{\partial^2 F}{\partial x_1 \partial x_n} \\ \frac{\partial^2 F}{\partial x_2 \partial x_1} & \frac{\partial^2 F}{\partial x^2_2} & \cdots & \frac{\partial^2 F}{\partial x_2 \partial x_n} \\ \vdots & \vdots & \ddots & \vdots \\ \frac{\partial^2 F}{\partial x_n} & \frac{\partial^2 F}{\partial x_n \partial x_2} & \cdots & \frac{\partial^2 F}{\partial x^2_n} \end{bmatrix} \tag{3-7}$$

$$q = grad(F) = \nabla(F) = \left(\frac{\partial F}{\partial x_1}, \frac{\partial F}{\partial x_2}, \ldots, \frac{\partial F}{\partial x_n} \right) \tag{3-8}$$

In equation 3-6, "s" is an approximate solution to a quadratic subproblem (3-6).

Reference [16] provides a numerical scheme for the solution of equation (3-6). The solution of (3-6) can be found by determining $\lambda \geq 0$ such that $Hf+\lambda I$ is positive definite and

$$\left\| \left(hf + \lambda I \right)^{-1} \cdot s \right\| = \Delta \tag{3-9}$$

If $\lambda \geq 0$ does not satisfy (3-9) then Hebden's algorithm must be used [17].

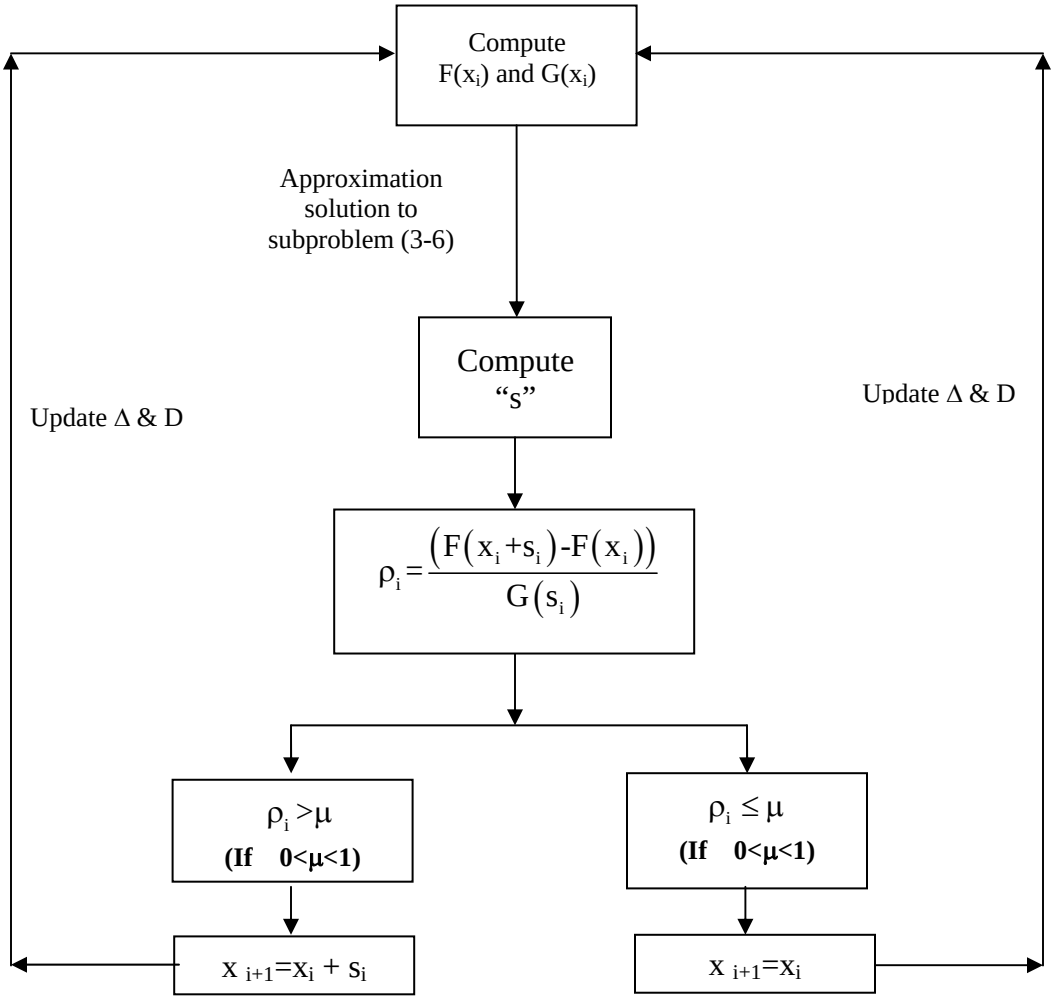

Figure 15: Trust Region Algorithm

Figure 15 shows the minimization algorithm using the Unconstrained Region Method. Also, reference [16] provides a numerical algorithm, GQTPAR, for trust

region problems using Cholesky factorization. After calculating the step (increment) "s" the new problem is to minimize G(s),

$$\min_{x} \{G(s)\ s \in N\} \qquad (3\text{-}10)$$

3.7. Aerodynamic Model- Analytical Procedure

The aerodynamic modeling procedure is completed for all coefficients, and the analytical results are collected in a MATLAB function (aero.m). This function represents a complete aerodynamic model of the GHV for all speed ranges. This approach makes each element of the simulation a separate module. For any other hypersonic vehicle with different configuration, the aerodynamic module can be generated by applying the same MATLAB code (FITTERNEW.m) to the aerodynamic lookup tables. This makes the modeling and simulation routine robust and flexible for use analyzing different configurations with different aerodynamic characteristics. It is very important to keep the format of the lookup tables compatible with the MATLAB function (FITTERNEW.m).

Table 2 and equation (3-11) show lookup table and nonlinear analytical expression developed for the lift coefficient.

Table 2: Lift Coefficient - Category: Subsonic Speeds, Control: Elevon (δe)

Angle of Attack (α)	Mach Number	δe	$CL_{\delta e}$
-1	0.3	-20	0.06
0	0.3	-20	0.06
2	0.3	-20	0.07
4	0.3	-20	0.07
6	0.3	-20	0.08
8	0.3	-20	0.08
10	0.3	-20	0.09
12	0.3	-20	0.1

Angle of Attack (α)	Mach Number	δe	$CL_{\delta e}$
-1	0.3	-10	0.03
0	0.3	-10	0.03
2	0.3	-10	0.03
4	0.3	-10	0.04
6	0.3	-10	0.04
8	0.3	-10	0.04
10	0.3	-10	0.05
12	0.3	-10	0.05
-1	0.3	0	0
0	0.3	0	0
2	0.3	0	0
4	0.3	0	0
6	0.3	0	0
8	0.3	0	0
10	0.3	0	0
12	0.3	0	0
0	0.3	10	-0.03
2	0.3	10	-0.03
4	0.3	10	-0.04
6	0.3	10	-0.04
8	0.3	10	-0.04
10	0.3	10	-0.05
12	0.3	10	-0.05
0	0.3	20	-0.06
2	0.3	20	-0.06
4	0.3	20	-0.06
6	0.3	20	-0.07
8	0.3	20	-0.07
10	0.3	20	-0.08
12	0.3	20	-0.08
0	0.7	-20	0.07
2	0.7	-20	0.08
4	0.7	-20	0.08
6	0.7	-20	0.09
8	0.7	-20	0.1
10	0.7	-20	0.1
12	0.7	-20	0.11

Angle of Attack (α)	Mach Number	δe	$CL_{\delta e}$
0	0.7	-10	0.03
2	0.7	-10	0.04
4	0.7	-10	0.04
6	0.7	-10	0.04
8	0.7	-10	0.05
10	0.7	-10	0.05
12	0.7	-10	0.06

Angle of Attack (α)	Mach Number	δe	$CL_{\delta e}$
0	0.7	10	-0.03
2	0.7	10	-0.03
4	0.7	10	-0.03
6	0.7	10	-0.04
8	0.7	10	-0.04
10	0.7	10	-0.04
12	0.7	10	-0.05
0	0.7	20	-0.07
2	0.7	20	-0.06
4	0.7	20	-0.06
6	0.7	20	-0.07
8	0.7	20	-0.07
10	0.7	20	-0.08
12	0.7	20	-0.08

$$C_L = -5.1\times10^{-4} + 10^{-3}\times\alpha - 1.4\times10^{-4}\times\alpha\times\delta e + 1.3\times10^{-3}\times\alpha\times M - 8.6\times10^{-4}\times M\times\delta e$$

(3-11)

where α is the angle of attack, δe is the elevon deflection angle, and M is the flight Mach number. The same routine is applied to all lookup tables to find analytical expressions for each aerodynamic coefficient. Optimization of the fitting results and correspondent observed output data, based on the value of sum of square errors (SSE), reveals that the best point to break subsonic and supersonic regimes is at M=1.25 not M=1.0. The minimum SSE can be achieved by choosing M=1.25 instead

of M=1. The effect of the breaking point selection is more significant on lift and drag coefficients than other aerodynamic coefficients. The aerodynamic model with a breaking point at M=1.0 overestimates the lift and drag coefficients up to 100%. The important point in this observation is that it is not valid for high angles of attack. In fact, the angle of attack is very small at hypersonic flight conditions. The same observation is made for supersonic and hypersonic speed regimes. The best point to switch between supersonic and hypersonic regimes is at M=4.0, not at M=5.0. The aerodynamic model breaking point at M=5.0 underestimates the lift coefficients up to 50%. Selections of the breaking point does not have any significant effect on other aerodynamic coefficients. Interestingly the formation of predefined fitting function $\nu(\bar{X})$ has little effect on the breaking points selection. The MATLAB function that represents the analytical aerodynamic model of the GHV is available in Appendix B.

3.8. Summary

An overview of the aerodynamic characteristics, along with the process for developing an aerodynamic database for the Generic Hypersonic Vehicle (GHV), is presented in this section. The experimental investigation of the aerodynamic characteristics for the body of the GHV is used as the core of the simulation model. The gaps in the wind tunnel data have been filled using the best available CFD results. The CFD results are compared with the equivalent wind tunnel data for authenticity. The expressions for the aerodynamic forces and the aerodynamic coefficients acting on the GHV are developed. The aerodynamic database covers the range of flight Mach numbers, angles of attack, sideslip angles, and control surface deflections. The aerodynamic model is used for the simulation of the GHV.

Chapter 4: Propulsion System

4.0. Introduction

The propulsion system model is a fundamental part of the six degrees of freedom vehicle simulation (see equations (2-34) and (2-41)). In this chapter, the design procedure for the propulsion system of a generic hypersonic vehicle (GHV) is presented. Horizontal take-off and horizontal landing vehicles continue to be a subject of great interest for future space launch missions. For a hypersonic vehicle operating through all Mach regimes a combined-cycle propulsion system is the most promising concept. The propulsion model for this research is developed using a 2-D forebody, inlet, and nozzle code, and a 1-D isolator and burner code. The code analyzes the entire vehicle with forebody, inlet, and nozzle flows calculated assuming a 2-D perfect gas. The burner performance characteristics are computed using a 1-D flow with liquid hydrogen combustion. The cycle analysis of the isolator and combustor is conducted using Rayleigh flow principles. The nozzle flow and dimensions are determined applying the method of characteristics. A X-43A type hypersonic vehicle (Hyper-Hawk) is designed and used as a generic vehicle for the design and simulation of hypersonic propulsion systems. Figures 16 and 17 show 2-D and 3-D models of the compression system. In the GHV model, the forebody shock impinges at the leading edge of the cowl and interacts with the local shock wave and generates a shock-shock interaction. In the design process, the deflection angles of the compression system can be adjusted for any research vehicle.

Figure 16: 2-D View of the External-Internal Compression System (Hyper-Hawk)

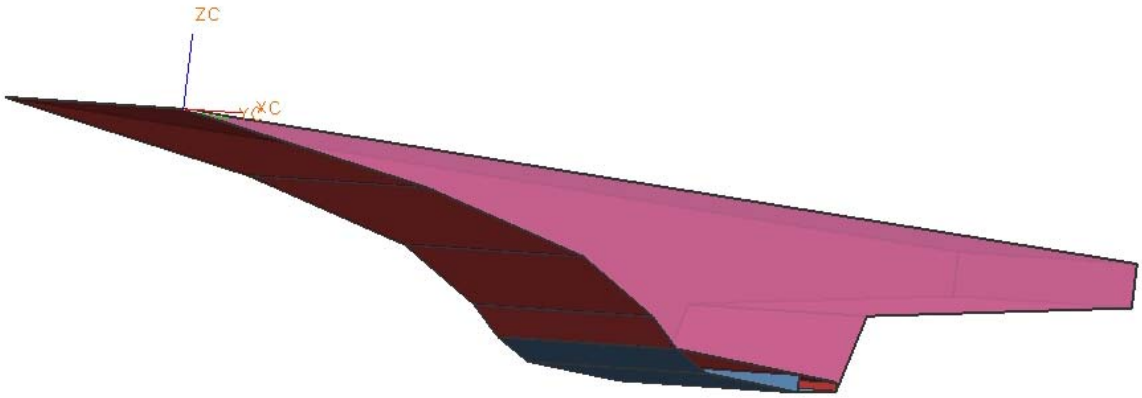

Figure 17: 3-D View of the Hyper-Hawk

4.1. Ramjet-Scramjet Performance Analysis

4.1.0. Definitions and Technical Background

The most effective way for analyzing of airbreathing hypersonic engines is to establish reference stations at critical axial positions along the engine flowpath. Each property of the flow can be represented by a value at each reference station. Figure 18 shows the reference stations used in the Hyper-Hawk. It is assumed that when the value of any two independent intensive thermodynamic properties is fixed the values of all other intensive thermodynamic properties are determined (the pure substance

assumption). The flow is compressed adiabatically from the freestream T_0 to T_3. This process is adiabatic but it is not isentropic.

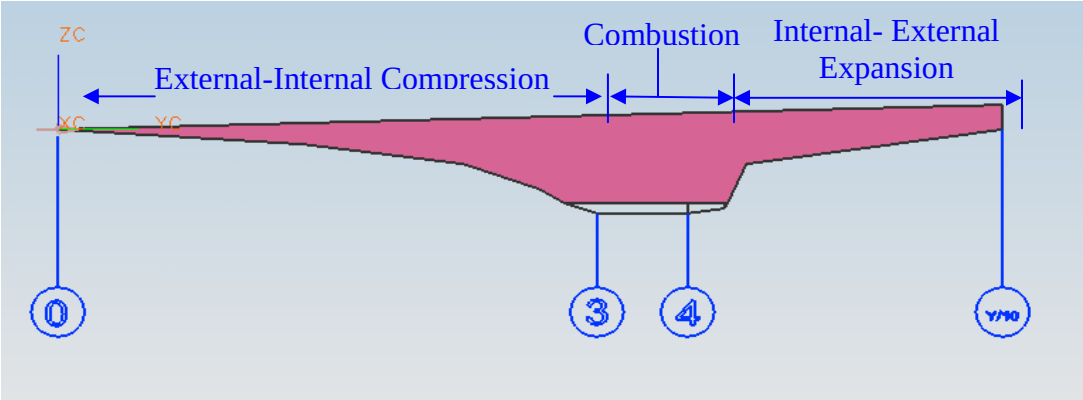

Figure 18: Reference Stations

The flow entropy is increased because of the shock waves and other losses like skin friction. Between station 3 and station 4, a frictionless heat is added to a constant static pressure flow. An adiabatic expansion occurs in the expansion nozzle (station 4 to station 10). The thermodynamic cycle is closed and occurs in a constant static pressure.

4.1.1. Compression System Limitations

The stagnation temperature of the inlet adiabatic flow is given by:

$$T_t = T_0\left(1+\frac{\gamma-1}{2}M^2{}_0\right) = T_3\left(1+\frac{\gamma-1}{2}M^2{}_3\right) \qquad (4\text{-}1\text{-}a)$$

The Burner entry Mach number can be used to find the limit on the compression temperature. From equation (4-1-a), the burner entry Mach number is calculated as:

$$M_3 = \sqrt{\frac{2}{\gamma-1}\left\{\frac{T_0}{T_3}\left(1+\frac{\gamma-1}{2}M^2{}_0\right)-1\right\}} \qquad (4\text{-}1\text{-}b)$$

where, $\frac{2}{\gamma-1} > 0$

$$\left\{\frac{T_0}{T_3}\left(1+\frac{\gamma-1}{2}M^2{}_0\right)-1\right\}=0 \qquad (4\text{-}1\text{-}c)$$

The solution of equation (4-1-c) for M_0 becomes,

$$M^2{}_0\left(\frac{2}{\gamma-1}\right)=\frac{T_3}{T_0} \qquad (4\text{-}1\text{-}d)$$

if $M_0 < \sqrt{\frac{2}{\gamma-1}\left(\frac{T_3}{T_0}-1\right)}$, then no solution exists for M_3. (4-1-e)

Secondly, when

$$M_0 > \sqrt{\frac{2}{\gamma-1}\left\{\frac{T_3}{T_0}\left(1+\frac{\gamma-1}{2}\right)-1\right\}} \qquad (4\text{-}2)$$

Then the flow entering the burner should remain supersonic or supersonic combustion (scramjet cycle) is inevitable.

Another observation from equation (4-1-a) reveals that:

$$\frac{M^2{}_3}{M^2{}_0} \approx \frac{T_0}{T_3} \qquad (4\text{-}3\text{-}a)$$

$$\frac{M_3}{M_0} \approx \sqrt{\frac{T_0}{T_3}} \qquad (4\text{-}3\text{-}b)$$

this ratio is approximately a constant the following condition:

$T_0 \approx 218$ K

$\left(T_3\right)_{max} \approx 1600$ K

$$\frac{M_3}{M_0} \cong \sqrt{\frac{T_0}{T_3}} \cong 0.37 \qquad (4\text{-}4)$$

The burner Mach number is restricted by equations (4-2) and (4-4). This shows that the limit on the compression temperature leads directly to the burner entry Mach number [18].

4.1.2. Hypersonic Shock Relations

As shown in Figure 19, the freestream flow goes through a series of shock waves on the underbody of the vehicle. The underbody flow is modeled by applying shock wave theory. For a thermally and calorically perfect gas, the shock wave equations can be written in term of γ and the normal component of the upstream Mach number (M_{1n}).

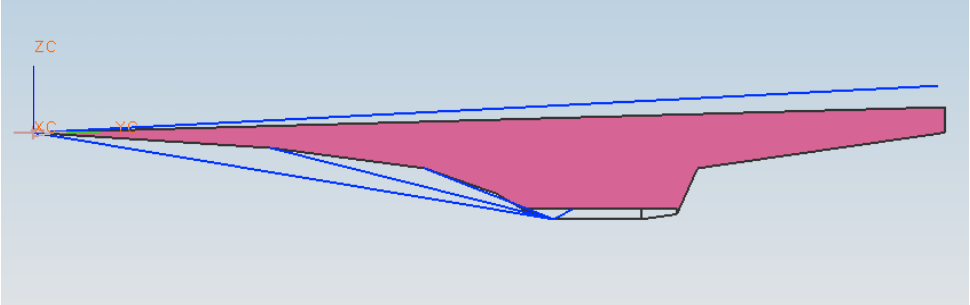

Figure 19: Shock Waves

Consider the flow through a straight oblique shock wave, shown in Figures 19 and 20. Upstream and downstream conditions are denoted by the subscript 1 and 2, respectively. For a calorically perfect gas, the classical results for change across the shock are given as:

$$\frac{\rho_2}{\rho_1} = \frac{(\gamma+1)M_{1n}^2}{(\gamma-1)M_{1n}^2+2} \tag{4-5}$$

$$\frac{P_2}{P_1} = 1+\frac{2\gamma\left(M_{1n}^2-1\right)}{(\gamma+1)} \tag{4-6}$$

$$\frac{T_2}{T_1} = \frac{a_2^2}{a_1^2} = 1 + \frac{2(\gamma - 1)\left(M_{1n}^2 - 1\right)}{(\gamma + 1)^2 M_{1n}^2}\left[\gamma M_{1n}^2 + 1\right] \tag{4-7}$$

$$\frac{s_2 - s_1}{c_v} = \ln\left[\frac{P_2}{P_1}\left(\frac{\rho_2}{\rho_1}\right)^{-\gamma}\right] \tag{4-8}$$

$$M_{1n} = M_1 \times \sin\beta \tag{4-9}$$

The Mach number downstream of the shock is given by:

$$M_{2n}^2 = \frac{2 + (\gamma - 1)M_{1n}^2}{2\gamma M_{1n}^2 - (\gamma - 1)} \tag{4-10}$$

The velocity vectors are obtained from these geometrical relations as:

$$V_1 \cdot \hat{n} = V_1 \sin\beta \tag{4-11}$$

$$V_2 \cdot \hat{n} = V_2 \sin(\beta - \theta) \tag{4-12}$$

where β is the wave angle.

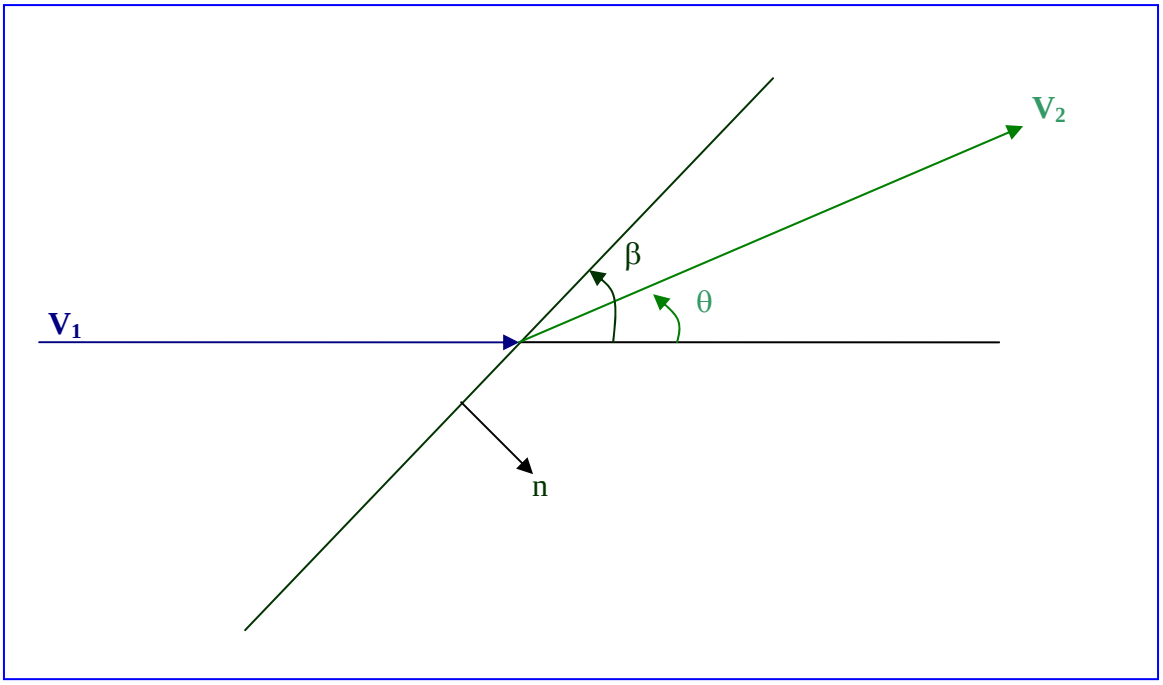

Figure 20: Local Shock Angle and Flow-deflection Angle for an Oblique Shock

The relation between β and θ is given by:

$$\frac{\tan(\beta-\theta)}{\tan(\beta)} = \frac{\gamma+1}{2} M_1^2 \frac{\sin\beta\sin\theta}{\cos(\beta-\theta)} \tag{4-13}$$

In the limit as M_1 goes to infinity then,

$$M_{1n}^2 = \left(M_1{}^2 \times \sin^2\beta\right) \gg 1 \tag{4-14}$$

Hence equations (4-4) through (4-7) become:

$$\frac{\rho_2}{\rho_1} \cong \frac{(\gamma+1)}{(\gamma-1)} \tag{4-15}$$

$$\frac{P_2}{P_1} \cong \frac{2\gamma\left(M^2{}_1 \times \sin^2\beta\right)}{(\gamma+1)} \tag{4-16}$$

$$\frac{T_2}{T_1} \cong \frac{2\gamma(\gamma-1)\left(M_1^2 \times \sin^2\beta\right)}{(\gamma+1)^2} \tag{4-17}$$

A MATLAB routine is written to calculate external and internal compression and the underbody flow at supersonic through hypersonic speeds using the hypersonic shock relations. The routine is designed to respond to the angle of attack.

4.2. Cycle Analysis

In hypersonic engine cycle analysis there are important definitions which are discussed in this subsection. The cycle static temperature ratio (ψ) is defined as:

$$\psi = \frac{T_3}{T_0} \tag{4-18}$$

This ratio is the principle determinant of thermodynamic cycle efficiency. T_3 is limited to a value that prevents excessive dissociation in the exhaust flow. In this research, T_3 is kept within the range 1,400–1,650 K. The maximum allowable temperature should be determined case by case, and this range should not be taken as

a universal range. The static temperature of the flow is increased by the underbody compression process. This change in the flow's static temperature causes a change in the constant specific heats ratio. For an accurate mathematical manipulation, γ is calculated at each reference. From the Gibbs equation and the adiabatic compression process, the burner entry pressure is given as:

$$\frac{P_3}{P_0} = \left(\frac{T_3}{T_0}\right)^{\left(\frac{C_p}{R}\right)} = (\psi)^{\left(\frac{C_p}{R}\right)} \tag{4-19}$$

The principles of the conservation energy and mass are used to calculate V_3 and area ratio $\frac{A_3}{A_0}$. The combustion energy release is modeled as heat addition via mass addition. The relation between burner entry and exit temperatures for constant pressure combustion is [18]:

$$\frac{T_4}{T_3} = \frac{1}{1+f}\left\{1+\frac{1}{C_{p-Burner}\cdot T_3}\left[\eta_{Burner}\cdot f\cdot h_{PR} + f\cdot h_f + f.C_{p-Burner}T^{\circ} + \left(1+\frac{V_f^2}{V_3^2}\right)\times\frac{V_3^2}{2}\right]\right\}\ldots$$

$$-\frac{V_4^2}{2C_{p-Burner}} \tag{4-20}$$

T° is the absolute static enthalpy estimate $\left(T^{\circ} = 220\,K\right)$. The burner area ratio is calculated using the static temperature ratio of the burner as follows:

$$\frac{A_4}{A_3} = (1+f)\cdot\tau_{Burner}\cdot\frac{V_3}{V_4}$$

$$\text{where } \tau_{Burner} = \frac{T_4}{T_3} \tag{4-21}$$

The expansion process is assumed adiabatic process which results in the component analysis as [18]:

$$T_{10} = T_4 \left\{ 1 - \eta_{expansion} \left[1 - \left(\frac{P_{10}}{P_0} \cdot \frac{P_0}{P_4} \right)^{\left(\frac{R}{C_{p-expansion}} \right)} \right] \right\} \quad (4\text{-}22)$$

$$V_{10} = \sqrt{V_4^2 + 2C_{p-expansion}\left(T_4 - T_{10}\right)} \quad (4\text{-}23)$$

where $\eta_{expansion}$ is the nozzle expansion efficiency.

The stream thrust function is,

$$Sa_{10} = V_{10}\left(1 + \frac{R \cdot T_{10}}{V_{10}^2}\right) \quad (4\text{-}24)$$

For an ideal expansion in the exhaust nozzle , $P_{10}=P_0$, with constant caloric properties which gives:

$M_{10}=M_0$ (4-25)

Because of heat addition in the combustor, the T_{10} in the ejector is much higher than the ambient temperature T_0. The velocity ratio V_0/V_{10} for the ideal cycle becomes:

$$\frac{T_{t4}}{T_0} = 1 + \frac{q}{C_p T_0} \frac{1}{1 + \frac{\gamma - 1}{2} M^2{}_0} \quad (4\text{-}26)$$

$$\frac{V_{10}}{V_0} = \sqrt{\frac{T_{10}}{T_0}} \overset{\text{Adiabatic Process}}{=} \sqrt{\frac{T_4}{T_0}} = \sqrt{\frac{T_{t4} \diagup T_{t0}}{1 + \frac{\gamma - 1}{2} M^2{}_0}} = \sqrt{1 + \frac{q}{C_p T_{t0}}} = \sqrt{1 + \frac{q}{C_p T_0} \frac{1}{1 + \frac{\gamma - 1}{2} M^2{}_0}} \quad (4\text{-}27)$$

For the non-ideal cycle, equation (4-20) becomes:

$$\sqrt{\frac{T_{10}}{T_0}} = \sqrt{1 + \frac{q}{C_p T_0} \frac{\eta_{th}}{1 + \frac{\gamma - 1}{2} M^2{}_0}} \quad (4\text{-}28)$$

where,

$$\eta_{th} = \eta_n \left[1 - \frac{1 + \frac{\gamma - 1}{2} M^2_3}{1 + \frac{\gamma - 1}{2} M^2_0} \left\{ 1 + (1 - \eta_K) \frac{\gamma - 1}{2} M_0^2 \right\} \right] - \frac{\frac{\gamma - 1}{2} M^2_0}{\frac{q}{C_p T_0}} (1 - \eta_K \eta_n) \qquad (4\text{-}29)$$

The exhaust nozzle performance is defined as:

$$\eta_n = \frac{V^2_{10}}{(V_{10})^2_{isontropic}} \qquad (4\text{-}30)$$

A representative value of η_K is chosen as: η_K=0.90 for ramjet combustion and η_K=0.98 is used for scramjet combustion [21]. The value for η_K can also be calculated using Waltrup model by the relation:

$$\eta_K = 1 - 0.4 \left(1 - \frac{M_3}{M_0} \right)^4 \qquad (4\text{-}31)$$

A MATLAB program (***Analysis.m***) was written to find the flow properties at the different stations.

4.3. Ramjet-Scramjet Compression Performance

One of the most challenging tasks in the design of a ramjet-scramjet engine is to find an efficient underbody compression system. The performance of the hypersonic inlet is investigated using oblique shock theory (Section 4.1.2). The total pressure recovery (ratio), π_d, across the compression system is defined as the ratio of the total pressure at the burner inlet entry to the total pressure of the freestream flow. The total pressure ratio is an important measure of the performance of the compression system. The kinematic energy efficiency is another key performance property which is defined as:

$$\eta_d = \left(\frac{V_{ii}^{\ 2}}{V_0^2} \right) \tag{4-32}$$

The MATLAB program, EX_IN_COMP.m, is used to calculate these performance parameters for any compression system that incorporates up to four oblique shocks. The total pressure ratio is universally accepted as the meaningful measurement of performance for subsonic and supersonic aircraft compression systems. A comparison of the two existing inlet pressure recovery models (AIA standard and MIL E-5008B standard) with the MATLAB routine (EX_IN_COMP.m) is shown in Figure 21 [19]. Both standards yield more conservative results than EX_IN_COMP.m results. The results of hypersonic flight tests show that the total pressure ratio is not valuable measurement in the performance of compression systems. The total pressure ratio is a complicated function of flow conditions not a simple formula. The result of EX_IN_COMP only used to establish trends.

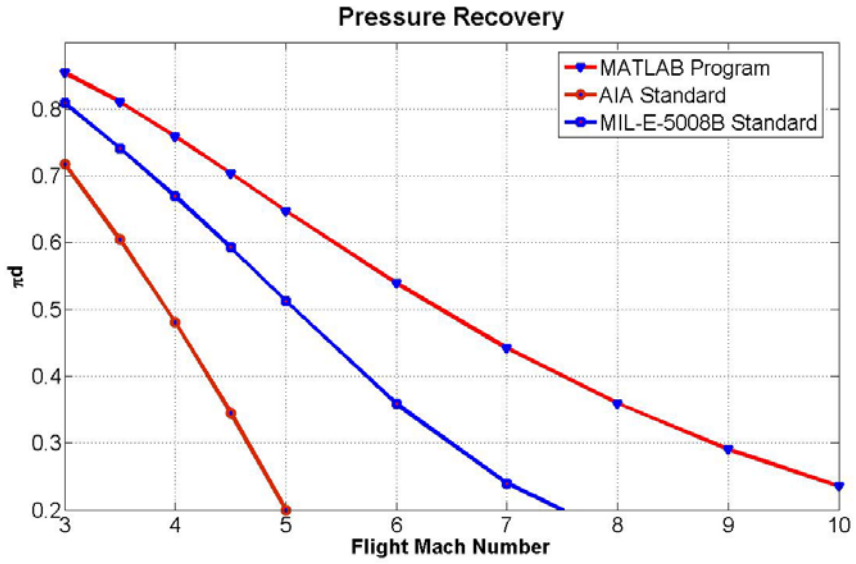

Figure 21: Pressure Recovery Comparison

The effect of angle of attack on the pressure recovery coefficient is investigated next. The shock waves are determined using the angle of attack (AOA), dynamic pressure, the free stream characteristics, and underbody deflection angles. As is shown in Figure 22, the pressure recovery decreases at higher angles of attacks, and it can cause higher static temperature and excessive dissociation in the exhaust nozzle.

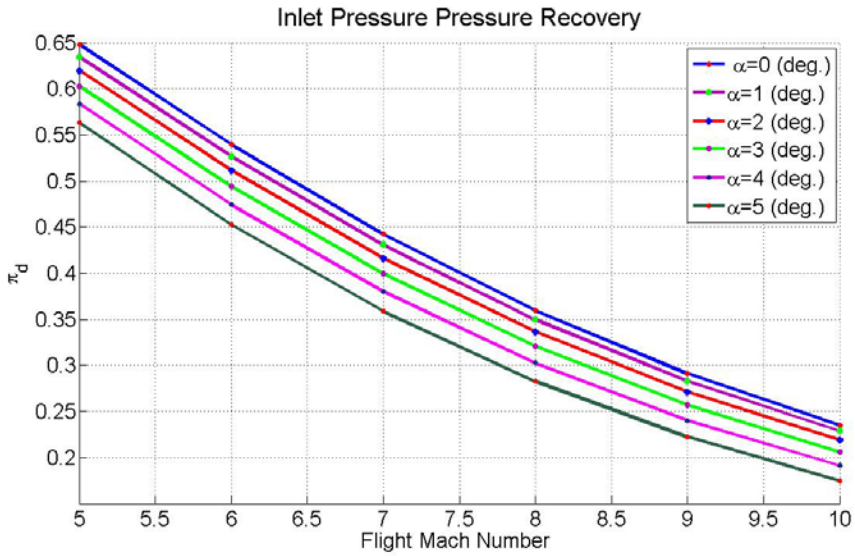

Figure 22: Variation of Pressure Recovery with Angle of Attack

At low hypersonic conditions, when the vehicle's overall angle of attack changes from 0 degrees to 5 degrees, the pressure recovery decreases by up to 9.6%. This variation is not significant at higher hypersonic speeds. At moderate hypersonic speeds, when the vehicle's overall angle of attack changes from 0 degrees to 5 degrees, the pressure recovery decreases by up to 3.0%. The AOA and dynamic pressure also affect the combustion kinetics and the exhaust flow/free stream shear layer. The sensitivity of the engine performance to the AOA and the dynamic pressure is small at high Mach numbers and increases as the speed decreases. At low speeds, the AOA and the dynamic pressure need to be greater than certain values in

order to provide acceptable performance. The optimum operating condition is a function of shockwaves formed on the leading edge and captured by the inlet lip. Therefore, these vehicles will require a variable geometry inlet to operate at or near optimum aerodynamic and propulsion conditions at all times. The generated thrust force may drop dramatically due to lower pressure recovery in high angle of attack. As discussed before, in this class of vehicle and in the absence of a rotary compressor, the underbody of the vehicle performs as the compressor. The performance characteristics of Hyper-Hawk's external-internal compression system at supersonic and hypersonic speeds are shown in the following figures. The burner's static temperature and burner entry Mach number are two important engine performance characteristics. The higher the flight Mach number, the stronger the shock waves become. The burner entry Mach number (M_{bi}) is calculated and shown in Figure 23. The numerical value of M_{bi} indicates the nature of the combustion within the combustor. As it is shown in Figure 23 (with a high performance compression system) the compressed flow enters the burner supersonically (scramjet) at flight Mach numbers M>3. In reality, the performance of the compression system is lower due to off-design shockwave effects. Thus, the burner Mach number reaches sonic speed at a much higher flight Mach number. The kinetic efficiency of the underbody flow in moderate hypersonic speeds changes slightly with the flight Mach number. It means at high flight Mach numbers the overall kinetic efficiency (η_d) is not a primary function of the flight Mach number. To prevent excessive dissociation in the exhaust flow, T_3 needs to be limited to an acceptable range. In this research T_3 is kept in the range of 500K to 1,550 K for flight Mach numbers in the range of from

3 to 10. The burner entry Mach number must be adjusted for different flight conditions to generate maximum performance in the burner and prevent flow dissociation in the exhaust nozzle. In such adiabatic flows, the static temperature ratio (ψ) increases with increasing the flight Mach number because of stronger shock waves and lower burner entry Mach number as described in equation (4-33).

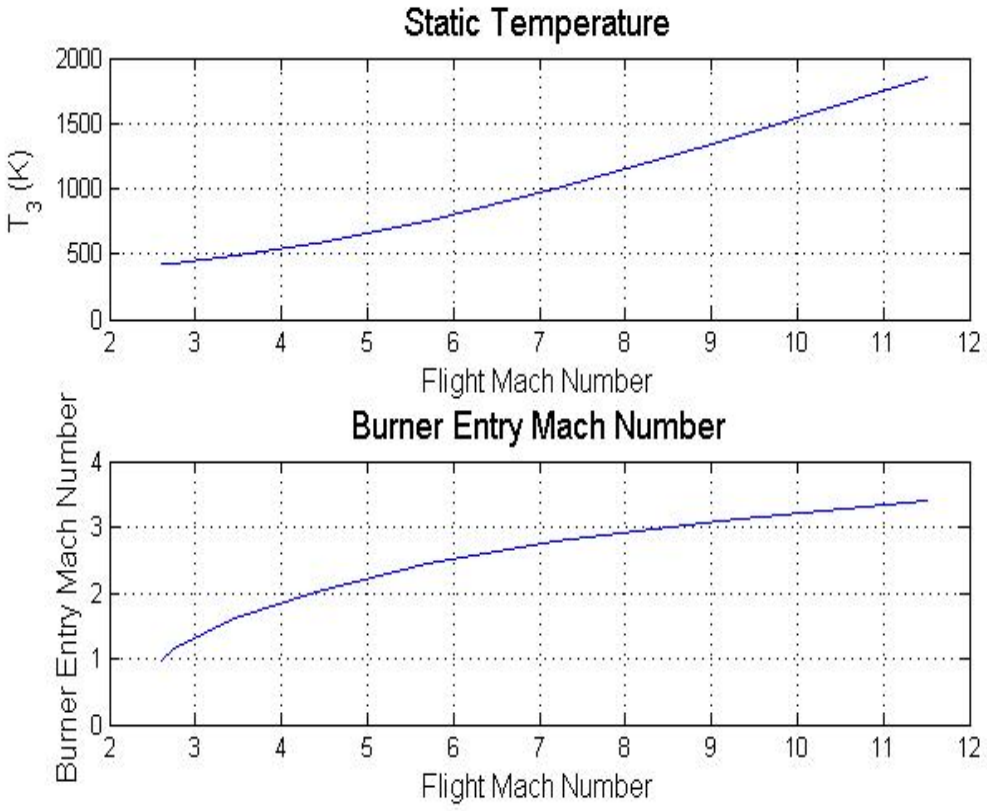

Figure 23: Static Temperature and Burner Inlet Mach Number with Flight Mach Number

$$\psi = \frac{T_3}{T_0} = \frac{1+\frac{\gamma-1}{2}M^2_0}{1+\frac{\gamma-1}{2}M^2_3} \qquad (4\text{-}33)$$

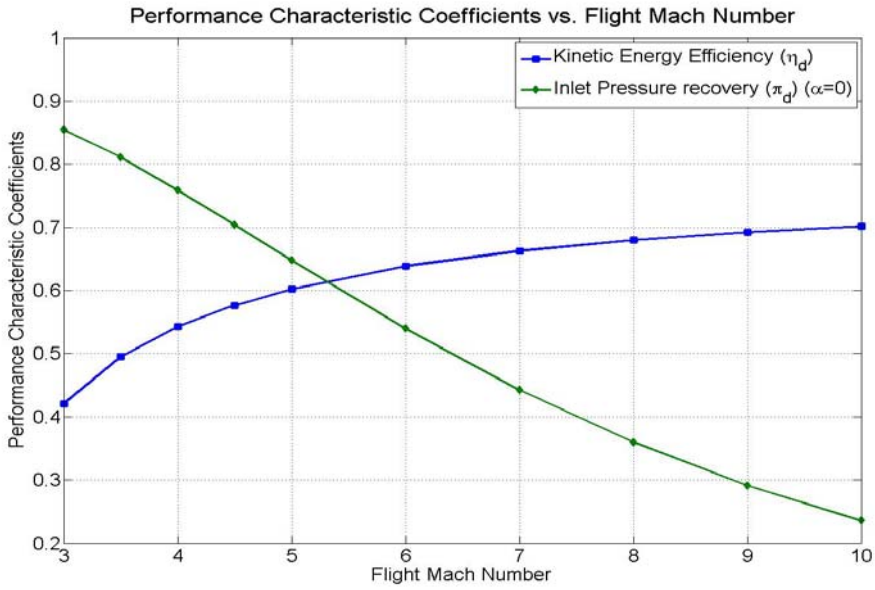

Figure 24: Kinetic Energy Efficiency of the Compression System

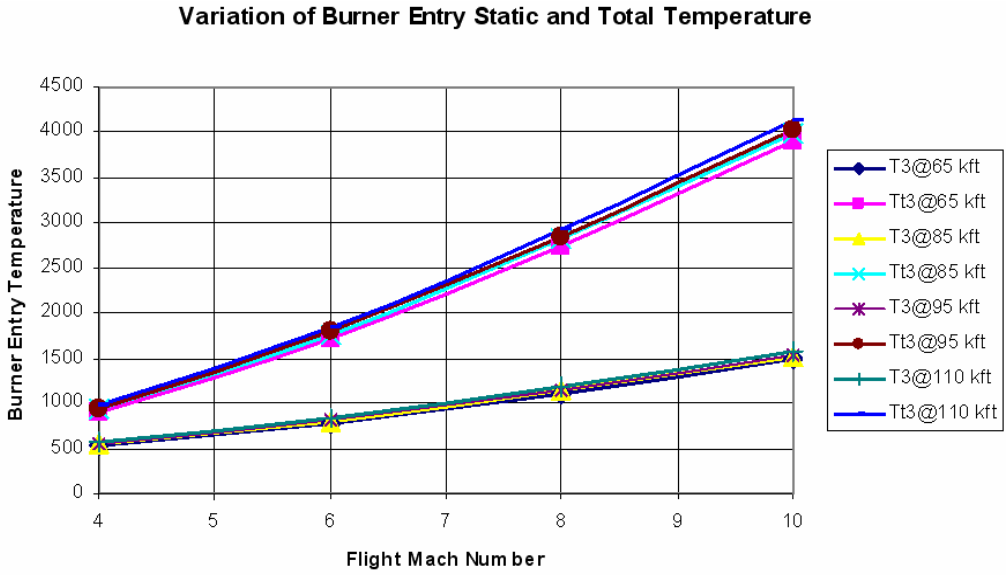

Figure 25: Variation in Burner Static Temperature

Change in the flow's static temperature causes changes in the specific heat at constant pressure (C_P) and the ratio of specific heats (γ). The variation in the burner entry γ and C_P with flight Mach at 85,000 ft is shown in Figure 26. The specific heat at constant pressure (C_P) increases with T_3 as well as the flight Mach number. In the calorically

perfect gas region (up to M_0=4) γ stays constant. At higher flight Mach number (M_0>4) γ decreases with flight Mach number and T_3 (see Figures 18 and 26). It is very important to calculate variations of γ and C_P with the flow's static temperature at each station. The confidence in the computational tools increases by calculating variations of γ and C_P. Another important burner performance indicator is the adiabatic efficiency.

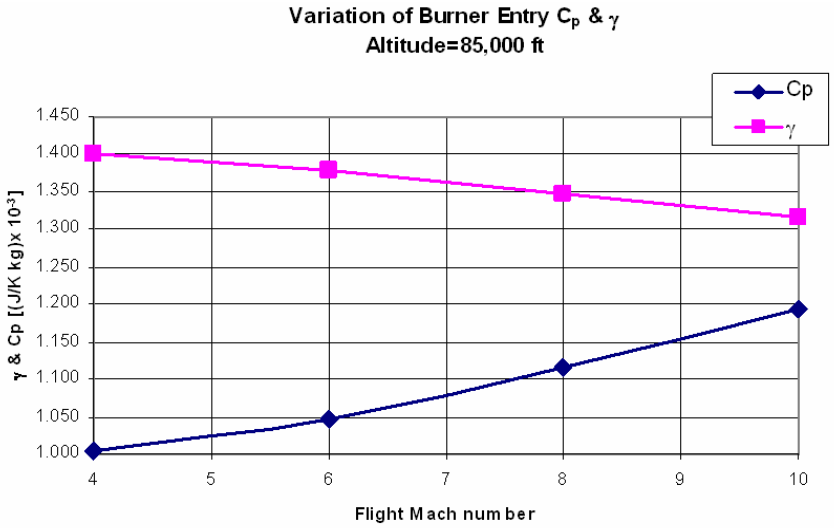

Figure 26: Variation of Burner Entry C_p and γ with Flight Mach Number

The adiabatic performance of the burner is calculated using equation (4-27) and is shown in Figure 27. In equation (4-27) , it is assumed that C_p stays constant between stations 1 and 3.

$$\eta_{Adiabatic} \cong \frac{(T_{t3})_{iso} - (T_3)}{(T_{t3}) - (T_3)} \qquad (4\text{-}34)$$

As it is shown in Figure 27, the loss can be substantial at high hypersonic speeds. Close observation of Figures 23 through 27 helps to find an optimized underbody geometry and configuration for the vehicles which minimizes the loss at hypersonic

speeds. Making the intake very long can be a very good way to fix this problem. Very shallow shock wave angles appropriate to hypersonic speeds. A long intake creates thick boundary layers especially at high altitudes. These boundary layers generate flow uniformly case lower pressure recovery. Furthermore, the recovery temperature at the wall below the boundary layer is near stagnation.

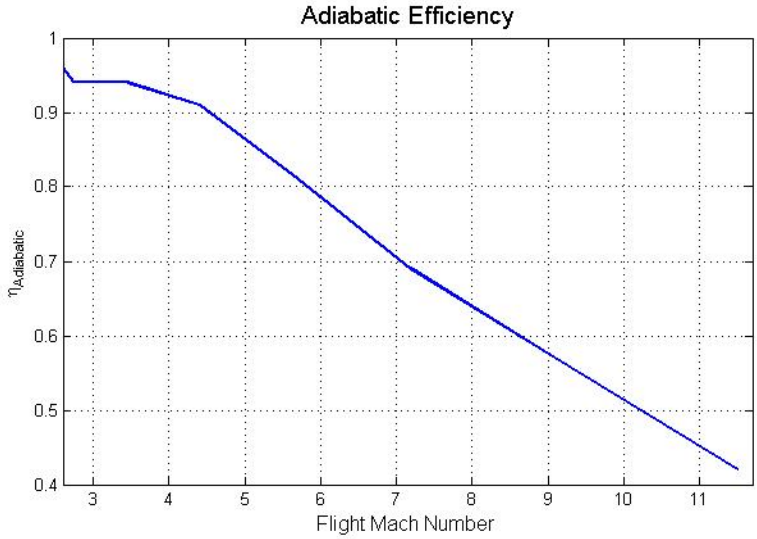

Figure 27: Adiabatic Efficiency

4.4. Ramjet-Scramjet Frictionless Constant Pressure Burner

In this research, hydrogen and air are used as the fuel and the oxidizer. The equations for complete combustion (stoichiometry) and the stoichiometry fuel air ratio are given as:

$$C_x H_y + \left(x + \frac{y}{4}\right)\left(O_2 + \frac{79}{21}N_2\right) \rightarrow x\,CO_2 + \frac{y}{2}H_2O + \frac{79}{21}\left(x + \frac{y}{4}\right)N_2 \qquad (4\text{-}35)$$

$$f_{st} = \frac{36x + 3y}{103(4x + y)} \qquad (4\text{-}36)$$

$$\text{For hydrogen}: x = 0 \,\&\, y = 2 \Rightarrow f_{st} = \frac{36(0)+3(2)}{103(4(0)+(2))}$$

$f_{st} =$ 0.0291 or 2.91%

$$\phi = \frac{f}{f_{st}} \tag{4-37}$$

Ramjet engines need two geometric constraints (throats). The first throat brings the flow into the burner at subsonic speeds. The flow is choked by the second throat and accelerates into the exhaust nozzle. Unlike ramjet engines, scramjet engines have no geometric throat upstream or upstream since the Mach number never drops to or below M=1.0. To avoid requiring two engine types, the concept of a dual mode combustion system was proposed by Curran and Stull [20]. The same concept is used in this research. When the vehicle operates at subsonic speeds, the dual mode combustion system provides subsonic flow either upstream or downstream of the combustor without using throats. The transition from supersonic flow to subsonic flow is accomplished in the dual mode combustion system by means of a constant area diffuser called an isolator. If the flow choked somewhere downstream, it causes a large back pressure at the burner entry. The back pressure in the isolator is generated either by chemical energy release in the burner or by obstructing the fuel injector (or a combination of both). Depending on the burner back pressure, the flow has two different patterns in the isolator. If $M_{ii} < 3$ in the isolator inlet, then the pattern is a normal shock train and the flow is subsonic. In contrast for flows with $M_{ii} > 3$, the oblique shock train generates a supersonic flow that adjusts the static back pressure in the burner [18].

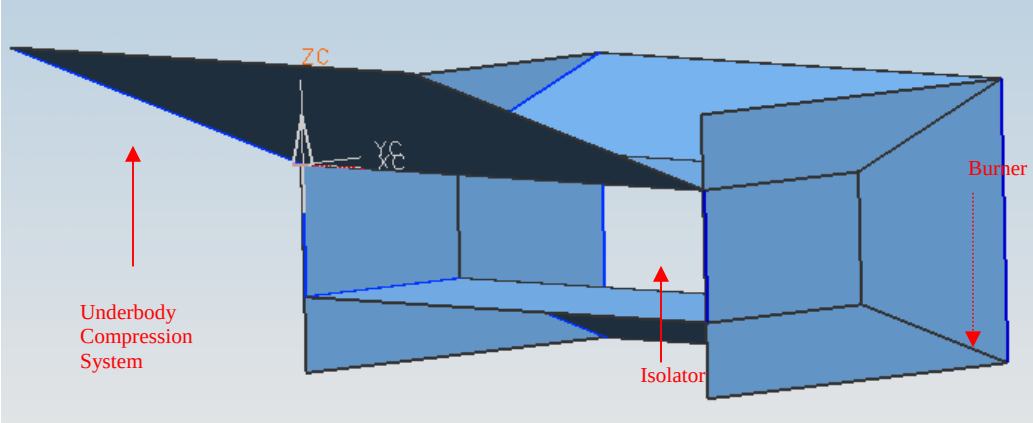

Figure 28: The Isolator and Burner

The impulse function at the isolator exit is given by:

$$I_{ie} = P_{ie}A_{ii} + \rho_{ii}V_{ii}A_{ii}V_{ie} = P_{ie}A_{ii} + \rho_{ie}A_{ie}V_{ie}^{\ 2} \tag{4-38}$$

$$M_{ie} = \left\{ \frac{\gamma_b^{\ 2}M_{ii}^2\left(1+\frac{\gamma_b+1}{2}M_{ii}^2\right)}{\left(1+\gamma_b^{\ 2}M_{ii}^2-\frac{P_{ie}}{P_{ii}}\right)^2} - \left(\frac{\gamma_b-1}{2}\right) \right\}^{-1/2} \quad \text{where } M_{ie} = M_{bi} \tag{4-39}$$

The Mach number at the isolator exit is calculated using equation (4-23). Both the temperature and pressure increase in the burner due to chemical reactions. In order to keep the pressure constant, the area ratio needs to be increased. For a quasi-one-dimensional frictionless heat addition at a constant pressure, the axial variation of Mach number is given as follows [18]:

$$\tau(x) = \frac{T_{t\_burner}(x)}{T_{t\_ii}(x)} \tag{4-40}$$

$$M(x)_{burner} = \frac{M_{bi}}{\sqrt{\tau(x)\left(1+\frac{\gamma_b-1}{2}M_{bi}^{\ 2}\right)-\left(\frac{\gamma_b-1}{2}\right)M_{bi}^{\ 2}}} \tag{4-41}$$

In a constant pressure burner the density decreases $\left(P=\rho\cdot R\cdot T\right)$ and the static temperature rises. Because T is proportional to the square of the speed of sound $\left(a^2\right)$, the Mach number falls in proportion to the $\sqrt{A}$. The burner area profile must be designed to maintain a constant burner pressure. The burner area ratio is proportional to $\tau(x)$.

$$A\left(x\right)_{burner}=A_{bi}\left[\tau\left(x\right)\left(1+\frac{\gamma_b-1}{2}M_{bi}^{\ 2}\right)-\left(\frac{\gamma_b-1}{2}\right)M_{bi}^{\ 2}\right] \qquad (4\text{-}42)$$

A MATLAB program (***Burner.m***) is written to do analytical analysis for the isolator and the burner. The burner model program is run for various temperature ratios at multiple altitudes. Figures 29 and 30 show the results for different runs.

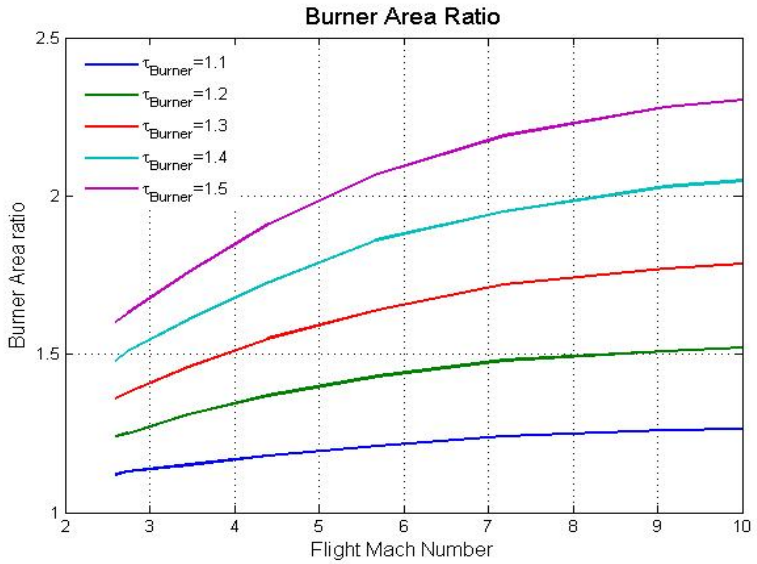

Figure 29: Burner Area Ratio

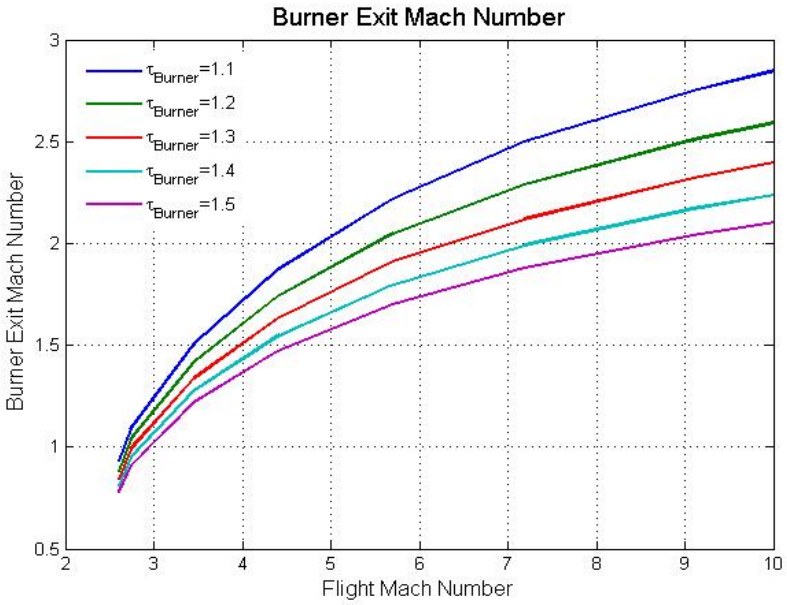

Figure 30: Burner Exit Mach Number

As was shown, the burner area ratio varies with the flight Mach number as a direct function of the burner total temperature ratio, τ_{Burner}. The higher the total temperature ratio the larger the area ratio required to keep the pressure constant. A larger area ratio expands the flow. Because of this the flows exits the burner at a lower Mach number.

An interesting observation is the direct proportionality between the area ratio and τ_{Burner}. This is a disadvantage for constant pressure burners operation. Another disadvantage to a constant pressure burner is the resulting lower value of $\left(\frac{P_{t4}}{P_{t3}}\right)$ at the same value of τ_{Burner}. The area ratio needs to be adjusted in response to varying altitude, flight Mach number, and τ_{Burner}. Keeping the burner pressure constant by using “infinitely variable” geometry or “rubber” burner is almost impossible using. Smart materials and adaptive structures are potential advanced propulsion

technologies to provide the required variable engine geometry. Other advances in materials, cooling techniques, and aerodynamics, can potentially also provide performance improvements. The results of applying advanced propulsion technologies are presented in terms of improvement in the overall system performance. Figure 31 shows the relationship between the burner total temperature ratio, τ_{Burner}, and the exit Mach number. The burner characteristic properties, including the total temperature ratio $\tau(x)$ and the area ratio $A(x)$, can be adjusted for any specific design criteria. The fuel air ratio and the fuel equivalence ratio are calculated at different total temperature ratios and the results are plotted in Figure 31.

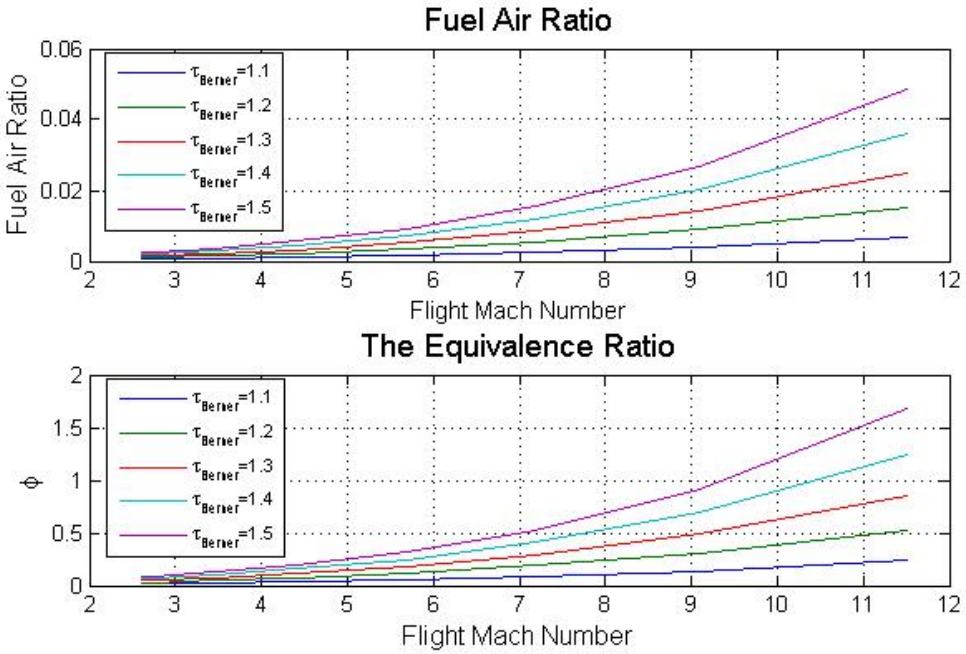

Figure 31: Fuel Air Ratio and Fuel Equivalence Ratio

The fuel equivalence ratio exceeds the stoichiometric mixture of hydrogen and air and become a fuel-rich mixture (ϕ>1) at high temperature ratios and high flight Mach numbers (τ>1.4 and M>10). In many cases, a fuel-rich mixture is desired since it

increases the cooling capacity of the engine. The variation in the heat input "q" per unit air mass flow rate and the heat parameter, q/CpT_0, are shown in Figure 32. The performance of the engines can be estimated using the heat parameter. This allows the performance of the engine to be calculated independence of the fuel type.

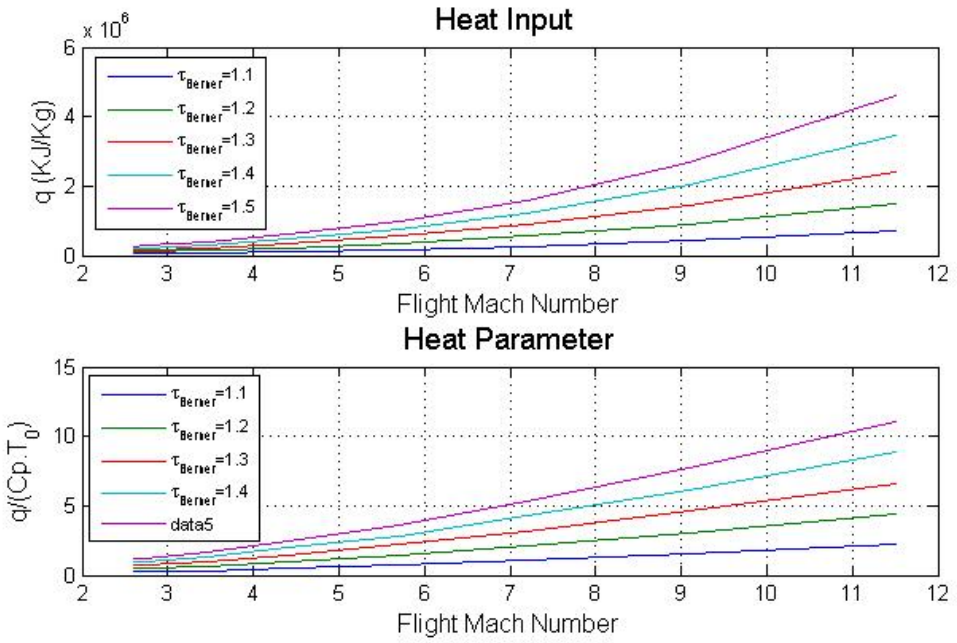

Figure 32: Heat Input and Heat Parameter

The combustor's back pressure $\left(\frac{P_{t4}}{P_{t0}}\right)$ is a function of the heat parameter. Depending on the value of the heat parameter, the flow displays two different patterns in the combustor. The combustion may take place subsonically or supersonically. The concept of a dual-fuel combustion system can be a very interesting research subject. The dual-fuel combustion system might be used to provide subsonic flow, either upstream or downstream of the combustor, without using throats. The ratio of specific heats (γ) decreases, and the specific heat at constant pressure (C_P) increases, with e

increasing static temperature within the burner. The effect of changing (γ) and (C_P) on engine performance is substantial. The confidence in the computational tools that are used in the propulsion systems analysis is increased by checking the variations in (γ) and (C_P) at each station.

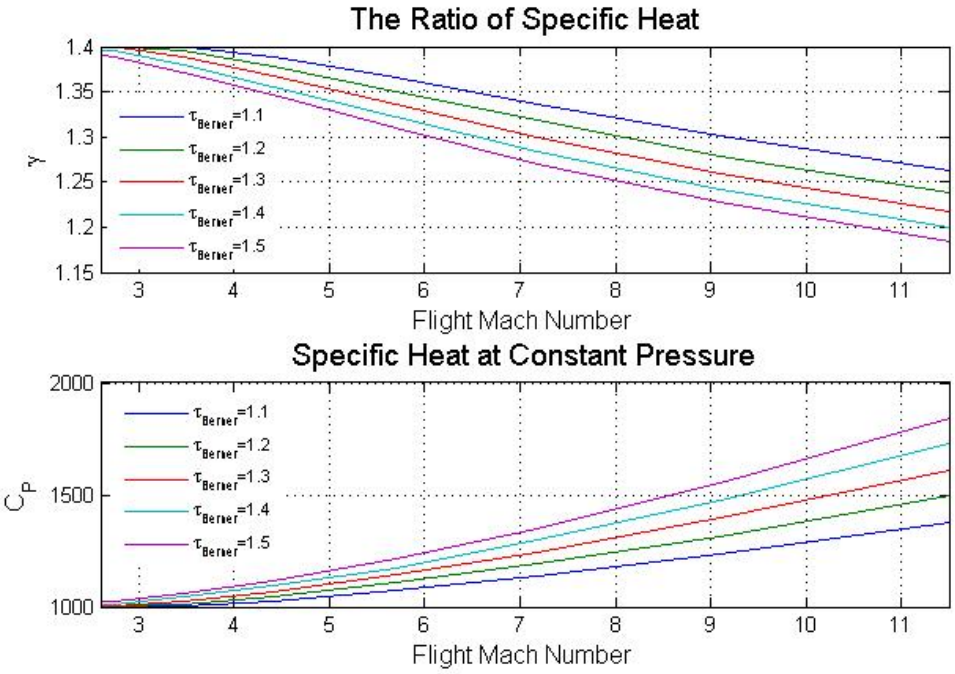

Figure 33: Specific Heat

In the design of burner, it is important to keep the additional heat lower than the limit. The addition of heat within the combustion chamber is often limited by the choking of the exit area. For the constant pressure case, in supersonic flow the Mach number decreases ($M_4 < M_3$). The limiting heat condition for choked flow is given by the expression:

$$\frac{q_{lim}}{C_p T_{t0}} = \frac{\left(M^2{}_3 - 1\right)^2}{2\left(\gamma + 1\right) M^3{}_2} \quad \text{for } M_3 > 1 \qquad (4\text{-}43)$$

Figures 34 through 36 show that at low to moderate supersonic flight Mach numbers and with $1.3 < \tau_{burner} < 1.5$, the heat addition exceeds the limiting heat addition.

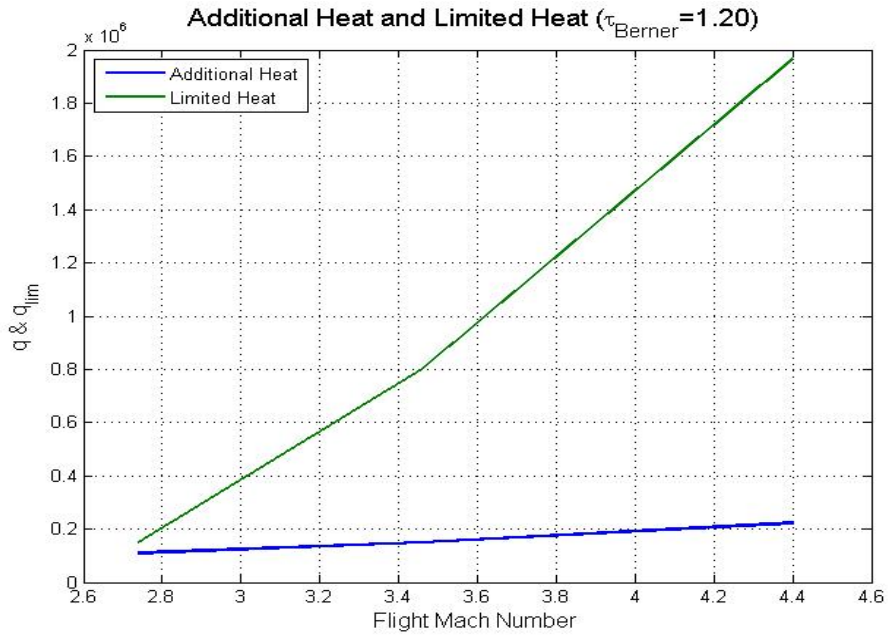

Figure 34: Heat Addition and Heat Limit (τ_{Burner}=1.20)

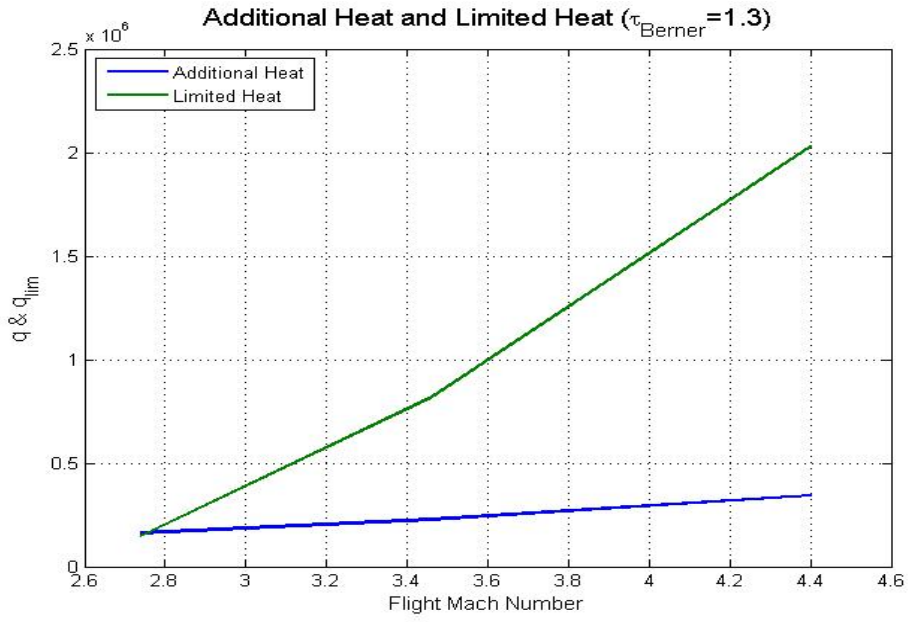

Figure 35: Heat Addition and Heat Limit (τ_{Burner}=1.30)

For the case where $\tau_{Burner} = 1.4$, the additional heat reaches the limit at Mach = 2.84. A solution to this problem is to adjust τ_{Burner} with flight Mach number. This allows more heat to be added to the flow at higher flight Mach numbers. An adjustable τ_{Burner} as a function of flight Mach number can increase the overall performance of the engine substantially. This can be potentially another important research topic.

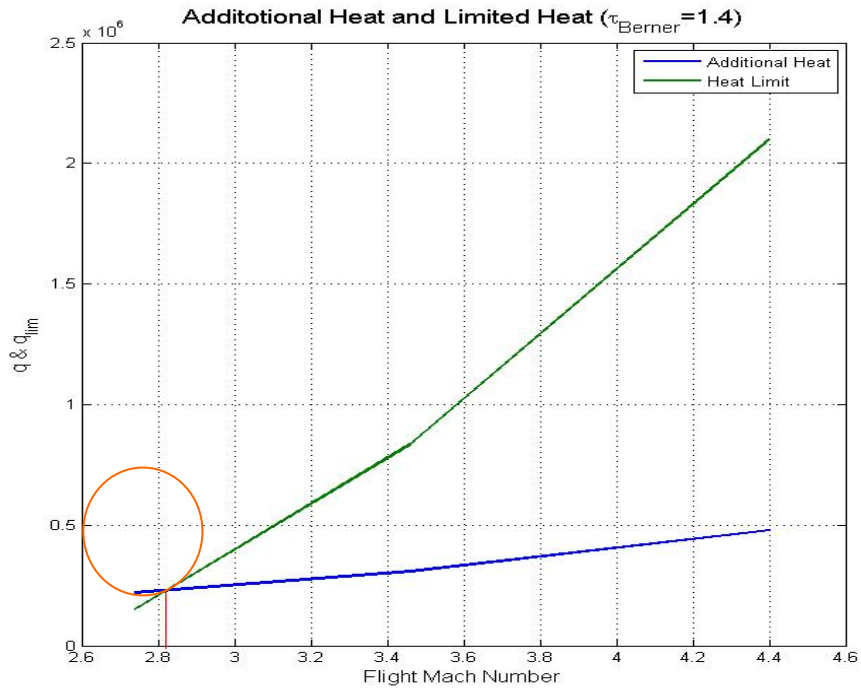

Figure 36: Heat Addition and Heat Limit (τ_{Burner}=1.40)

In this research τ_{burner} is taken as a constant parameter. Another constraint to stay within is $\tau_{Burner} \leq 1.5$. An interesting observation is that the choking limitations are less severe for the constant pressure burner than for the constant area burner. See Appendix C for details. Inside the burne there are two mixing methods, mixing with normal fuel injection and axial vortex mixing. In 1968, Swithenbank and Chigier suggested that "Substantial increase in mixing rates can be obtained by applying a

swirling motion to fuel jet." Researchers use empirical measures of mixing effectiveness. The interaction between the mixing efficiency and the overall efficiency must be investigated separately.

4.5. Expansion Nozzle and Specific Thrust

A 2-D flow analysis using the Method Characteristics is used for the expansion nozzle and specific thrust. Ideal, underexpanded, and overexpanded nozzles are all investigated. The control volume is carefully selected to facilitate the calculation of the total force or gross thrust. The expansion process starts inside the burner. The burner exit Mach number plays an important role in the overall performance of the propulsion system. The burner exit Mach number increases with altitude (see Figure 37) and it means the generated specific thrust is increased, see equations (4-41), and (4-42).

The exit temperature and the exit area ratio are calculated as follows:

$$T_{10} = T_4\left(\frac{P_0}{P_4}\right)^{\frac{R}{C_{Pe}}} \overset{\text{Const. Pressure Burner}}{=} T_4\left(\frac{P_0}{P_3}\right)^{\frac{R}{C_{Pe}}} \tag{4-44}$$

$$\frac{A_{10}}{A_0} = (1+f)\cdot\frac{P_0}{P_{10}}\cdot\frac{T_{10}}{T_0}\cdot\frac{V_0}{V_{10}} \tag{4-45}$$

Both a MATLAB program (***expansion.m***) and a MathCAD program (***expansion. derv1***) are used for these computations.

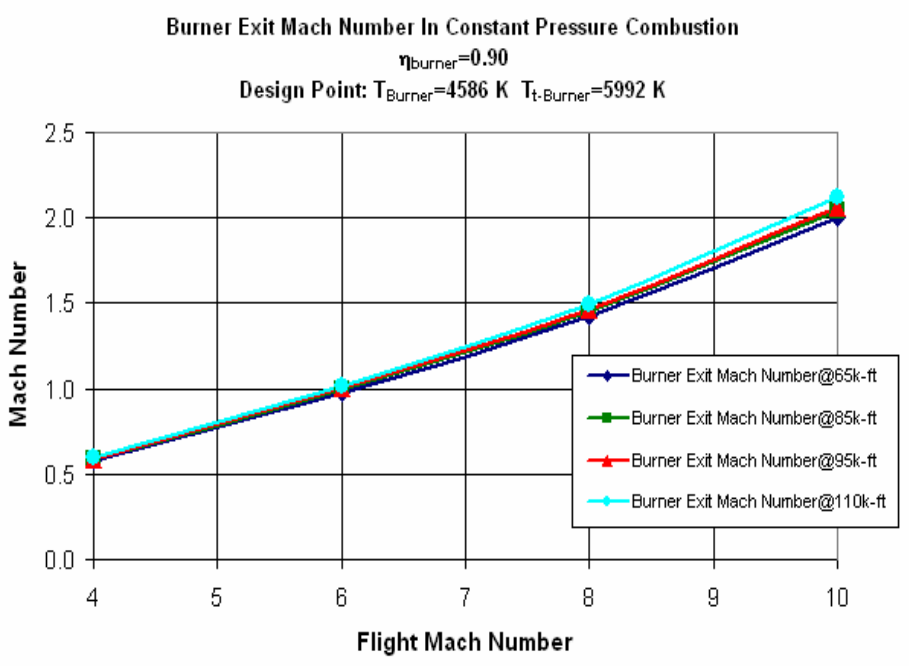

Figure 37: Burner Exit Mach Number

As the exit Mach number increases, the height ratio of the nozzle increases along with the flow turning angle. Unlike subsonic exhaust nozzles, the exhaust nozzles used in hypersonic vehicles are 2-D or planer rather than circular or axisymmetric. The nozzles used in hypersonic vehicles are relatively heavy. Changing their geometry is not easy. In most engines used in hypersonic vehicles the flow enters the nozzle supersonically. This makes their analysis much easier. The nozzle is designed based on the isentropic flow assumption (ideal expansion). The effect of underexpansion is discussed in the following section. The Method of Characteristics utilizes a graphical approach to construct the contour of a supersonic nozzle. This method is a classical technique for the solution of inviscid both internal and external supersonic and hypersonic flows.

The flow in the expansion nozzle has the following characteristics:

$$\mu_4 = \arcsin\frac{1}{M_{BE}} \tag{4-46}$$

Total flow turning from M_{BE} to M_Y is simulated by:

$$\omega = \sqrt{\frac{\gamma_{Burner}+1}{\gamma_{Burner}-1}}\left\{\arctan\sqrt{\frac{\gamma_{Burner}-1}{\gamma_{Burner}+1}\left(M^2{}_Y-1\right)}-\arctan\sqrt{\frac{\gamma_{Burner}-1}{\gamma_{Burner}+1}\left(M^2{}_4-1\right)}\right\} \quad ...$$

$$-\left\{\arctan\sqrt{\left(M^2{}_Y-1\right)}-\arctan\sqrt{\left(M^2{}_4-1\right)}\right\} \tag{4-47}$$

The Mach number (M_{III}) requires in the uniform flow zone of the nozzle. The uniform flow zone Mach number is found using the solution to equation (4-48) [18].

$$\frac{\omega}{2} = \sqrt{\frac{\gamma_{Burner}+1}{\gamma_{Burner}-1}}\left\{\arctan\sqrt{\frac{\gamma_{Burner}-1}{\gamma_{Burner}+1}\left(M^2{}_{III}-1\right)}-\arctan\sqrt{\frac{\gamma_{Burner}-1}{\gamma_{Burner}+1}\left(M^2{}_4-1\right)}\right\} \quad ...$$

$$-\left\{\arctan\sqrt{\left(M^2{}_{III}-1\right)}-\arctan\sqrt{\left(M^2{}_4-1\right)}\right\} \tag{4-48}$$

Using $M_{III,}$ the Mach wave angle is:

$$\mu_{III} = \arcsin\frac{1}{M_{III}} \tag{4-49}$$

The static pressure in the uniform flow zone of the nozzle is calculated by:

$$\frac{P_{III}}{P_{BE}} = \left\{\frac{1+\frac{\gamma_{Burner}-1}{2}M_4^2}{1+\frac{\gamma_{Burner}-1}{2}M_{III}^2}\right\}^{\frac{\gamma_{Burner}}{\gamma_{Burner}-1}} \tag{4-50}$$

The Mach wave angle in the nozzle's exit is written as:

$$\mu_{10} = \arcsin\frac{1}{M_Y} \tag{4-51}$$

The ratio of the exit height to entry height for ideal design point expansion components is:

$$\frac{H_{10}}{H_4}=\left(\frac{M_4}{M_Y}\right)\left\{\frac{1+\frac{\gamma_{Burner}-1}{2}M_Y^2}{1+\frac{\gamma_{Burner}-1}{2}M_4^2}\right\}^{\frac{\gamma_{Burner}+1}{2(\gamma_{Burner}-1)}} \tag{4-52}$$

The ratio of the exit height to the entry height for ideal design point expansion components increases rapidly with nozzle exit Mach number. The expansion system must provide a sizable $\frac{H_{10}}{H_4}$ using variable geometry as it is shown in Figure 38. The flow turning angle is shown in Figure 39. The flow turning varies with the burner Mach number, the burner ratio of specific heats, and the exit Mach number. These results suggest that a variable geometry is required as the properties of high Mach number flow are very sensitive to amount of ω (the flow turning from M_4 to M_{10}). If the value of $\left(\frac{P_4}{P_0}\right)$ is less than the value required by the design $\frac{H_{10}}{H_4}$ then the flow is calls overexpanded. If the value of $\left(\frac{P_4}{P_0}\right)$ is greater than the value required by the design $\frac{H_{10}}{H_4}$ then the flow is conditions calls underexpanded.

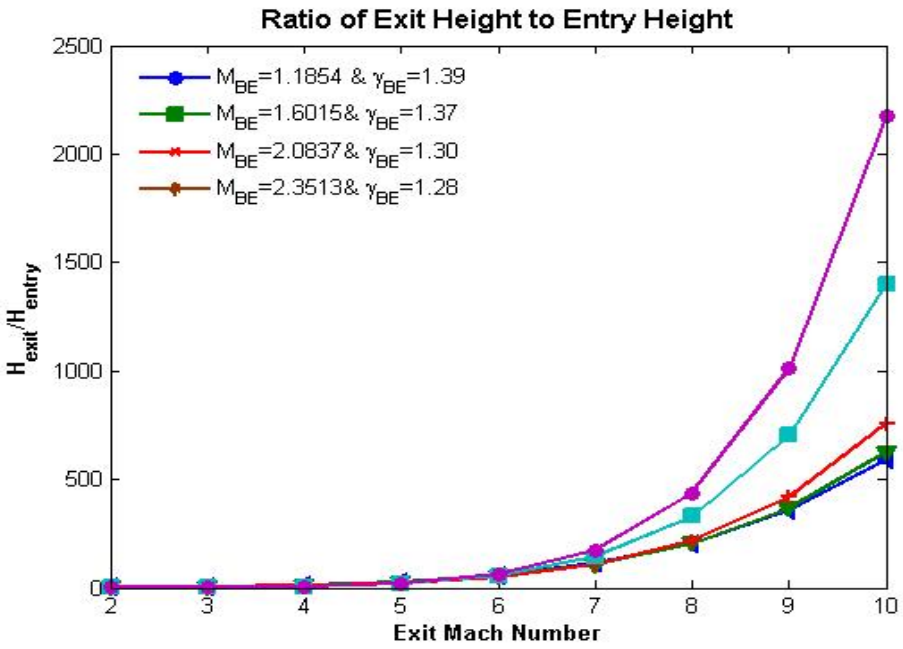

Figure 38: Ratio of Nozzle Exit Height to Entry Height

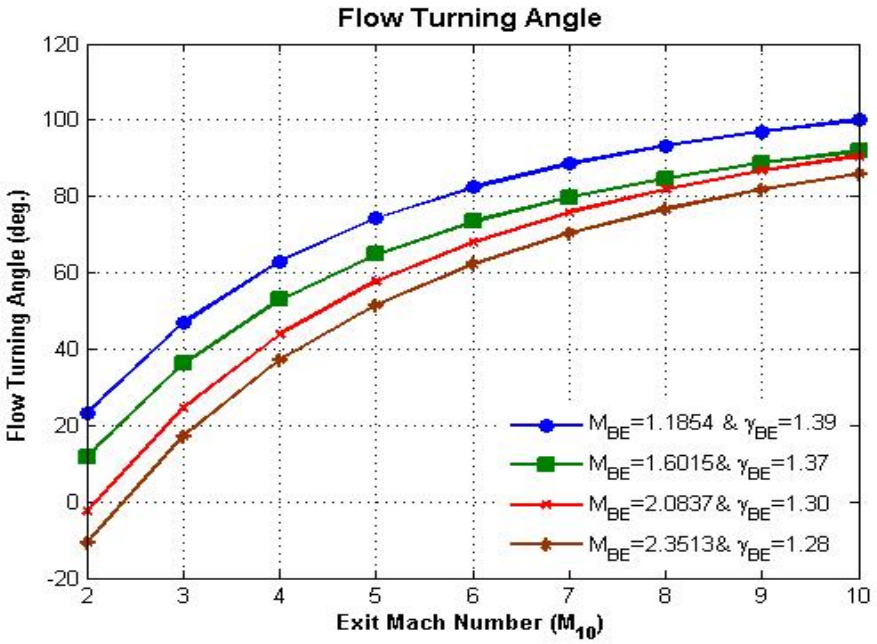

Figure 39: Flow Turning Angle (ω)

The exit plane components are used to calculate the uninstalled engine thrust as:

$$F = \dot{m}_{10} V_{10} - \dot{m}_0 V_0 + (P_{10} - P_0) A_{10} \qquad (4\text{-}53\text{-a})$$

$$F = \left(\dot{m}_{10} V_{10} + P_{10} A_{10}\right) - \left(\dot{m}_0 V_0 + P_0 A_0\right) - P_0 \left(A_{10} - A_0\right) \quad \text{(4-53-b)}$$

where,

$$V_{10} = \sqrt{V_4^2 + 2C_{p-Burner}\left(T_{10} - T_4\right)} \quad \text{(4-54)}$$

Also, the definition of the stream function for both the freestream flow and the exit flow,

$$Sa_{10} = V_{10}\left(1 + \frac{RT_{10}}{V^2_{10}}\right) \quad \text{(4-55)}$$

$$Sa_0 = V_0\left(1 + \frac{RT_0}{V^2_0}\right) \quad \text{(4-56)}$$

Finally from the conversation of mass,

$$\frac{A_{10}}{A_0} = \left(1 + f\right) \cdot \frac{P_0}{P_{10}} \cdot \frac{T_{10}}{T_0} \cdot \frac{V_0}{V_{10}} \quad \text{(4-57)}$$

The specific thrust is written as:

$$\frac{F}{\dot{m}_0} = \left(1 + f\right) \cdot Sa_{10} - Sa_0 - \frac{RT_0}{V_0}\left(\frac{A_{10}}{A_0} - 1\right) \quad \text{(4-58)}$$

4.6. Case Study

The nozzle performance and the overall engine performance are next investigated for multiple Mach numbers. The results are used to find the specific thrust of the engine. The equations of motion are used to find the required thrust force. Knowing the required thrust force for steady state flight yields the required air mass flow rate and the fuel mass flow rate. The stream function for both the freestream flow and the exit flow are calculated and the results are summarized in Figures 40 through 48. The burner design point is a design parameter and can be adjusted according to the design

criteria. The computer programs are designed to make these adjustments easy. At hypersonic speeds, the free stream thrust function increases with a faster slop than the exit thrust function. Because of this, regardless of the burner design point the specific thrust decreases when the flight Mach number increases.

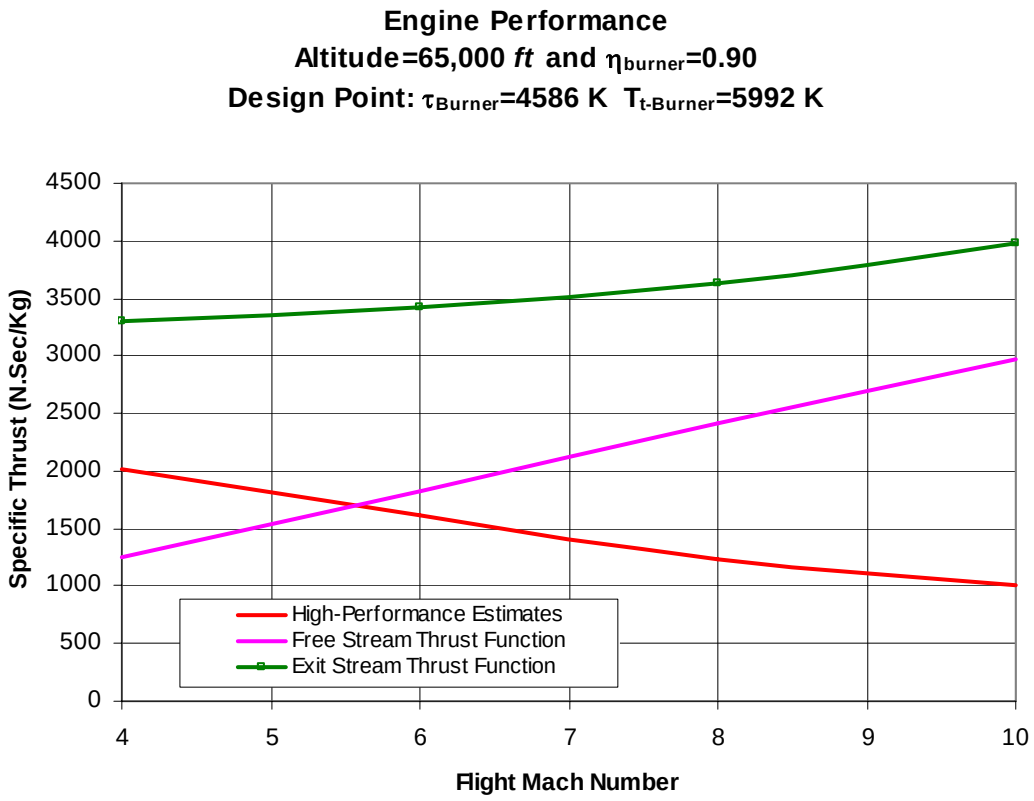

Figure 40: Specific Thrust @ 65,000 ft*

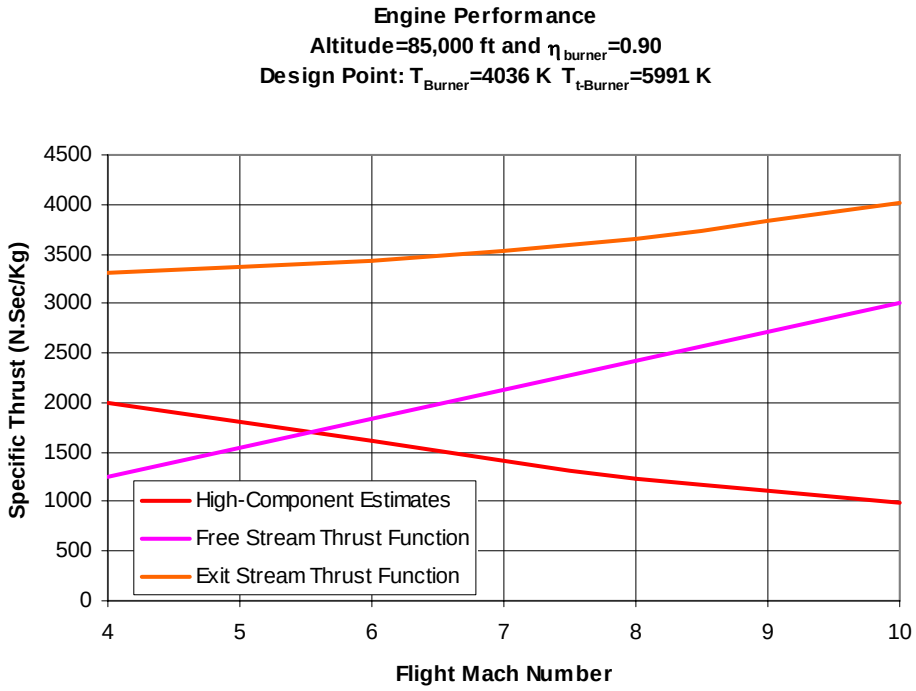

Figure 41: Specific Thrust @ 85,000 ft*

**High efficiency estimate*

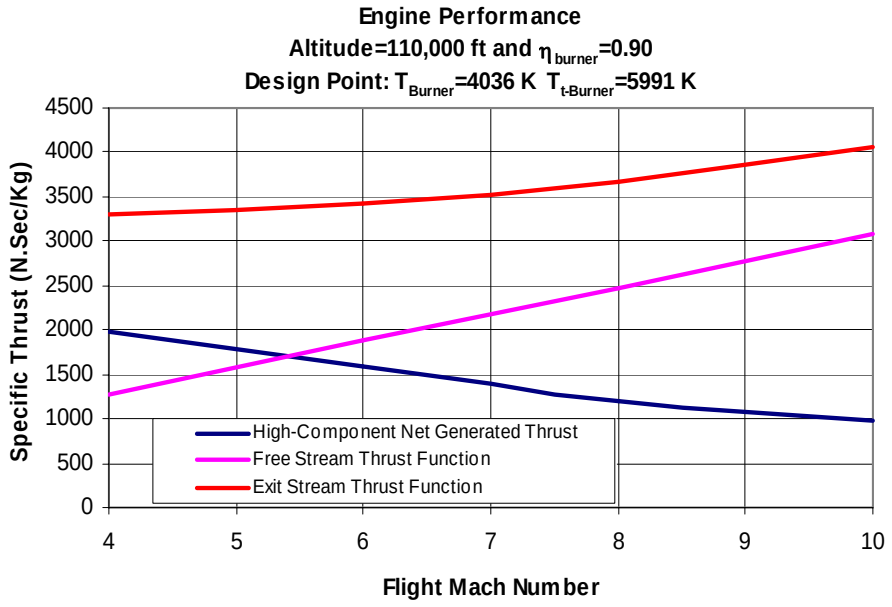

Figure 42: Specific Thrust @ 110,000 ft*

**High efficiency estimate*

The results are summarized in Figure 43. The specific thrust decreases with the increase in the flight Mach number.

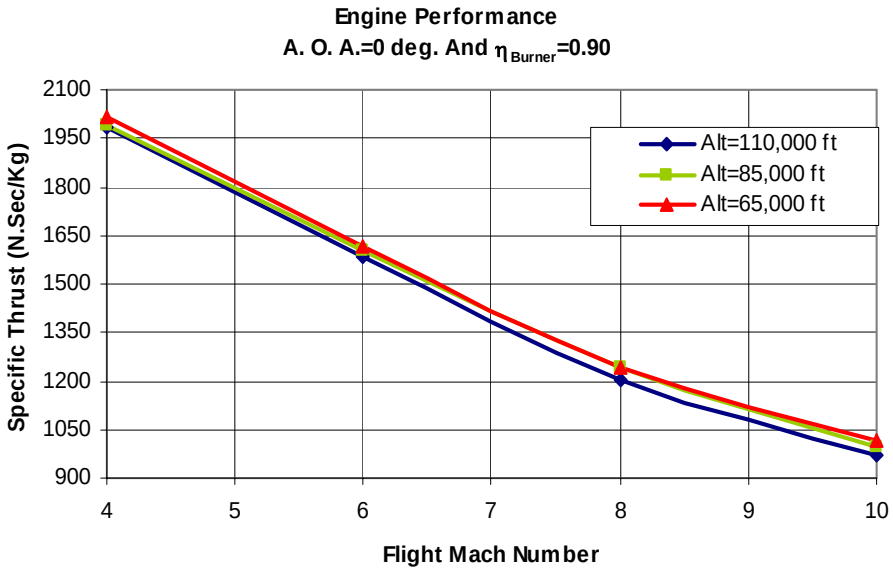

Figure 43: Engine Performance (Specific Thrust) at Different Altitudes*

**High efficiency estimate*

If the high estimates are achieved the performance of ramjet/scramjet propulsion engine becomes almost irresistible.

The specific impulse as a function of flight Mach number is shown in Figure 44.

The results of multiple iterations using MATLAB and MathCAD programs (Analysis.m) show that the engine with low burner temperature ratios can not generate positive thrust at high flight Mach number. In some cases, even changing the nozzle expansion ratio does not help. This fact shows how complicated the nature of the hypersonic propulsion is. The following figure shows the result of specific design points that positive thrust is generated. The specific impulse becomes very small for

high Mach numbers, and flight can not be sustained for long time. This is done using the assumption of a variable inlet and exit areas. The assumption of variable exit area is a big assumption considering the nature of the hypersonic flows.

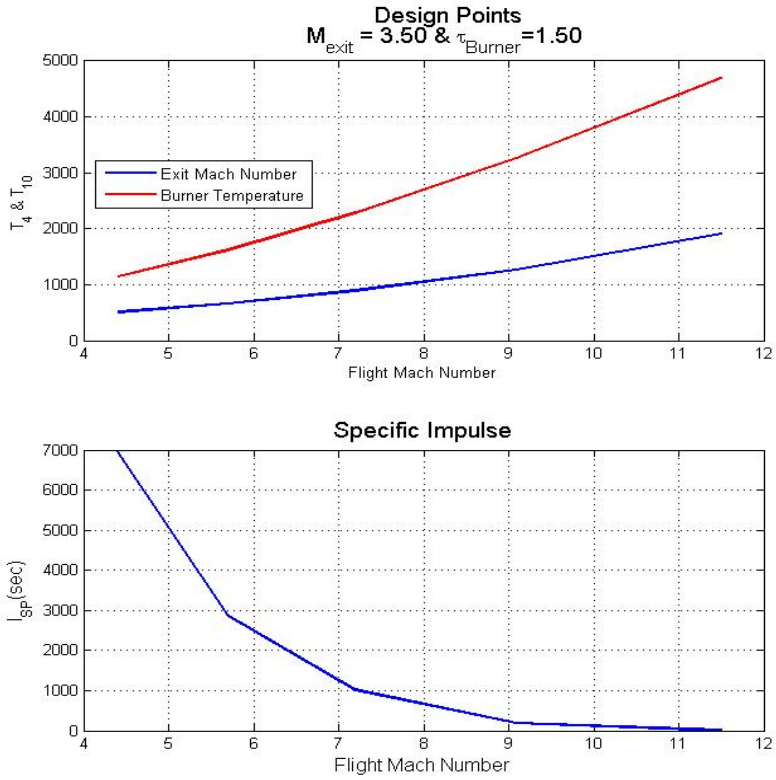

Figure 44: Specific Impulse and Exit Temperature

In order to achieve a higher specific impulse at a high flight Mach number, the expansion ratio in the nozzle must be increased.

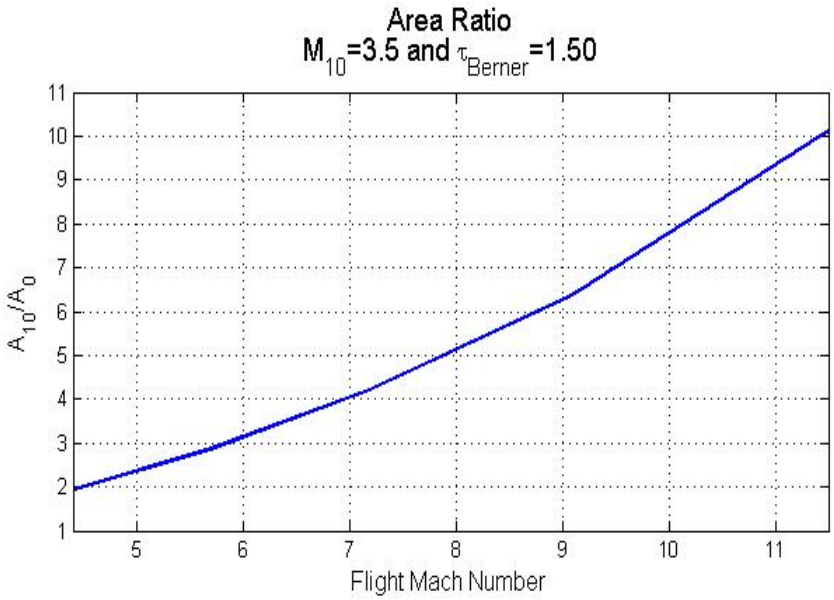

Figure 45: Area Ratio

A comparison of this engine model with the NASA Hypersonic Research Engine (HRE) model and the German Hypersonic Technology model validates the decreasing trend of I_{sp} with flight Mach number in the range of Mach 4 to Mach 8.

In Chapter 5, the same engine model is used in the trajectory optimization process. As discussed before, the required thrust force is calculated for the steady state flight condition. Knowing the required thrust force for steady state flight and the specific thrust allows the required air mass flow rate and the fuel mass flow rate to be computed. The fuel mass flow rate is included in regenerative cooling calculations in the next section. The derivation of this equation is provided in Chapter5

The steady state flight the minimum required thrust force is:

$$\text{Thrust}_{\min} = 1033 \cdot \text{M}^2 - 1.353 \times 10^4 \cdot \text{M} + 1.524 \times 10^5 \qquad (4\text{-}59)$$

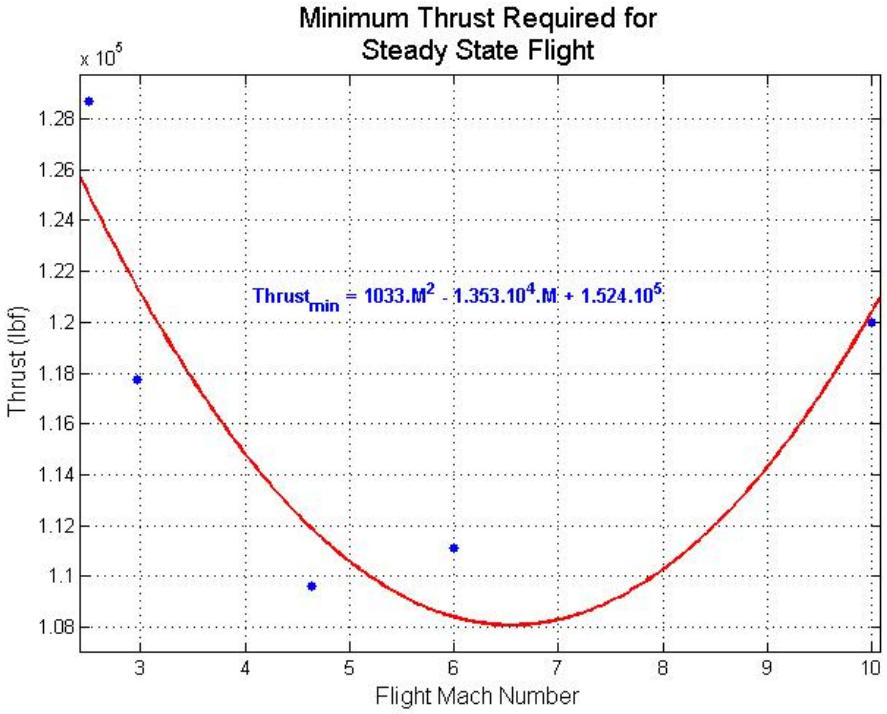

Figure 46: Minimum Required Thrust Force

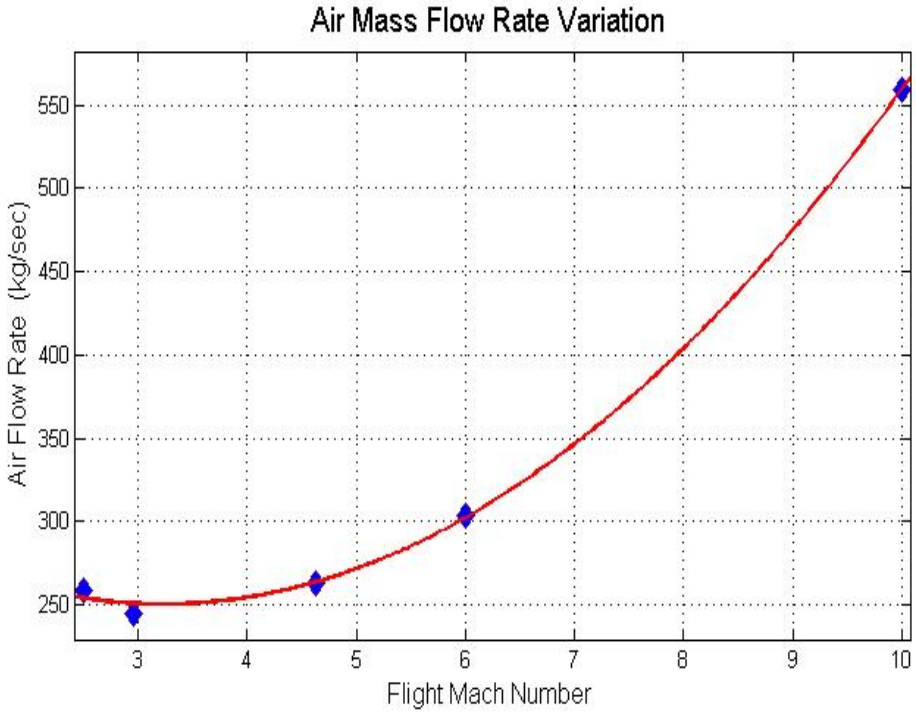

Figure 47: Air Mass Flow Rate

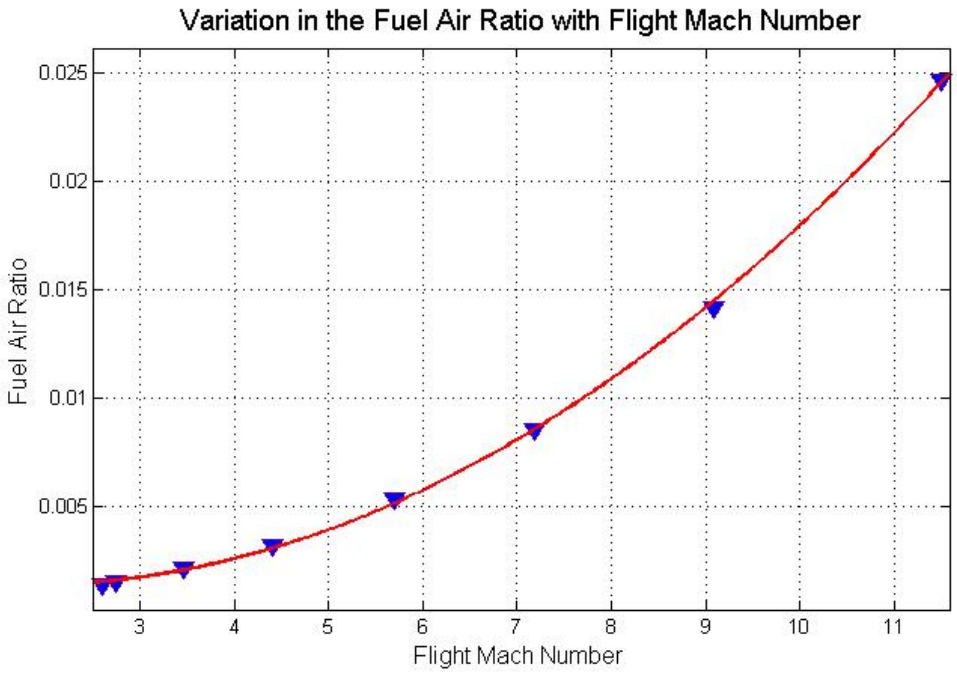

Figure 48: Fuel Air Ratio

4.7. Cooling the Ramjet/Scramjet

The combustion process in ramjet/scramjet engines takes place in a very high temperature environment. To control the body temperature of the vehicle within an acceptable range, the ramjet/scramjet engine must be cooled. It is clear that a proper material selection is a key to successful engine design. One of the ways to control excessive heat is to radiate part of it into the surrounding environment. Most of the time, the engine must also be cooled internally plus radiation emitted to the environment. The process of heat absorption by the fuel as it is consumed is called regenerative cooling. This method has been used as an effective way to cool engines internally. The analytical methods in the previous sections can be employed to find the proper air fuel ratio for any flight Mach number. The flight fuel air ratio is used to find the fuel mass flux. The heat flux is proportional to the mass flux. Quasi-one-

dimensional theory is used for the heat transfer analysis. To analyze the heat transfer in the axial direction, 2 or 3 dimensional finite element models would be needed. In this research, it is assumed that the thermal conductivity and the film coefficients are at their average values and are not functions the pressure or temperature. The 3-D model of the isolator and burner is shown in Figure 28, and the 2-D model is shown in the Figure 49. The wall channels are assumed to be cooled by the fuel through a combination of convective and film cooling. After convectively cooling the wall, the fuel is injected into a slot parallel to the core flow. This helps to preheat the fuel before combustion and increase the combustion efficiency while at the same time cooling the wall [19], [23].

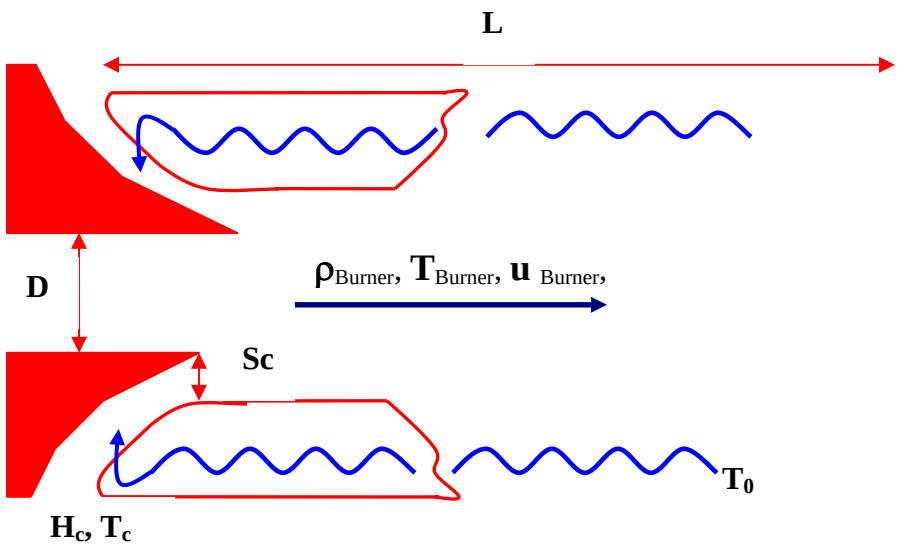

Figure 49: Engine Cooling System

$$\dot{m}_{cs} = 4D\rho_c u_c S_c \qquad (4\text{-}60)$$

$$\dot{m}_0 = D^2 \rho_{Burner} u_{Burner} \qquad (4\text{-}61)$$

The equivalence ratio for cooling is

$$\phi_{cs} = \frac{\dot{m}_{cs}}{\dot{m}_0 . f} = \left(\frac{1}{f}\right)\left(\frac{Sc}{D}\right)\left(\frac{\rho_c u_c}{\rho_{Burner} u_{Burner}}\right) \tag{4-62}$$

The gas and the liquid film coefficients are calculated using the following conventional heat transfer theory.

$$h_g = 0.026 \cdot \left(\frac{\kappa}{D}\right) \cdot \left(\frac{D \cdot V \cdot \rho}{\mu}\right)^{0.8} \cdot \left(\frac{\mu \cdot Cp}{\kappa}\right)^{0.4} \tag{4-63}$$

The gas film coefficient also can be found using

$$h_g = 0.026 \cdot \left(\frac{\kappa}{D^{0.2}}\right) \cdot \left(\frac{V \cdot \rho}{1}\right)^{0.8} \cdot \frac{Pr^{0.4}}{\mu^{0.8}} \tag{4-64}$$

where D is the diameter of the chamber of the nozzle, V is the calculated average local gas velocity, κ the conductivity of the gas, μ is the absolute gas viscosity, Cp is the specific heat of the gas at constant pressure burner, and ρ is the gas density.

The liquid film coefficient is:

$$h_l = 0.023 \cdot \gamma_{ave} \cdot \left(\frac{\dot{m}_c}{A_c}\right) \cdot \left(\frac{D_{Hy-c} \cdot V_c \cdot \rho_c}{\mu_c}\right)^{-0.2} \cdot \left(\frac{\mu_c \cdot \gamma_{ave}}{\kappa_c}\right)^{\frac{-2}{3}} \tag{4-65}$$

where $\dot{m}_c$ is the fluid mass flow rate (check Chapter 5 for details), A is the cross sectional area, D is the equivalent diameter of the coolant passage cross section, κ is the conductivity of the liquid, and μ is the absolute liquid viscosity.

For the case where: M=8, $D_{Combustor}$= 1 m, $(\rho V)_{gas} = 73.20 \ \frac{kg}{m^2 \cdot sec}$, $\kappa = 0.328 \ \frac{W}{m^2 K}$, $Pr = 0.7$, $C_p = 18 \ \frac{J}{Kg \cdot K}$, $\mu_c = 1.81 \times 10^{-4} \ \frac{kg}{m \cdot sec}$, $\dot{m}_{fuel} = 4.8717 \ \frac{kg}{sec}$ (for details

see Chapter 5), $D_{HY\text{-}c} = 0.11\times10^{-2}$ m, $\kappa_c = 0.172\ \frac{W}{m^2K}$, the number of channels are calculated to be 784. Also, $\mu_c = 0.11\times10^{-2}\ \frac{kg}{m\cdot sec}$ (absolute gas viscosity), $T_{l\text{-}ave}$ = 300 K, and T_g = 2280 K. The value of h_g is calculated using equations (4-45) and (4-46). It varies within the range [188~219 $\frac{W}{m^2K}$] as a function of temperature. Also, the liquid film coefficient is calculated to be $h_l = 113{,}162\frac{W}{m^2K}$ using equation (4-47).

Two MATLAB programs '***heatransfer2.m***' and '***heatransfer3.m***' were written to do all heat transfer calculations. The program '***heatransfer2.m***' calculates the overall film coefficient, the wall temperature liquid side, and the gas side. In the case that the total heat absorbed by the liquid is known, the program ***heatransfer3.m*** calculates the wall temperature liquid side, and also the gas side.

Quasi-one-dimensional heat transfer theory plus the fundamentals of heat flux yield the total heat flux to the combustor wall as [19]:

$$\dot{q}_{wall} = \underbrace{h_c\left(T_{w-c} - T_c\right)}_{\text{Coolant}} = \underbrace{\varepsilon_g\sigma T_g^{\,4} + h_g\left(T_{t4} - T_{w-g}\right)}_{\text{Combustor}} = \underbrace{\kappa_w\left(\frac{\left(T_{w-g} - T_{w-c}\right)}{t_{w-t}}\right)}_{\text{Wall}} \qquad (4\text{-}66)$$

The net one-dimensional heat flux to the combustor is the sum of the convective and radiative heat transfer. The quantity ε_g is known as the emissivity of the gas. The quantity σ is known as the Stefan-Boltzmann constant, which is $5.67\times10^{-8}\ \frac{W}{m^2K^4}$.

$$\dot{q}_{wall} = \frac{h_g\left(T_{t4} - T_c\right) + \left(\frac{\varepsilon\sigma T_g^{\,2}}{h_g}\right)}{h_{overall}} \qquad (4\text{-}67)$$

$$h_{overall} = \frac{1}{h_g} + \frac{1}{h_c} + \frac{t_w}{\kappa_w} \qquad (4\text{-}68)$$

In equation (4-68), t_w is the combustor wall thickness and κ_w is the wall thermal conductivity.

For the case $t_w = 2.5$ cm and $\kappa_w = 43 \; {}^{W}\!/_{m^2} - {}^{K}\!/_{m}$ the following results are calculated:

$h_{overall} = 1.7888 \times 10^2 \; \frac{W}{m^2 K}$, $q = 0.37208 \; \frac{MW}{m^2}$, $T_{w\text{-}c} = 203.29 \; K$, and $T_{w\text{-}g} = 419.61 \; K$.

The discussed MATLAB programs are designed to be flexible, and the user can check for variations in each output due to any changes in the gas and the liquid film coefficients.

4.8. Summary

This section covered the development of a cycle analysis for a ramjet/scramjet engine consisting of an airbreathing core with a variable geometry inlet. This analysis includes underbody compression, the isolator-burner, and the expansion nozzle. This modeling process is used within a hypersonic vehicle conceptual design framework. The engine underbody geometry and the efficiency parameters can be adjusted for new vehicle concepts. The model and simulation are developed to support conceptual design studies of hypersonic vehicles using multiple cycle engines.

Chapter 5: Trajectory Optimization

5.0. Introduction

This chapter covers the trajectory optimization for a generic hypersonic vehicle (GHV). Advanced guidance and control systems are key components to establishing a successful launch operation. In order to reduce the cost of designing flight profiles and to improve the vehicle performance, optimal trajectory calculations are required. The best way to perform an optimal trajectory is to update the trajectory on-board using real-time software. In this research, optimization techniques are applied only to the supersonic-hypersonic portion of the flight trajectory [$2.148 < M_0 < 15.01$] and it is limited to altitude between 60,000 to 100,424 ft.

5.1. Formulation and Analysis Process

Given a functional form for *F* and choosing the *n* parameters q_1, q_2, q_3,…, q_n to be arbitrary functions of time (*t*), what forms must these functions of *t* take in order to render *F* a maximum or a minimum? The generalized form of *J* is represented as [24]:

$$J = \int_{t_o}^{t_f} F\left(q_1, q_2, \ldots, q_n; \dot{q}_1, \dot{q}_2, \ldots, \dot{q}_n; t\right) dt \qquad (5\text{-}1)$$

The q's are independent of each other. Each q is a dependent variable and is a function of time (*t*).

A continuous dynamic system is described by a vector of three states ($\aleph(t)$) at time *t*. The state rate of change is shown as:

$$\dot{\aleph} = f(\aleph, u, t) \qquad (5\text{-}2)$$

where u(t) is the control vector.

In this study, the main objective of the optimization process is to find the optimum trajectory using the flight velocity as the state variable and the flight path angle as the control variable. The goal is to maximize the flight range within $t_0 < t < t_f$.

The continuous dynamic system is presented as:

$$\begin{aligned} \dot{V} &= \frac{1}{m}\left(T - q \cdot S \cdot C_D - m \cdot g \cdot \sin\gamma\right) \\ \dot{x} &= V \cdot \cos\gamma \\ \dot{y} &= V \cdot \sin\gamma \end{aligned} \tag{5-3}$$

Here, "V" represents the flight velocity, "x" represents the range, the altitude is represented by "y", and "γ" is the flight path angle.

The state vector $\aleph$ is defined as: $\aleph = \begin{bmatrix} V \\ x \\ y \end{bmatrix}$

The control vector is defined as: $u = [\gamma]$

The adjoint of the performance index is represented by equation (5-4),

$$\bar{J} = \phi\left[\aleph\left(t_f\right)\right] + \int_{t_0}^{t_f} \left\{L\left(\aleph(t), u(t), t\right)\right\} dt \tag{5-4}$$

From equation (5-2)

$$f(\aleph, u, t) - \dot{\aleph} = 0 \tag{5-5}$$

Adding the constraints using equation (5-5), and using a time-varying Lagrange multiplier $\lambda(t)$, the new version of the performance index yields [25]:

$$\bar{J} = \phi\left[\aleph\left(t_f\right)\right] + \int_{t_0}^{t_f} \left\{L\left(\aleph(t), u(t), t\right) + \lambda(t) \cdot \left[f\left(\aleph(t), u(t), t\right) - \dot{\aleph}\right]\right\} dt$$

As was stated before, the goal of the optimization process is to maximize the range of flight, so the performance index is defined as the flight range.

$$J = \phi\left[\aleph\left(t_f\right)\right] + \int_{t_0}^{t_f} L\left(\aleph, u, t\right)dt = x \qquad \text{(range)} \tag{5-6}$$

Assume that $t_0 = 0$,

$$J = \phi\left[\aleph\left(t_f\right)\right] + \int_{t_0}^{t_f} L\left(\aleph, u, t\right)dt = x = \int_{0}^{tf} \dot{x} \cdot dt \tag{5-7}$$

where from the equations of motion $\dot{x} = V \cdot \cos\gamma$ (5-3). The performance index becomes [25], [26], [27]:

$$J = \int_{0}^{tf} \dot{x} \cdot dt \Rightarrow \quad J = \int_{0}^{tf} V \cdot \cos\gamma \cdot dt \tag{5-8}$$

Comparison of equation (5-8) with the original performance index (5-6) reveals:

$$\phi\left[\aleph\left(t_f\right)\right] = 0 \tag{5-9}$$

$$L\left(\aleph, u, t\right) = V \cdot \cos\gamma \Rightarrow X \triangleq V \;\&\; u \triangleq \gamma \tag{5-10}$$

The time varying functional form of *F*, a fundamental equation, is given as:

$$F = V \cdot \cos\gamma + \lambda_V\left(m\dot{V} - T + q \cdot S \cdot C_D + m \cdot g \cdot \sin\gamma\right) \tag{5-11}$$

Now applying the Euler-Lagrange equation gives:

$$\frac{\partial}{\partial t}\left(\frac{\partial F}{\partial \dot{V}}\right) - \frac{\partial F}{\partial V} = 0 \Rightarrow \frac{\partial}{\partial t}\left(\lambda_V\right) - \frac{\partial F}{\partial y} = 0 \Rightarrow \dot{\lambda}_V = \frac{\partial F}{\partial V} \tag{5-12}$$

$$\frac{\partial F}{\partial \gamma} = 0 \tag{5-13}$$

5.2. Trajectory Constraints

According to modified Newtonian Impact Theory, the local pressures are proportional to the dynamic pressure as follows:

$$P - P_0 = q_0 \cdot C_{pr} . \sin^2\theta \qquad (5\text{-}14)$$

In the previous equation, C_{pr} is the pressure coefficient and θ is the angle of inclination of the surface with respect to the freestream. If the dynamic pressure (q_0) is too high then the structural force and the drag force on the vehicle can be very large. This will result in a higher empty weight (W_0) and will require a more powerful engine. On the other hand, if the dynamic pressure is too small, then a very large wing reference area is needed to sustain flight. Because of these concerns, most hypersonic vehicles operate within a very narrow range of dynamic pressure [500 to 2000 psf]. The following tables show how the velocity, air physical characteristics, and the air mass flow rate per unit area change at constant dynamic pressures through the trajectory [18]. The maximum and the minimum flight Mach number in the range of dynamic pressure [500 to 2000 psf] are calculated [$11.2 < M < 0.5$]. It means at 100,000 ft altitude, the flight Mach number can not exceed M=11.2 unless design constraints change.

Table 3: Constant Dynamic Pressure (2000 psf)

q_0 (psf)	Mach	Altitude (ft)	ρ_0 (slug/ft^3)	T_0 (R°)	P_0 (lb/sqft)	a_0 (ft/sec)	V_0(ft/sec)	$\rho_0 V_0$ (slug/ft^2.sec)
2000	1.16	0	0.0024	518.67	2116.23	1116.27	1297.04	3.11
2000	1.4	10000	0.0018	483.01	1455.34	1077.21	1509.33	2.72
2000	1.71	20000	0.0013	447.35	972.5	1036.68	1776.91	2.31
2000	2.13	30000	0.0009	411.69	628.44	994.5	2120.51	1.91
2000	2.7	40000	0.0006	389.97	391.69	967.92	2614.18	1.57
2000	3.43	50000	0.0004	389.97	242.22	967.92	3324.33	1.33
2000	4.37	60000	0.000224	389.97	149.78	967.92	4227.39	0.95
2000	5.55	70000	0.000138	392.37	92.68	970.9	5390.57	0.74
2000	7.04	80000	0.000084	397.86	57.68	977.66	6881.14	0.58
2000	8.89	90000	0.000052	403.35	36.12	984.38	8754.55	0.46
2000	9.99	95000	0.000041	406.09	28.66	987.72	9862.53	0.41
2000	11.2	100000	0.000032	408.83	22.77	991.05	11101.81	0.36

Tables 3 though 5 demonstrate that flying at constant dynamic pressures causes a dramatic reduction in the air mass flow rate per unit area.

Table 4: Constant Dynamic Pressure (1000 psf)

q_0 (psf)	Mach	Altitude (ft)	ρ_0 (slug/ft^3)	T_0 (R°)	P_0 (lb/sqft)	a_0 (ft/sec)	V_0(ft/sec)	$\rho_0 V_0$ (slug/ft^2.sec)
1000	0.82	0	0.002400	518.67	2116.23	1116.27	917.14	2.20
1000	0.99	10000	0.001800	483.01	1455.34	1077.21	1067.26	1.92
1000	1.21	20000	0.001300	447.35	972.50	1036.68	1256.47	1.63
1000	1.51	30000	0.000900	411.69	628.44	994.50	1499.43	1.35
1000	1.91	40000	0.000600	389.97	391.69	967.92	1848.50	1.11
1000	2.43	50000	0.000400	389.97	242.22	967.92	2350.65	0.94
1000	3.09	60000	0.000224	389.97	149.78	967.92	2989.21	0.67
1000	3.93	70000	0.000138	392.37	92.68	970.90	3811.71	0.53
1000	4.98	80000	0.000084	397.86	57.68	977.66	4865.70	0.41
1000	6.29	90000	0.000052	403.35	36.12	984.38	6190.41	0.32
1000	7.06	95000	0.000041	406.09	28.66	987.72	6973.86	0.29
1000	7.92	100000	0.000032	408.83	22.77	991.05	7850.17	0.25

Table 5: Constant Dynamic Pressure (500 psf)

q_0 (psf)	Mach	Altitude (ft)	ρ_0 (slug/ft^3)	T_0 (R°)	P_0 (lb/sqft)	a_0 (ft/sec)	V_0(ft/sec)	$\rho_0 V_0$ (slug/ft^2.sec)
500	0.58	0	0.002400	518.67	2116.23	1116.27	648.52	1.56
500	0.70	10000	0.001800	483.01	1455.34	1077.21	754.66	1.36
500	0.86	20000	0.001300	447.35	972.50	1036.68	888.46	1.15
500	1.07	30000	0.000900	411.69	628.44	994.50	1060.25	0.95
500	1.35	40000	0.000600	389.97	391.69	967.92	1307.09	0.78
500	1.72	50000	0.000400	389.97	242.22	967.92	1662.16	0.66
500	2.18	60000	0.000224	389.97	149.78	967.92	2113.69	0.47
500	2.78	70000	0.000138	392.37	92.68	970.90	2695.29	0.37
500	3.52	80000	0.000084	397.86	57.68	977.66	3440.57	0.29
500	4.45	90000	0.000052	403.35	36.12	984.38	4377.28	0.23
500	4.99	95000	0.000041	406.09	28.66	987.72	4931.26	0.20
500	5.60	100000	0.000032	408.83	22.77	991.05	5550.91	0.18

Figure 50 shows the trajectory constraints imposed by the dynamic pressure. Constant mass flow rates per unit area are shown in Figure 51.

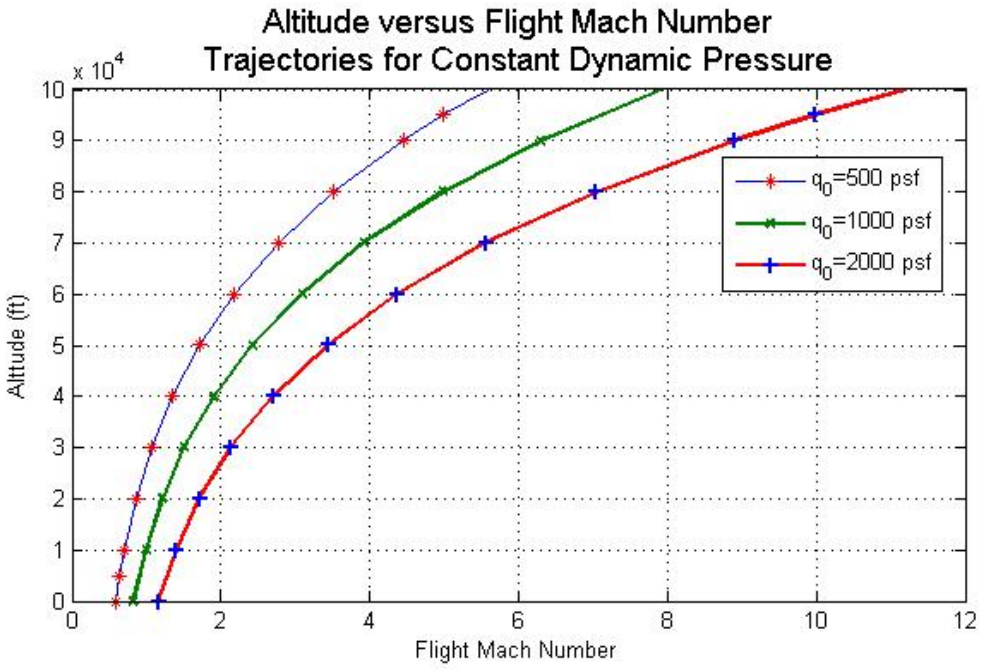

Figure 50: Trajectories for Constant Dynamic Pressure

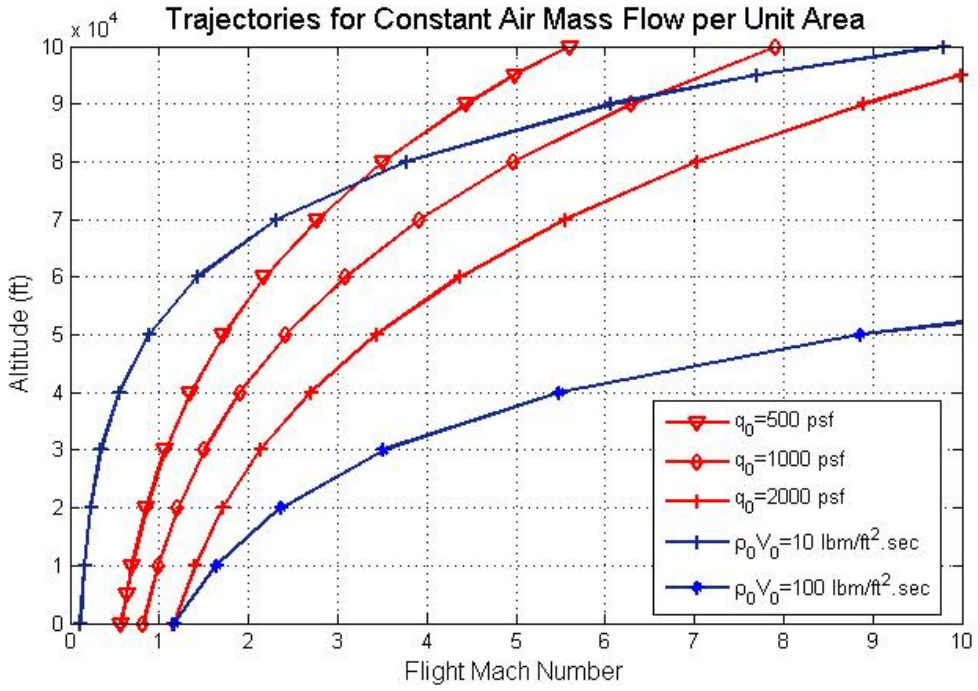

Figure 51: Constant Air Mass Flow Rate per Unit Area

As was shown, a high mass flow rate per unit area might be out of the dynamic pressure range, (see Figure 51, $\rho_0 V_0 = 100 \frac{\text{lbm}}{\text{ft}^2 \cdot \text{sec}}$).

The mass flow rate per unit area is equal to:

$$\rho_0 V_0 = \frac{q_0}{\frac{1}{2} V_0} = \frac{2q_0}{V_0} \tag{5-15}$$

where

$$V_0 = M_0 \cdot a_0$$

$$\rho_0 V_0 = \frac{2q_0}{a_0 M_0} \tag{5-16}$$

Another observation is that the mass flow is proportional to the inverse of the flight Mach number. To avoid a dramatic reduction in the air mass flow rate per unit area at higher flight Mach numbers, the dynamic pressure is increased constantly within the

allowable range. In the inlet engine design, a long forebody compression surface increases the capture area of the engine.

The optimization constraints are given as:

$$2000 \le q_0 \le 500 \text{ psf} \tag{5-17}$$

The minimum is:

$$\frac{1}{2}\rho \cdot V_0^2 \le 500 \text{ psf} \Rightarrow V_{0-\min} = \sqrt{\frac{1000}{\rho}}$$

The maximum is:

$$\frac{1}{2}\rho \cdot V_0^2 \le 2000 \text{ psf} \Rightarrow V_{0-\max} = \sqrt{\frac{4000}{\rho}} \tag{5-18}$$

Using the golden section search optimization technique, the extremum (minimum or maximum) mass flow rate per unit area is calculated for this specific case. There are two nonlinear inequality constraints for the dynamic pressure, equations (5-17) and (5-18). The maximum flight altitude is assumed at 100,000 ft, which provides one linear inequality constraint on the air density ($\rho > 0.000032$ slug/ft^3).

A MATLAB program, ***dpoptimization.m***, was written to apply the golden section search technique. The result of the optimization routine demonstrates that for the dynamic pressure range between [500 to 2000 psf], the maximum value for the mass flow rate per unit area cannot exceed $12.3841 \frac{\text{lbm}}{\text{ft}^2 \text{ sec}}$. In this research, the maximum value for the mass flow rate per unit area is taken to be $\rho V_0 = 15 \frac{\text{lbm}}{\text{ft}^2 \text{ sec}}$. Table 6 shows the minimum and the maximum flow rate per unit area, the minimum and the

maximum Mach number, and the minimum and the maximum flight velocity for a dynamic pressure range between [500 to 2000 psf].

Table 6: Minimum and Maximum Flow Rate per Unit Area

Altitude (ft)	T_0 (R°)	a_0 (ft/sec)	$V_{0\text{-min}}$ (ft/sec)	Mach $_{min}$	$\rho_0 V_{0\ min}$	$q_{0\ Min}$ (psf)
0	519	1116.27	648.65	0.581	49.6	500
10,000	483	1077.21	754.9	0.701	42.62	500
20,000	447	1036.68	888.46	0.857	36.21	500
30,000	412	994.5	1060.66	1.067	30.33	500
40,000	390	967.92	1307.52	1.351	24.61	500
50,000	390	967.92	1662.16	1.717	19.36	500
60,000	390	968.07	2113.02	2.183	15.23	500
70,000	392	971.05	2692.08	2.772	11.95	500
80,000	398	977.82	3450.54	3.529	9.32	500
90,000	403	984.54	4385.56	4.454	7.34	500
95,000	406	984.54	4938.96	5.017	6.51	500
100,000	409	991.21	5590.52	5.64	5.76	500
110,000	419	1003.62	7071.51	7.046	4.55	500

Altitude (ft)	T_0 (R°)	a_0 (ft/sec)	$V_{0\text{-max}}$ (ft/sec)	Mach $_{max}$	$\rho_0 V_{0\ Max}$	$q_{0\ Max}$ (psf)
0	519	1116.27	1297.31	1.16	99.2	2000
10,000	483	1077.21	1509.8	1.4	85.24	2000
20,000	447	1036.68	1776.92	1.71	72.43	2000
30,000	412	994.5	2121.32	2.13	60.67	2000
40,000	390	967.92	2615.04	2.7	49.21	2000
50,000	390	967.92	3324.32	3.43	38.71	2000
60,000	390	968.07	4226.03	4.37	30.45	2000
70,000	392	971.05	5384.15	5.54	23.9	2000
80,000	398	977.82	6901.08	7.06	18.65	2000
90,000	403	984.54	8771.13	8.91	14.67	2000
95,000	406	984.54	9877.91	10.03	13.03	2000
100,000	409	991.21	11181.03	11.28	11.51	2000
110,000	419	1003.62	14143.01	14.09	9.1	2000

The flow rate per unit area needs to be adjusted accordingly for any other dynamic pressure range. Figure 52 shows altitude versus flight Mach number for a constant mass flow rate per unit area, $15\ \frac{\text{lbm}}{\text{ft}^2\,\text{sec}}$.

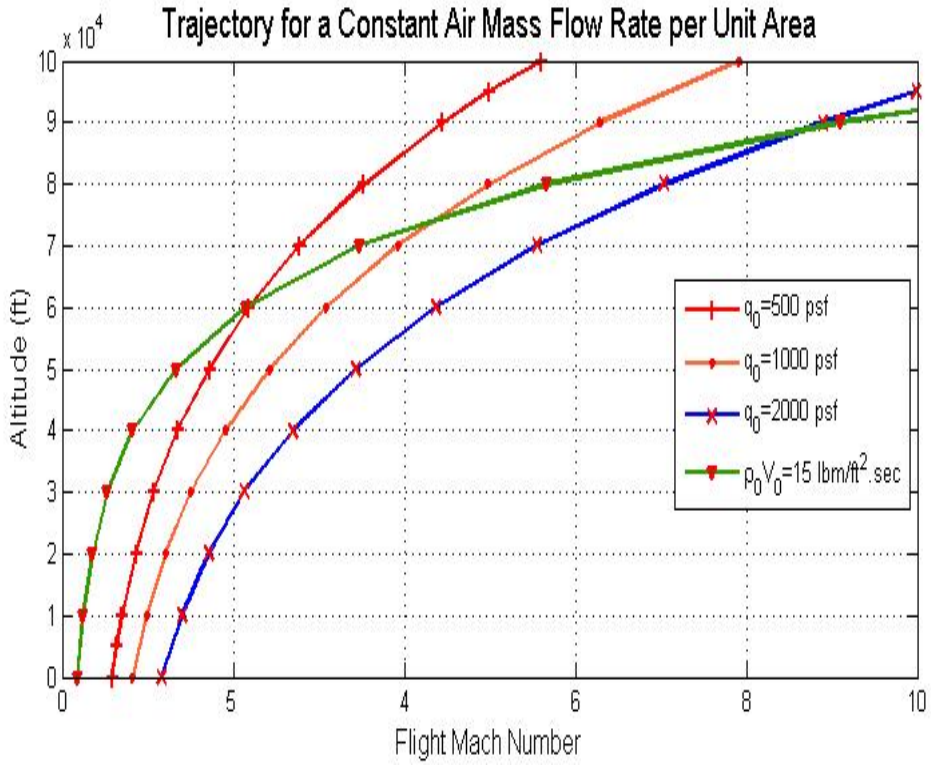

Figure 52: Trajectory for a Constant Air Mass Flow Rate per Unit Area

5.3. Modeling and Simulation

Dynamic Pressure

Considering that the dynamic pressure is a function of the velocity and the density of the air throughout the trajectory, its variation with flight altitude and flight velocity are developed using air density and velocity models. Knowing the variation in the mass flow rate per unit area helps to model and simulate the variation of the vehicle's velocity throughout the flight trajectory. Table 7 shows the corresponding velocity at different altitudes for $\rho_0 V_0 = 15 \frac{\text{lbm}}{\text{ft}^2 \text{ sec}}$.

Table 7: Velocity versus Altitude

Altitude (ft)	Velocity (ft/sec)
0	196
10,000	265
20,000	368
30,000	524
40,000	796
50,000	1287
60,000	2080
70,000	3376
80,000	5546
90,000	8958
95,000	11362
100,000	14557
110,000	23292

Curve Fitting

For the curve fitting process, a MATLAB program was developed using the method of least squares. The fitting process requires a model that relates the response data to the predictor data using one or more coefficients. To obtain the coefficient estimates, the least squares method minimizes the summed square of residuals. The residual shows the difference between the observed response data and the fitted response value.

$$R_i = f(x_i) - y_i$$
$$SSE = \sum_{i=1}^{n} R_i^2 = \sum_{i=1}^{n} \left(f(x_i) - y_i\right)^2 \qquad (5\text{-}19)$$

where “n” is the number of data points included in the fitting algorithm.

Residuals (R_i) are defined as the difference between the observed values of the dependent variable and the values that are predicted by the routine. The residuals approximate independent random errors. Goodness of fit refers to how well a statistical model fits a set of observed data. Confidence bounds are confidence

intervals for a predicted response. The width of the interval shows the degree of confidence of the fit. The details of the curve fitting process were shown in Chapter 3.

The Velocity Model

Using the curve fitting process, various predefined functions (custom equations and splines) are explored to fit the observed data. The general form of the velocity equation is modeled as:

$V = a \cdot \left(\exp\left(b \cdot y\right)\right)$ $\quad y \equiv \text{altitude} \,\&\, V \equiv \text{velocity}$

n=6

The coefficients (with 95% confidence bounds) are:

a = 114.8

b = 4.842×10^{-5}

Goodness of fit:

SSE = 1.189×10^{4}

R^2 = 0.9998

RMSE: 54.51

$$V = 114.8 \cdot \left(\exp\left(4.842 \times 10^{-5} \cdot y\right)\right) \qquad y \equiv \text{Altitude} \,\&\, V \equiv \text{Velocity} \quad (5\text{-}20)$$

$$\frac{\partial V}{\partial y} = 0.005586 \cdot \left(\exp\left(4.842 \times 10^{-5} \cdot y\right)\right) \quad (5\text{-}21)$$

The data, fit, and residuals are shown in Figure 53. The adjusted R^2 statistic is generally the best indicator of the fit quality when a new predefined function fits to the observed data. The measure of goodness of fit summarizes a low discrepancy between observed values and the values expected under the model in equation (5-20). The sum of squares due to error (SSE) and the adjusted R-square statistics are used to

help determine the best fit. The SSE statistic is the least squares error of the fit, with a value closer to zero indicating a better fit.

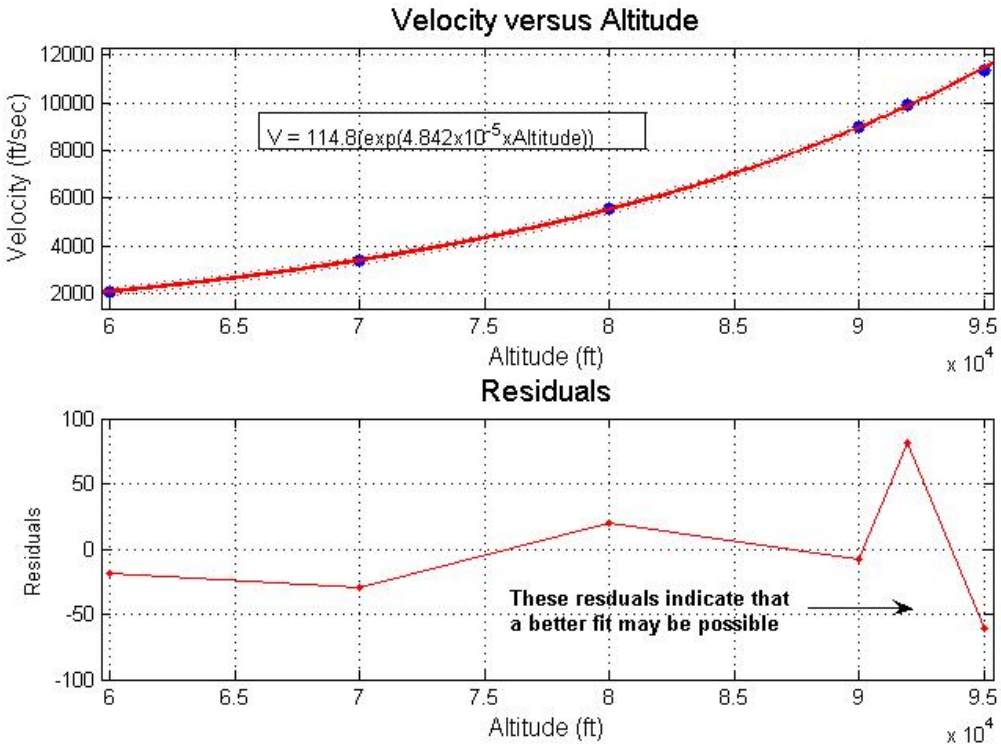

Figure 53: Variation of Velocity with Altitude

The Air Density

The exponential variation of air density with the altitude is modeled as:

$\rho = a \cdot \left(\exp\left(b \cdot y\right)\right)$ $y \equiv \text{altitude}\ \&\ \rho \equiv \text{air Density}$

n=24

The coefficients (with 95% confidence bounds) are:

a = 0.002451

b = 3.440×10^{-5}

Goodness of fit:

SSE = 8.213×10^{-8}

R^2 = 0.9946

$$\text{RMSE} = 4.422\times10^{-5}$$

$$\rho = 0.002451\left(\exp\left(-3.44\times10^{-5}\,y\right)\right) \qquad y \equiv \text{altitude} \qquad (5\text{-}22)$$

The data, fit, and residuals are shown in Figure 54. At low altitudes, the measure of goodness of fit summarizes a low discrepancy between observed values and the values expected under the model in equation (5-22). The model can be used for further analysis.

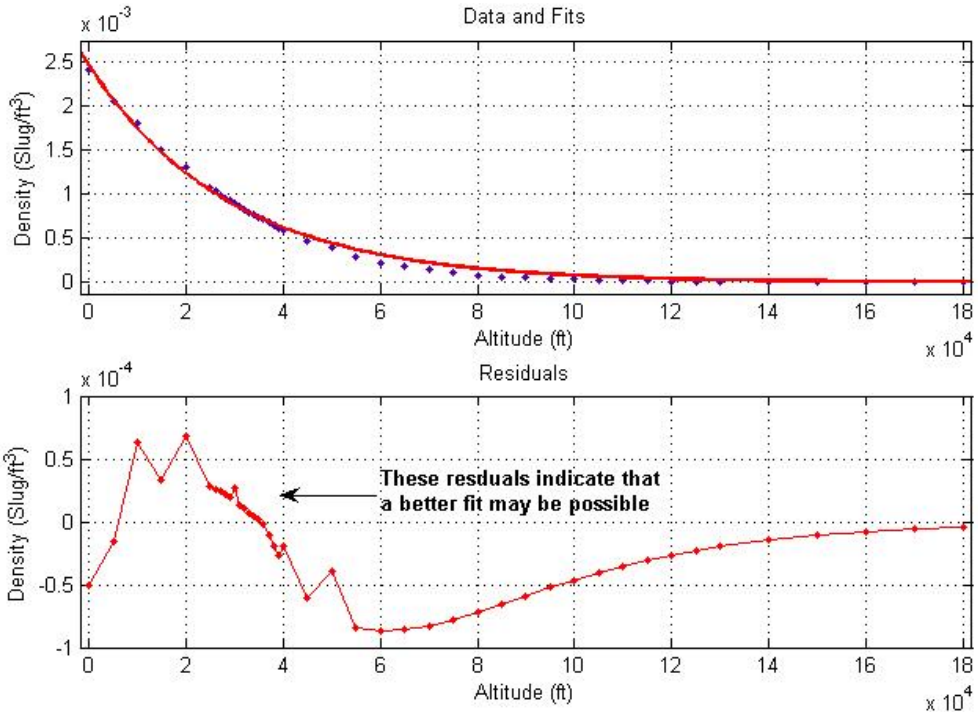

Figure 54: Variation of Air Density with Altitude

$(L/D)_{max}$ and Drag Polar

Using the aerodynamic models from Chapter 3, $(L/D)_{max}$ and the drag polar at different Mach numbers are modeled and the results are summarized in Figures 55 through 64. The thrust required for steady state flight is directly proportional to the gross weight of the GHV. The thrust required also depends on the ratio of lift to drag.

The ratio of lift to drag is a very important measure of the GHV's aerodynamic efficiency. The vehicle aerodynamic efficiency is a strong function of airspeed.

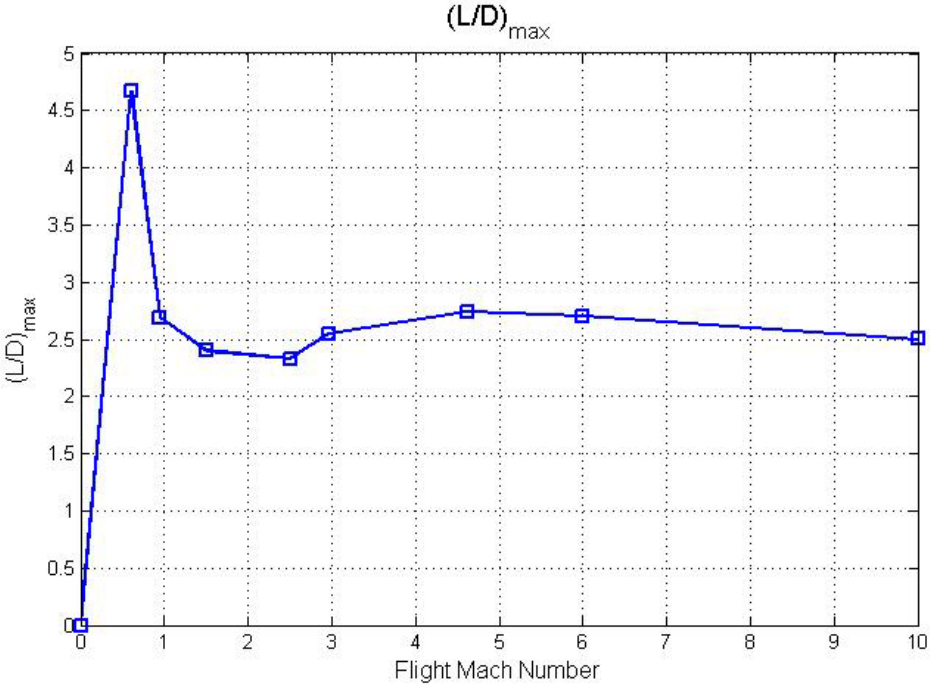

Figure 55: $(L/D)_{max}$

The drag force can be written as the parasitic drag plus the induced drag.

$$C_D = C_{DP} + \frac{CL^2}{\pi e_s R_A} \tag{5-23}$$

where e_s is the span efficiency factor and R_A is the aspect ratio.

$$C_D = \underbrace{C_{D0} + C_{D0,L} \cdot C_L + C_{D0,L^2} \cdot C_L{}^2}_{C_{DP}} + \frac{C_L{}^2}{\pi e_s R_A} \tag{5-24}$$

Combining the quadratic term from the parasitic drag with the induced drag, the total drag can be written as:

$$C_D = C_{D0} + C_{D0,L} \cdot C_L + \frac{C_L{}^2}{\pi e R_A} \tag{5-25}$$

where e is called Oswald efficiency factor.

The term on the right hand side of equation (5-25) is often called the induced factor even though it is the induced factor plus the quadratic term from the parasitic drag. In this research the change in the drag coefficient with respect to lift coefficient at zero lift is assumed zero (a very small), thus the value of $C_{D0,L}$ in equation (5-25) is assumed zero. The total drag can be written as:

$$C_D = C_{D0} + \frac{C_L^{\,2}}{\pi e R_A} = C_{D0} + \kappa \cdot C_L^{\,2} \qquad (5\text{-}26)$$

where $\kappa = \frac{1}{\pi e R_A}$

The minimum required thrust is approximated as:

$$\text{Thrust}_{min} \approx 2 \cdot W \cdot \sqrt{C_{D0} \cdot \kappa} \qquad (5\text{-}27)$$

The results for various Mach numbers are summarized in the following subsections under the studied Mach values.

M_0=0.60:

General model:

$$C_D = C_{D0} + \kappa \times C_L^{\,2}$$

The coefficients (with 95% confidence bounds) are:

C_{D0} = 0.01615 κ = 0.7102

<u>Goodness of fit:</u>

SSE = 8.574×10^{-6}

The measure of goodness of fit summarizes a low discrepancy between the observed values and the expected values. The model describes the data well.

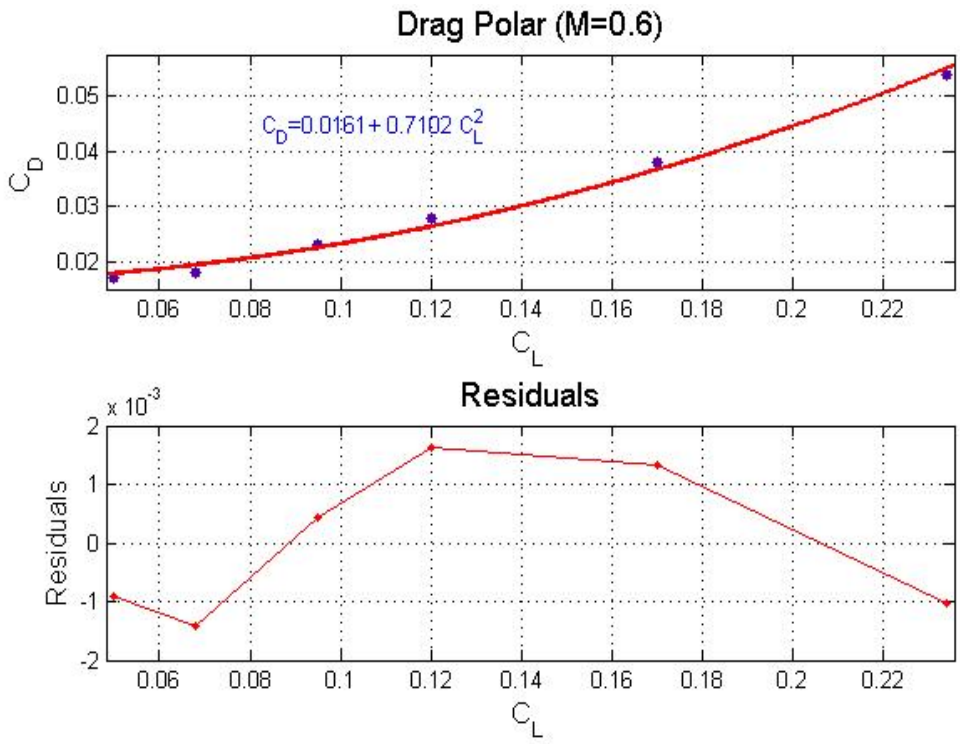

Figure 56: Drag Polar at M=0.60

M_0=0.95:

General model:

$$C_D = C_{D0} + \kappa \times C_L^{\,2}$$

The coefficients (with 95% confidence bounds) are:

$C_{D0} = 0.05609$

$\kappa = 0.6195$

Goodness of fit:

SSE = 8.316×10^{-6}

The measure of goodness of fit summarizes a low discrepancy between the observed values and the expected values. The model can be used for further analysis.

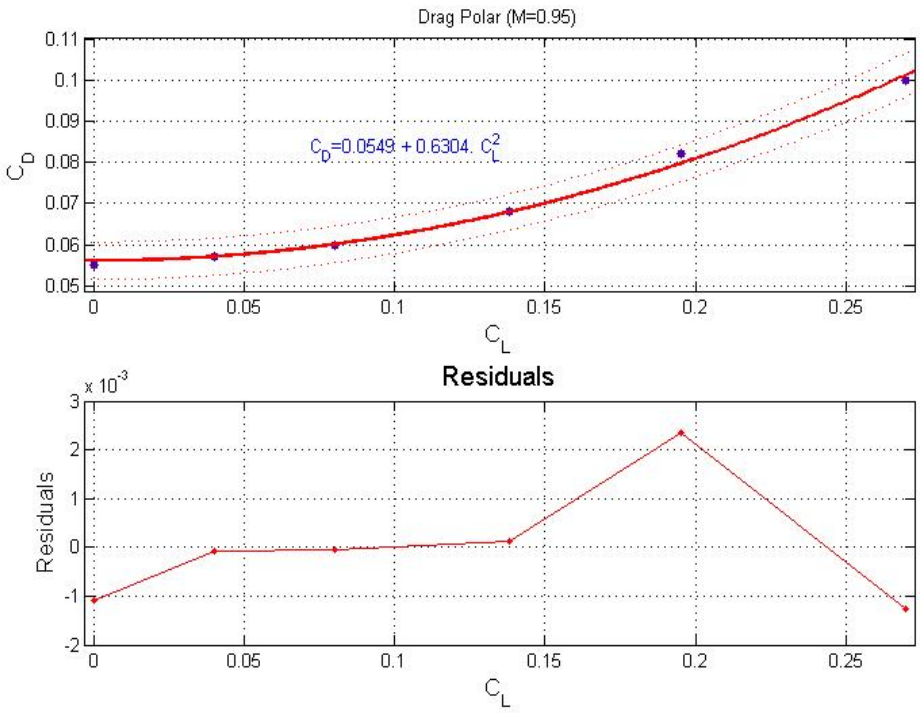

Figure 57: Drag Polar at M=0.95

M_0=1.50:

General model:

$$C_D = C_{D0} + \kappa \times C_L^{\ 2}$$

The coefficients (with 95% confidence bounds) are:

$C_{D0} = 0.0507$

$\kappa = 0.8533$

Goodness of fit:

SSE = 2.032×10^{-4}

The measure of goodness of fit summarizes a discrepancy between the observed values and the expected values. The model describes the data well.

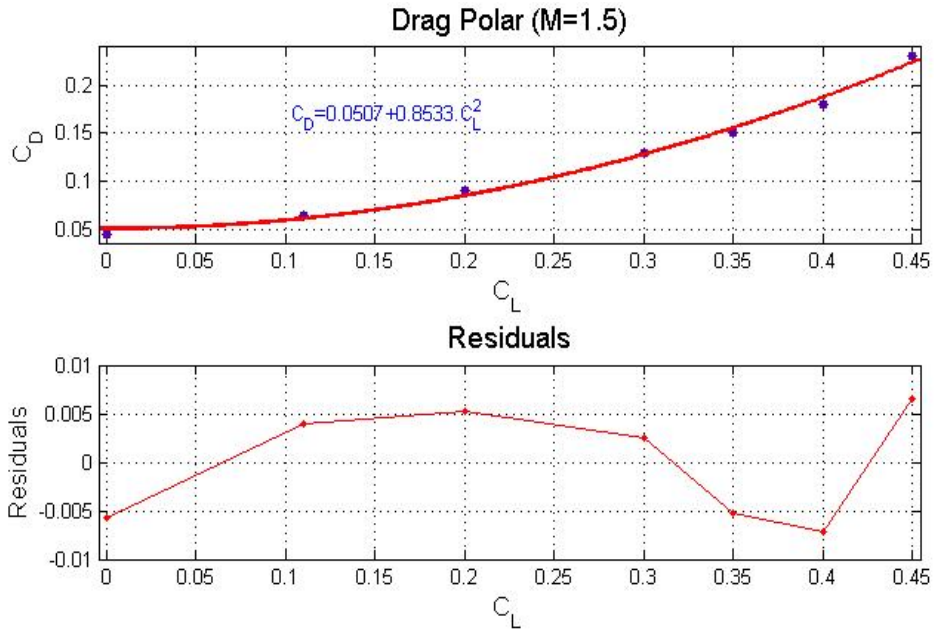

Figure 58: Drag Polar at M=1.5

M_0=2.50:

General model:

$$C_D = C_{D0} + \kappa \times C_L^{\,2}$$

The coefficients (with 95% confidence bounds) are:

$C_{D0} = 0.0504$

$\kappa = 0.9123$

Goodness of fit:

SSE = 8.365×10^{-4}

The measure of goodness of fit summarizes a low discrepancy between the observed values and the expected values. The model can be used for further analysis.

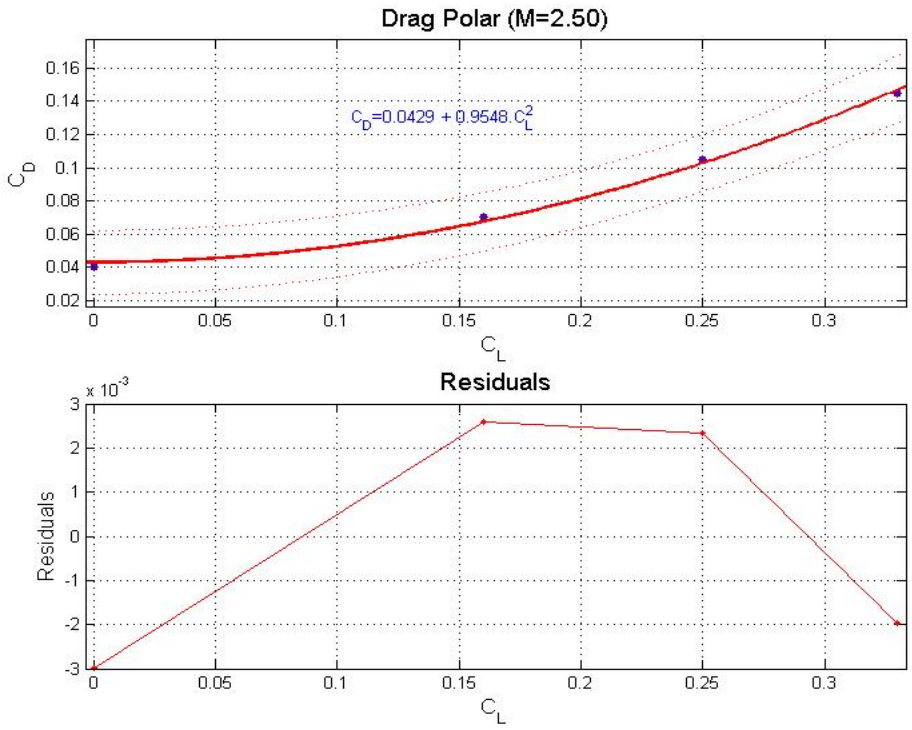

Figure 59: Drag Polar at M=2.50

M_0=2.96:

General model:

$$C_D = C_{D0} + \kappa \times C_L^{\,2}$$

The coefficients (with 95% confidence bounds) are:

$C_{D0} = 0.03562$

$\kappa = 1.081$

Goodness of fit:

SSE = 8.831×10^{-3}

The measure of goodness of fit summarizes a discrepancy between the observed values and the expected values. The model describes the data well.

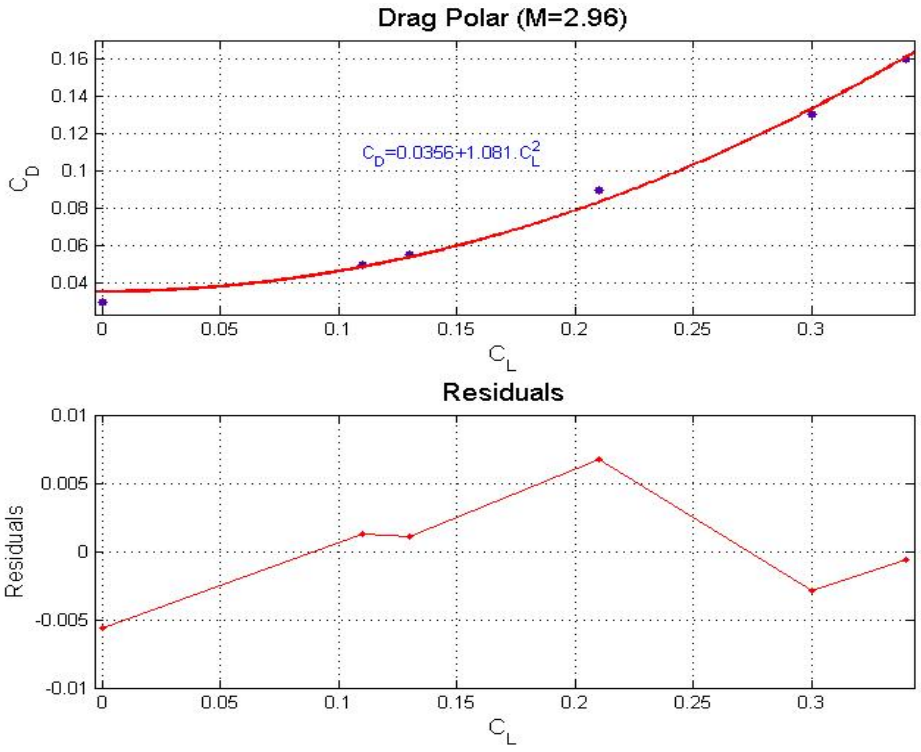

Figure 60: Drag Polar at M=2.96

M_0=3.95:

General model:

$$C_D = C_{D0} + \kappa \times C_L^{\,2}$$

The coefficients (with 95% confidence bounds) are:

$C_{D0} = 0.03562$

$\kappa = 1.081$

<u>Goodness of fit:</u>

SSE = 8.831×10^{-3}

The measure of goodness of fit summarizes a low discrepancy between the observed values and the expected values. The model can be used for further analysis.

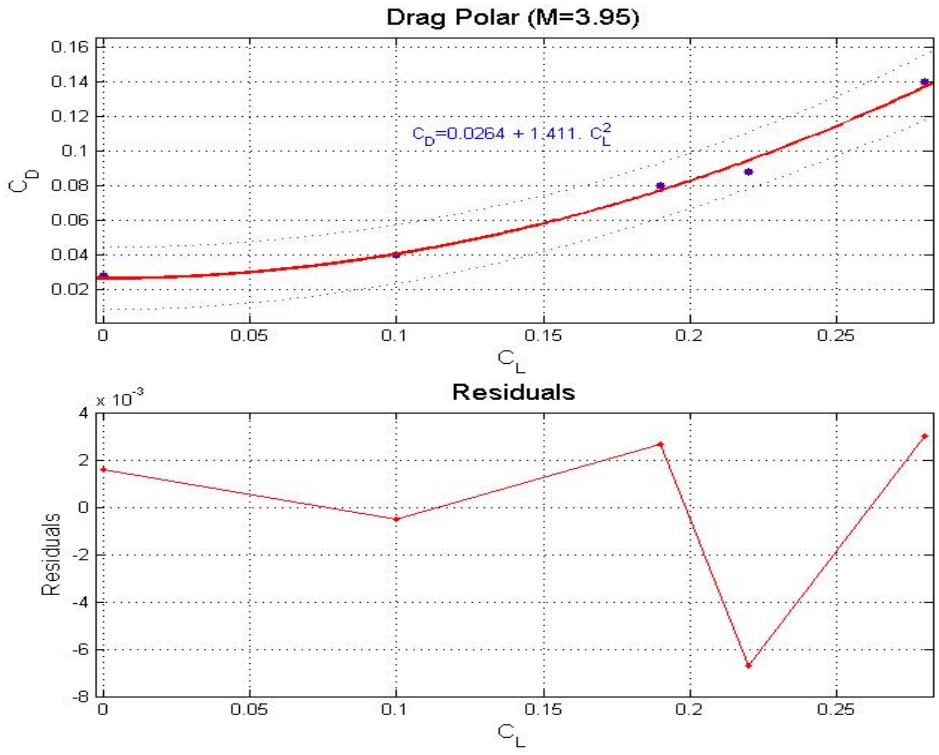

Figure 61: Drag Polar at M=3.95

M_0=4.63:

General model:

$$C_D = C_{D0} + \kappa \times C_L^{\ 2}$$

The coefficients (with 95% confidence bounds) are:

C_{D0} = 0.0214

κ = 1.559

Goodness of fit:

SSE = 1.66×10^{-6}

The measure of goodness of fit summarizes a low discrepancy between the observed values and the expected values. The model describes the data well.

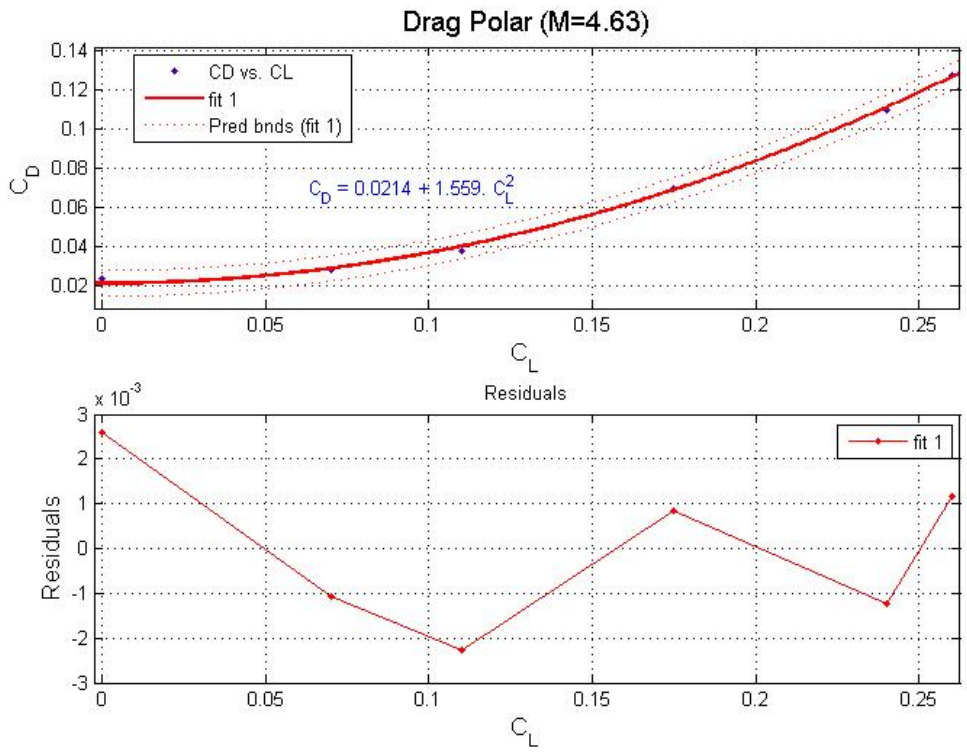

Figure 62: Drag Polar at M=4.63

M_0=6.00:

General model:

$$C_D = C_{D0} + \kappa \times C_L{}^2$$

$$\left(\frac{C_L}{C_D}\right)_{max} = 2.7 = \frac{1}{2\sqrt{\kappa C_{D0}}}$$

where, $C_{D0} = 0.02 \Rightarrow \kappa = 1.7147$

The drag polar at M=6.0 is modeled using $\left(\frac{C_L}{C_D}\right)_{max}$ (Figure 55) and the results from the aerodynamic model of the GHV (Appendix A).

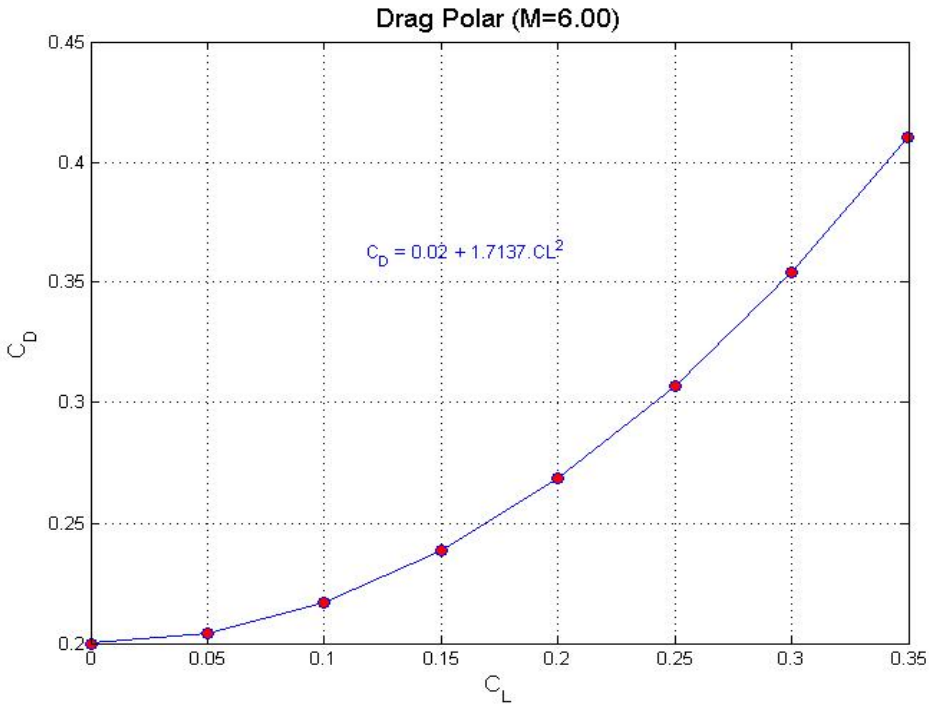

Figure 63: Drag Polar at M=6

M_0=10.00:

General model:

$$C_D = C_{D0} + \kappa \times C_L{}^2$$

$$\left(\frac{C_L}{C_D}\right)_{max} = 2.5 = \frac{1}{2\sqrt{\kappa C_{D0}}}$$

where, $C_{D0} = 0.01 \Rightarrow \kappa = 4.00$

The drag polar at M=10.0 is modeled using $\left(\frac{C_L}{C_D}\right)_{max}$ (Figure 55) and the results from the aerodynamic model of the GHV (Appendix A).

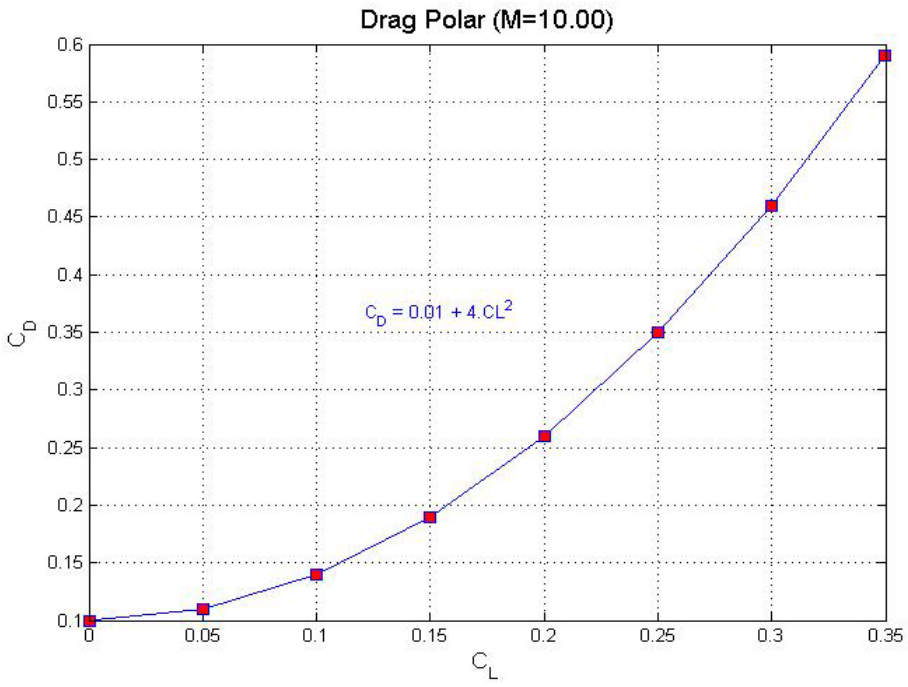

Figure 64: Drag Polar at M=10

Thrust

One important performance measure for the GHV is the thrust required to maintain steady state level flight. For steady State Flight there is no acceleration and no change in altitude. During level unaccelerated flight, the wing must provide sufficient lift to balance the weight of the GHV and the engine must provide enough thrust to balance the drag force. The propulsion system of the GHV is modeled in Chapter 4. The variation in the minimum required thrust force through the flight trajectory for steady state flight is modeled at different Mach numbers. The minimum required thrust is calculated using the drag polar at different flight Mach numbers. In this research, optimization techniques are applied only to a supersonic-hypersonic portion of the flight trajectory [$2.148 < M_0 < 15.01$] and it is limited to altitude between 60,000 to 100,424 ft. Although some subsonic and some supersonic Mach numbers are out of

the scope of this optimization research, the minimum required thrust at these conditions is calculated. The C_{D0} and κ are two important parameters to calculate the minimum thrust for steady state flight at the different Mach numbers. Using information from the drag polars, the minimum required thrust force is calculated at different flight Mach numbers in the following section.

The minimum required thrust is modeled as:

$$\text{Thrust}_{min} = 1033 \cdot M^2 - 1.353 \times 10^4 . M + 1.524 \times 10^5 \quad (5\text{-}28)$$

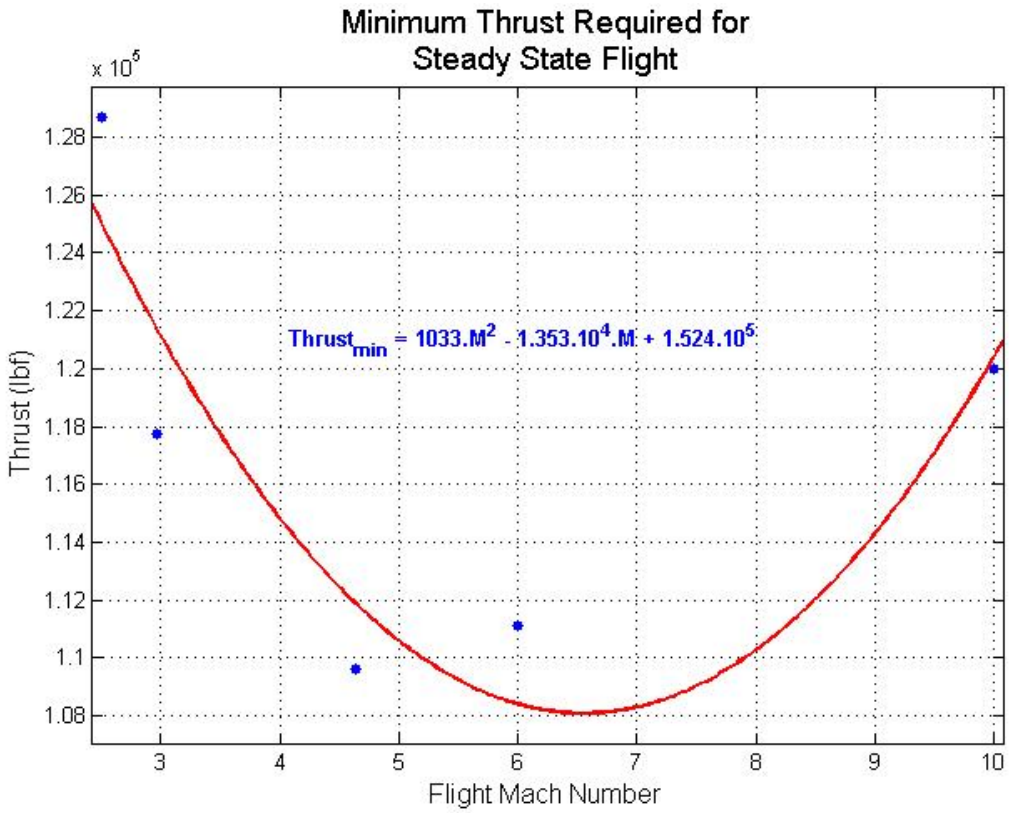

Figure 65: Minimum Required Thrust

As was discussed in previous section, the vehicle aerodynamic efficiency is a strong function of airspeed thus the minimum required thrust varies with the flight Mach

number. The minimum required thrust varies due to the variation in the parasitic drag plus the induced drag. Although the speed of sound varies with the altitude, in this research the variation in the speed of sound with altitude is ignored. An average value is used for the conversion of Mach number into velocity.

$$M = \frac{V}{a_{ave}}$$

$$a_{ave} = 980 \text{ ft/sec}$$

$$\text{Thrust}_{min} = 1033 \cdot \left(\frac{V}{980}\right)^2 - 1.353 \times 10^4 \cdot \left(\frac{V}{980}\right) + 1.524 \times 10^5 \tag{5-29}$$

$$\text{Thrust}_{min} = 0.0011 \cdot V^2 - 13.81 \cdot V + 1.524 \times 10^5$$

$$\frac{\partial \text{Thrust}_{min}}{\partial V} = 0.0022 \cdot V - 13.81 \tag{5-30}$$

Air Mass Flow Rate and Fuel Air Ratio

The air mass flow rate is modeled as a function of Mach number. This model is developed using the Chapter 4 engine model (specific thrust) and the minimum required thrust force for steady state flight.

$$\text{Thrust}_{min} = I_{sp} \times \dot{m}_{air} \qquad \dot{m}_{air} \equiv \dot{m}_0 \tag{5-31}$$

$$\dot{m}_0 = \frac{\text{Thrust}_{min}}{I_{sp}} = (\rho \cdot V)_{air} \cdot A$$

Considering that the optimum value for a constant air mass flow rate per unit area is taken to be $15 \frac{\text{lbm}}{\text{ft}^2 \text{ sec}}$, the minimum required inlet capture area is found as:

$$A = \frac{\text{Thrust}_{min}}{I_{sp} \cdot (\rho \cdot V)_{air}} \tag{5-32}$$

Table 8: Air Mass Flow Rate

M	Thrust (lbf)	Isp(second)	$\rho_0 V_0$ lbm/ft^2.sec)	$(dm/dt)_{air}$ (lbm/sec)	A_{inlet}(ft^2)
2.50	128658	2212	15.00	569.19	38.04
2.96	117736	2135	15.00	539.69	36.07
4.63	109618	1855	15.00	578.29	38.65
6.00	111112	1625	15.00	668.97	44.71
10.00	120000	955	15.00	1229.67	82.19

The air mass flow rate is modeled as a function of flight Mach numbers:

$$\dot{m}_0 = 6.735 \cdot M^2 - 43.48 \cdot M + 320.6 \qquad (5\text{-}33)$$

Goodness of fit:

SSE: 58.07

The measure of goodness of fit summarizes a discrepancy between the observed values and the expected values. This goodness of fit indicates that a better fitting model may possible.

The engine model developed in Chapter 4 is used to find a model for the variation in fuel air ratio as a function of flight Mach number as follows:

$$f = 0.0002454 \cdot M^2 - 0.0008707 \cdot M + 0.002119 \qquad f \equiv \text{fuel air ratio} \qquad (5\text{-}34)$$

Goodness of fit:

SSE: 1.78e-007

The measure of goodness of fit summarizes a low discrepancy between observed values and the values expected under the model.

Drag Coefficient

The drag coefficient is modeled in Chapter 3 as a function of Mach number, angle of attack, and control surface deflection angles. In this section, a clean drag coefficient is

modeled and developed solving nonlinear curve-fitting (data-fitting) problems in the least-squares sense.

Supersonic Speeds:

$$C_D = 3.7912\times10^{-2} + 4.4563\times10^{-4}\cdot\alpha^2 - 3.9357\times10^{-3}\cdot M$$

$$\text{where, } M = \frac{V_0}{a_{ave}}$$

$$a_{ave} = 980 \text{ ft/sec} \qquad (5\text{-}35)$$

$$C_D = 3.7912\times10^{-2} + 4.4563\times10^{-4}\cdot\alpha^2 - 4.016\times10^{-6}\cdot V$$

$$\frac{\partial C_D}{\partial V_0} = -4.016\times10^{-6} \qquad (5\text{-}36)$$

Hypersonic Speeds:

$$C_D = 8.0052\times10^{-3} + 2.3936\times10^{-4}\cdot\alpha^2 - 6.2594\times10^{-4}\cdot M$$

$$\text{where, } M = \frac{V_0}{a_{ave}}$$

$$a_{ave} = 980 \text{ ft/sec} \qquad (5\text{-}37)$$

$$C_D = 8.0052\times10^{-3} + 2.3936\times10^{-4}\cdot\alpha^2 - 6.3871\times10^{-7}\cdot V_0$$

$$\frac{\partial C_D}{\partial V_0} = -6.3871\times10^{-7} \qquad (5\text{-}38)$$

5.4. Optimization Process

The fundamental equation for the optimization process is:

$$F = V\cdot\cos\gamma + \lambda_V\left(m\dot{V} - T + q\cdot S\cdot C_D + m\cdot g\cdot\sin\gamma\right) \qquad (5\text{-}11)$$

where, from equation (5-12), the time varying Lagrange multiplier is calculated as:

$$\dot{\lambda}_V = \cos(\gamma) + \lambda_V \left[-\frac{\partial(T)}{\partial V} + \rho \cdot V \cdot C_D \cdot S + 0.5 \cdot \rho \cdot V^2 \cdot S \cdot \frac{\partial(C_D)}{\partial V} \right] \qquad (5\text{-}39)$$

where $\gamma = \gamma(t)$ is determined by applying equation (5-13) which may be written as:

$$\lambda_v(t) \cdot \cos(\gamma) \cdot W = V \cdot \sin(\gamma)$$

The variation in the thrust force with flight velocity is calculated using equation (5-30). The numerical value of the drag coefficient and its variation with flight velocity are calculated using equations (5-35) through (5-38).

Numerical Analysis

As was shown in equation (5-3), the control vector, $[\gamma]$, is optimized with the flight velocity over the entire flight trajectory. Considering that the flight path angle is a primary function of the flight velocity, the fundamental equation (5-11) is formally dependent on the time. A combination of classical numerical methods plus MATLAB and MathCAD programming techniques are used for the optimization of the flight path angle throughout the flight trajectory.

$$\lambda_v(t) \cdot \cos(\gamma) \cdot W = V \cdot \sin(\gamma)$$

$$\sin(\gamma) = \frac{\lambda_v(t) \cdot \cos(\gamma) \cdot W}{V} \Rightarrow \qquad (5\text{-}13)$$

$$\tan(\gamma) = \frac{\lambda_v(t)\cdot W}{V} \Rightarrow$$

$$\gamma = \tan^{-1}\left[\frac{\lambda_v(t)\cdot W}{V}\right] \quad (5\text{-}40)$$

The substitution of equation (5-40) into equation (5-39) yields:

$$\dot{\lambda}_V = \cos\left(\tan^{-1}\left[\frac{\lambda_v(t)\cdot W}{V}\right]\right) + \lambda_V(t)\left[-\frac{\partial(T)}{\partial V} + \rho\cdot V\cdot C_D\cdot S + 0.5\cdot\rho\cdot V^2\cdot S\cdot\frac{\partial(C_D)}{\partial V}\right] \quad (5\text{-}41)$$

Equation (5-32) is rewritten as:

$$\dot{\lambda}_V = \left(\frac{1}{\left[1+\left(\frac{\lambda_v(t)\cdot W}{V}\right)^2\right]^{1/2}}\right) + \lambda_V(t)\left[-\frac{\partial(T)}{\partial V} + \rho\cdot V\cdot C_D\cdot S + 0.5\cdot\rho\cdot V^2\cdot S\cdot\frac{\partial(C_D)}{\partial V}\right] (5\text{-}42)$$

The flight path angle is a function of time. There is no exact solution to equation (4-42). The 4th-order Runge–Kutta numerical method is accurate to the fourth-order term of Taylor's expansion.

A time-marched solution using the 4th-order Runge–Kutta numerical method is used to solve the ODE equation (5-42) as follows:

$$\dot{\lambda}v = f(\lambda v, \gamma, t) \qquad \gamma = g(t) \qquad \lambda v(t_0) = \lambda v_0 \quad (5\text{-}43)$$

The fourth-order Runge–Kutta method for this problem is given by the following equation:

$$\lambda v_{n+1} = \lambda v_n + \frac{h}{6}\left(k_1 + 2k_2 + 2k_3 + k_4\right) \tag{5-44}$$

where $\frac{h}{6}\left(k_1 + 2k_2 + 2k_3 + k_4\right)$ is called the increment function. The local truncation error is *O* (h^5). The size of the interval is taken as (h) and the increment function is expressed as:

$$k_1 = \lambda v\left(\lambda v_n, t_n\right)$$

$$k_2 = \lambda v\left(\frac{h}{2}k_1, t_n + \frac{h}{2}\right)$$

$$k_3 = \lambda v\left(\frac{h}{2}k_2, t_n + \frac{h}{2}\right) \tag{5-45}$$

$$k_4 = \lambda v\left(\lambda v_n + h \cdot k_3, t_n + h\right)$$

The 4th-order Runge–Kutta method does not require the derivatives of $f\left(\lambda v, \gamma, t\right)$. It produces a result equivalent to the high order Taylor formula. The most important advantage of Runge–Kutta methods in this research is that they solve the problem using only one initial point. The 4th-order Runge–Kutta calculates λv_{n+1} using the value of present λv_n plus the slope at the beginning of the interval (k_1), the slope at the midpoint of the interval (k_2), the slope at the midpoint (k_3), and the slope at the end of the interval (k_4). Although, the 4th-order Runge–Kutta method is used to solve ordinary differential equations, a MathCAD program, ***flightpath.mcd,*** is used for all

simultaneous analytical calculations and a MATLAB program, ***flightpath.m***, is used to solve nonlinear equations. The input of the computer programs is the flight altitude. The flight velocity is calculated applying equation (5-18). The MathCAD program, ***flightpath.mcd*** generates a time varying ordinarily differential equation (ODE). The 4^{th}-order Runge–Kutta method generates solutions to this ODE and then the nonlinear equations are solved using the MATLAB program, ***flightpath.m***. The nature of hypersonic flight implies a very small sampling time. In this research, the size of the interval is taken as 0.2 seconds and both the simulation and optimization routines are updated every 0.2 seconds. The optimized flight path angle plus the input velocity provide enough information to update the flight altitude every 0.2 seconds. The MathCAD routine can also calculate the fuel air ratio, the mass flow rate, and the consumed fuel mass every 0.2 seconds. Knowing the optimized flight path angle plus the variation of the velocity and the altitude enables the MathCAD routine to update the Mach number, the drag coefficient, and thrust force variation with velocity accordingly.

5.5. Results

The following figures show the results from the optimization process over a broad range of Mach numbers.

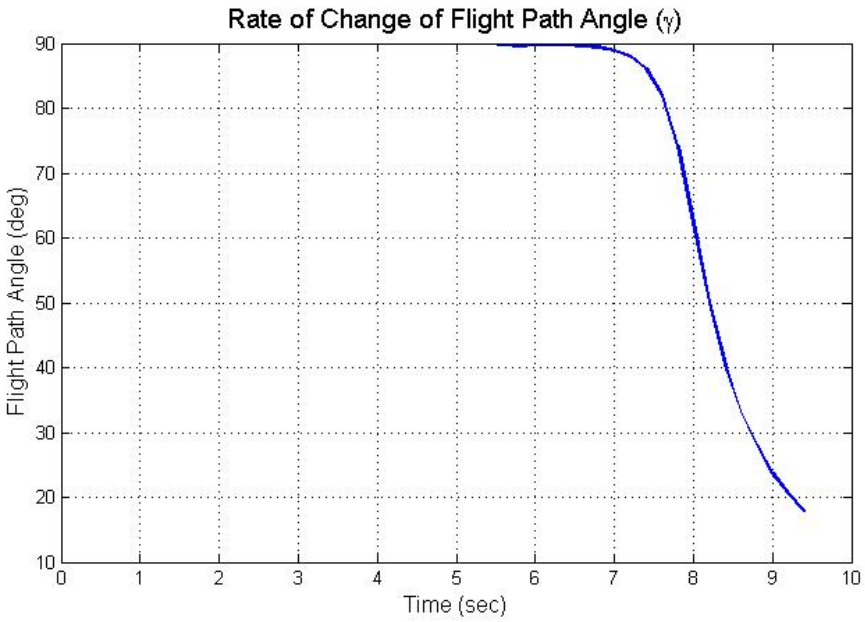

Figure 66: Rate of Change of Flight Path Angle

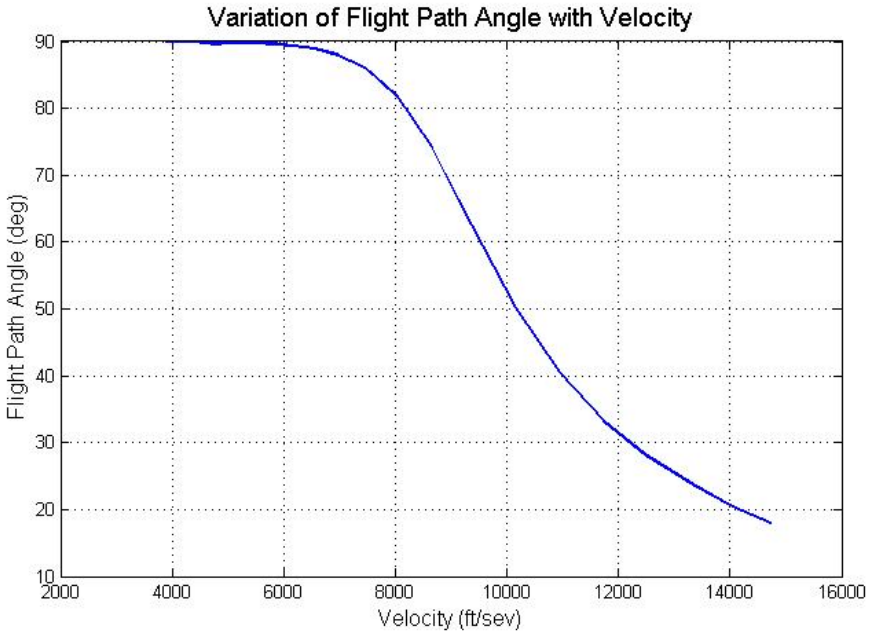

Figure 67: Variation of Flight Path Angle with Velocity

As shown in Figure 66, for the first 6 seconds the flight path angle is constant and stays at 90 degrees. There are two reasons for the vertical flight of the vehicle. The first reason is that the air density is a function of altitude. The second is that the induced drag coefficient decreases with the increase in the flight Mach number. The flight path angle is reduced when the total drag force is reduced. A very small variation in the drag coefficient causes a large change to the results of the optimization. Figure 68 shows the position of the vehicle (X, Y) or (range, altitude) throughout the flight trajectory.

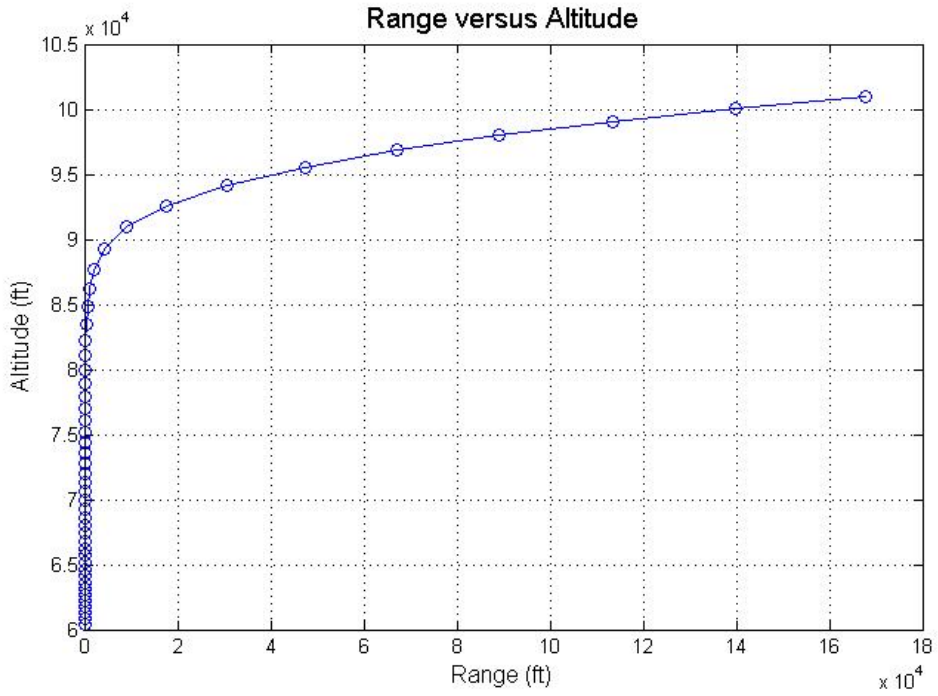

Figure 68: Range versus Altitude

The fuel mass flow rate increases with the velocity exponentially. Figures 69 and 70 show how fuel injection becomes challenging at high Mach numbers. The fuel mass flow needs to be sustained at a very high rate in order to continue hypersonic flight at high Mach numbers. Keeping the fuel mass flow rate at such a very high rate (e.g.

115 lbm/sec) is a difficult task. This is not only due to the flow rate itself, but it can also cause a dramatic increase in the empty weight of the vehicle.

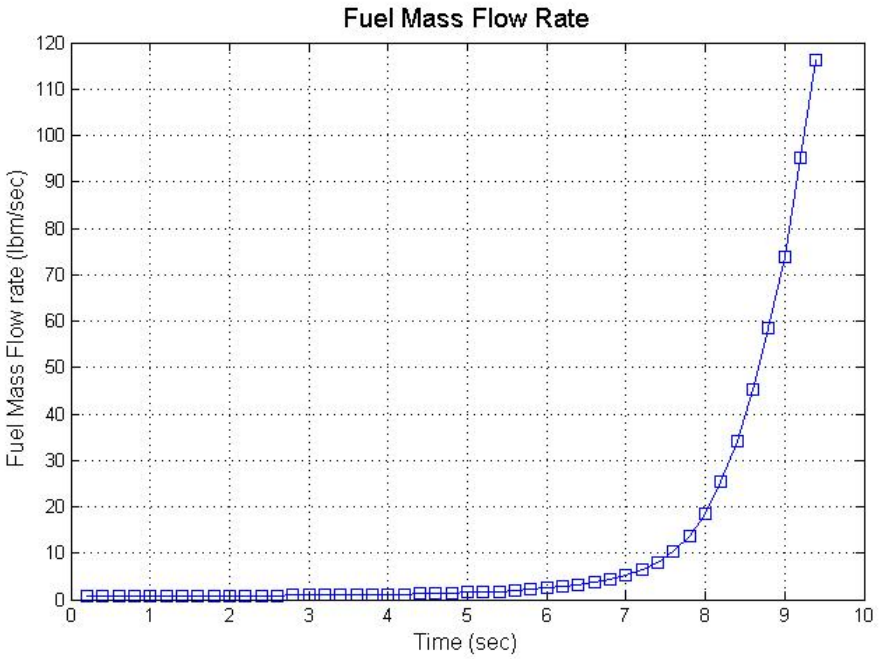

Figure 69: Fuel Mass Flow Rate

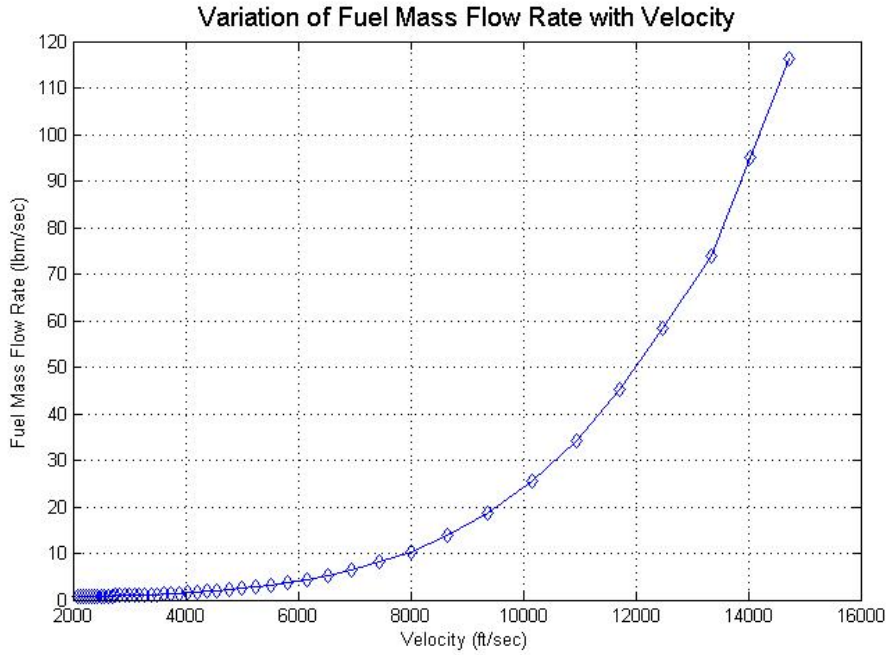

Figure 70: Variation of Fuel Mass Flow Rate with the Velocity

The weight of the vehicle varies as a function of the fuel mass flow rate. In a numerical analysis of the weight due to velocity (W/V), the analysis is updated every 0.2 second as a function of time. Figures 71 and 72 show the rate of change of (W/V) through flight trajectory, as well as their variation with velocity.

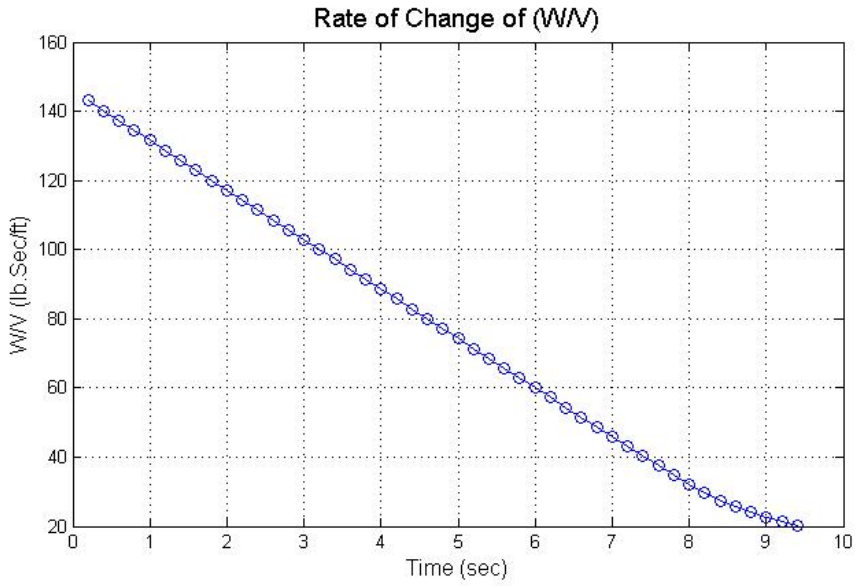

Figure 71: Rate of Change of (W/V)

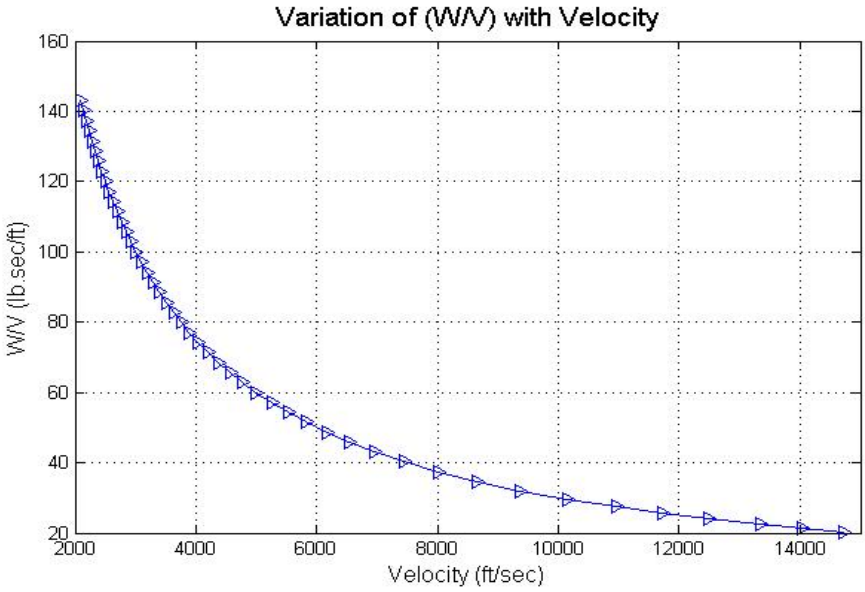

Figure 72: Weight to Velocity Ratio

The velocity of the vehicle reaches a predefined value of 14,000 ft/sec in about 9 seconds. Large acceleration big values are required to reach a very high velocity in a very short time (9 seconds). The vehicle acceleration increases with velocity up to 8.6 seconds then it decreases. The odd behavior of the vehicle at V=13,336 ft/sec needs to be investigated separately.

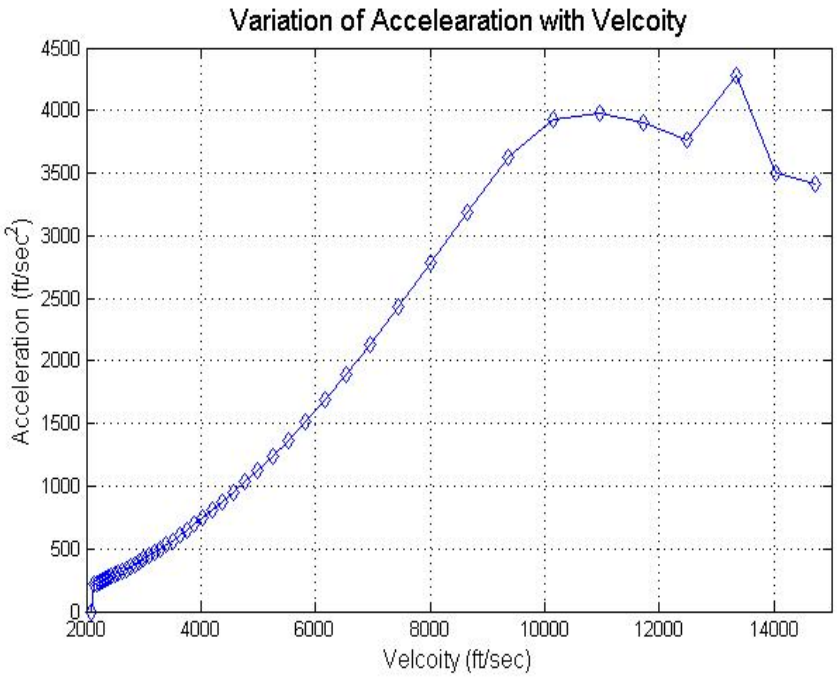

Figure 73: Acceleration

5.6. Summary

This research covers the development of an optimized trajectory, one generated for different thrust specific force values. The model and the simulation are developed to support conceptual design studies of hypersonic vehicles. The aerodynamic database for the generic hypersonic vehicle uses experimental wind tunnel data and the results from multiple CFD codes. The simulation includes an optimized trajectory and a

flight path angle calculated at every point along the flight path to maximize the range. A MATLAB routine (***trajectory.m***) is developed specifically for this application.

Chapter 6: Modeling and Simulation

6.0. Introduction

This chapter covers the development of a six degrees of freedom simulation of a generic hypersonic vehicle (GHV) using the merged aerodynamic database that was presented in Chapter 3. The simulation includes the air-breathing propulsion engine cycles presented in Chapter 4. This work is developed to support conceptual hypersonic vehicle design studies and related aerospace vehicle technologies.

6.1. Simulation Process

The equations of motion for a six degrees of freedom (12 states) simulation of a generic hypersonic vehicle (GHV) is presented in Chapter 2. The mathematical models of the aerodynamic database and propulsion system are developed in Chapters 3 and 4. The simulation is implemented within a MATLAB routine. Applying the Jacobian technique and the MATLAB programs ***TRIMMER.m*** and ***SIMPLEX.m***, the GHV steady state model is simulated throughout the trajectory [27].

The state variables are:

$$X = \begin{bmatrix} V_t \\ \alpha \\ \beta \\ \phi \\ \theta \\ \psi \\ P \\ Q \\ R \\ N.D. \\ E.D. \\ Alt. \end{bmatrix} \qquad (6\text{-}1)$$

$$U = \begin{bmatrix} \delta_{Thtl} \\ \delta_e \\ \delta_a \\ \delta_{rud} \end{bmatrix} \tag{6-2}$$

$$\cos t = X(1)^2 + 100 \times (X(2)^2 + X(3)^2) + 10 \times (X(7)^2 + X(8)^2 + X(9)^2) \tag{6-3}$$

The MATLAB program, ***SIMPLEX.m,*** performs the minimization using a Nelder and Mead simplex algorithm. This method only uses cost function values; it does not need derivatives and does not attempt to compute approximations to the derivatives.

The constraints are applied for the steady state pull-up flight condition. The following figures show the simulation results and the trim points throughout the flight trajectory. The steady state performance of the GHV is investigated throughout the flight trajectory using a set of trimmed flight conditions. The lift and drag coefficients, the thrust force, the sideslip angle, the bank angle, and the pitch angle are determined for a number of different flight conditions. The results are summarized in Figures 74 through 78. At low supersonic speeds (lower dynamic pressures) a high value of the lift coefficient is required to support the GHV weight. This results in a large angle of attack and therefore a high induced drag. This means a higher thrust value is needed to overcome the drag force. In this region opening the throttle produces an increase in altitude but not an increase in speed. The nominal speed, altitude, and flight path angle are chosen to simulate the flight condition. As shown in Figures 76 and 77, α (angle of attack) and θ (pitch angle) vary together. This means there is a very little change in the flight path angle.

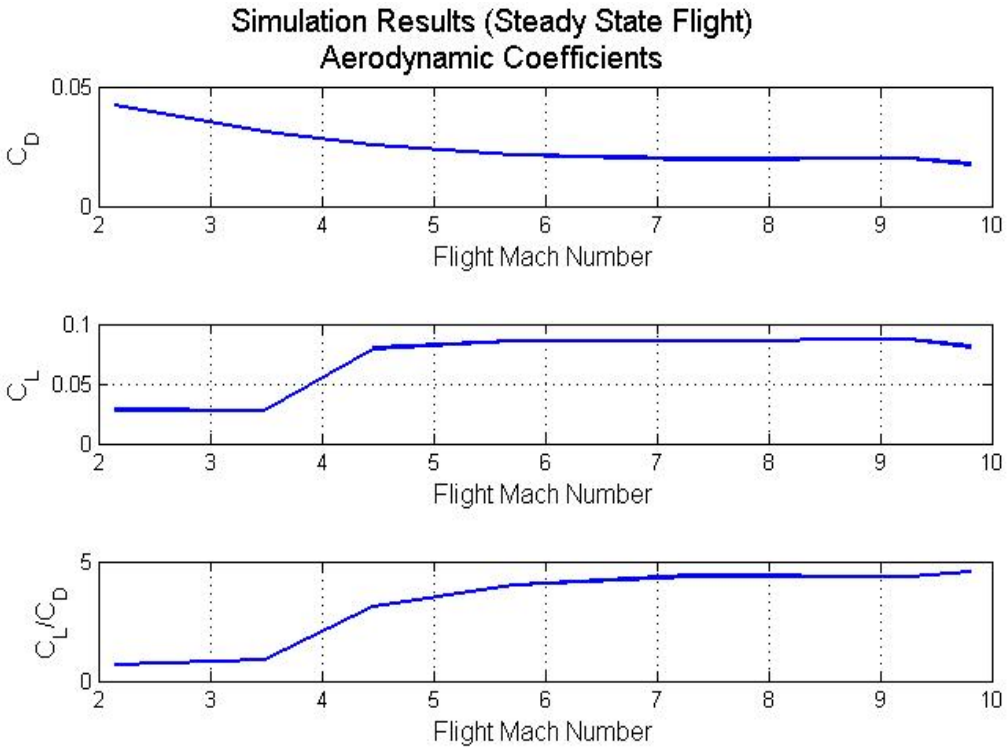

Figure 74: Variation in the Aerodynamic Coefficients

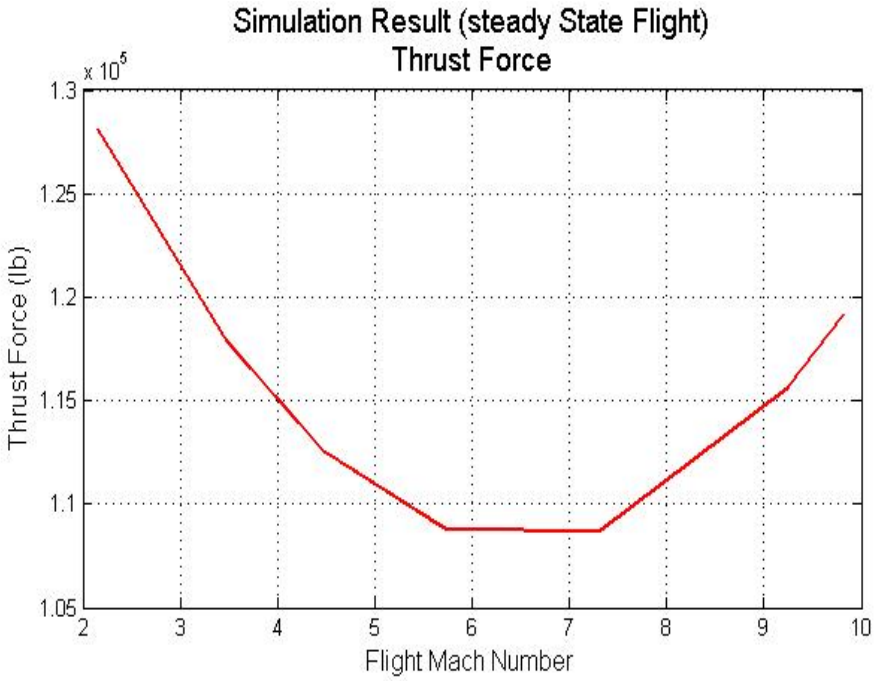

Figure 75: Thrust versus Flight Mach Number with Mach Number

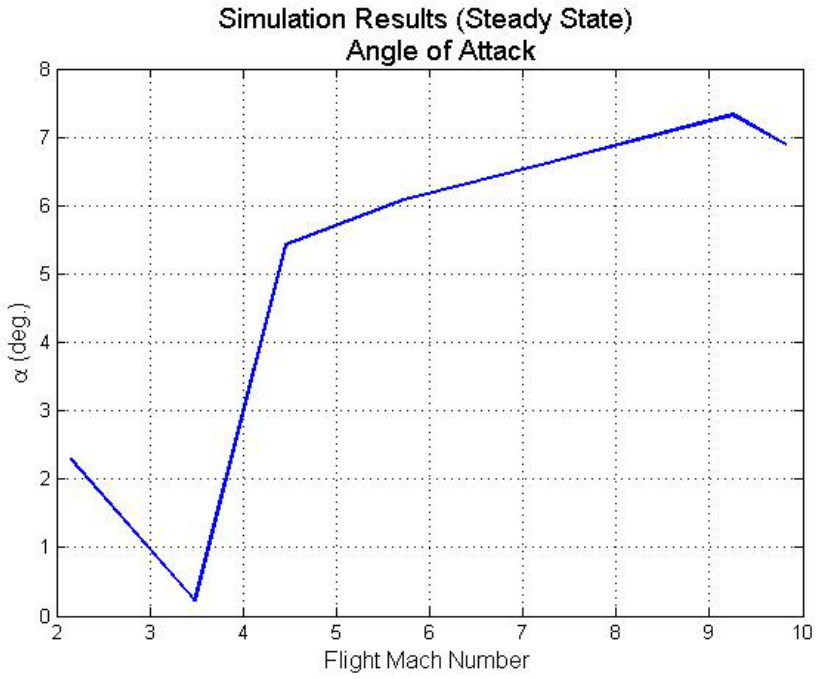

Figure 76: Variation of Angle of Attack with Mach Number

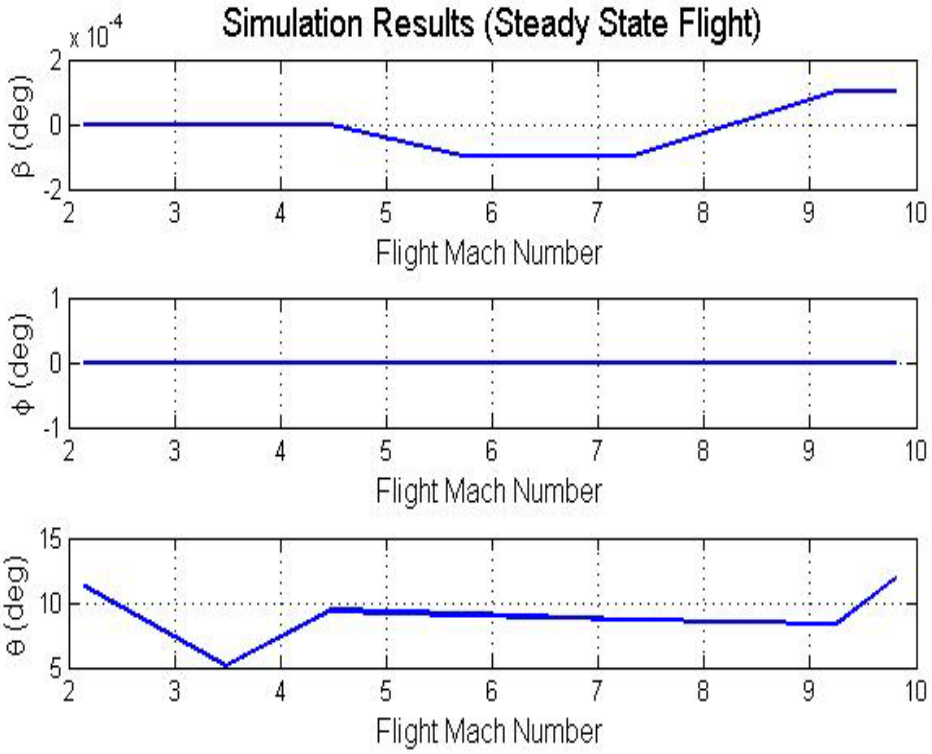

Figure 77: Variation in Sideslip Angle, Bank Angle, and Pitch Angle with Flight Mach Number

If a numerical solution approaches the exact solution, the numerical method is said to be convergent. All the convergence values are found to be very small (in most cases they approach zero).

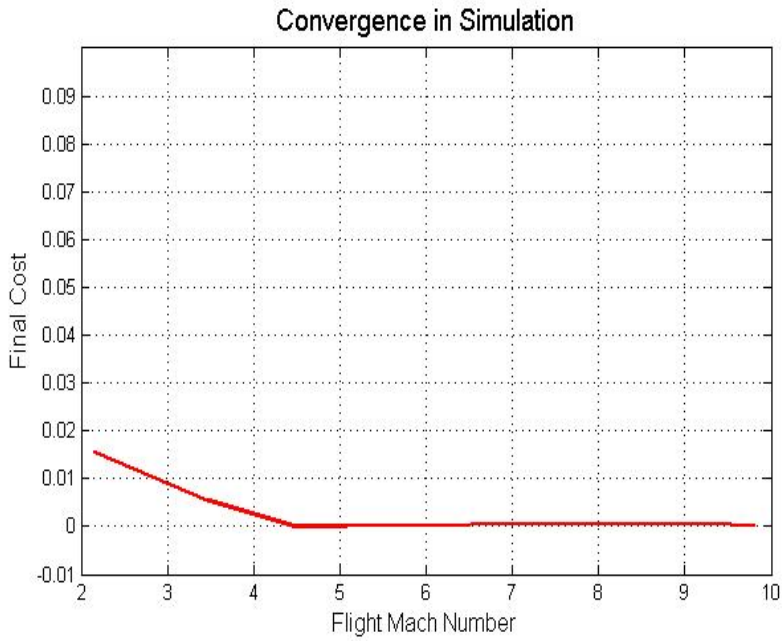

Figure 78: Convergence in Simulation with Mach Number

6.2. NUMERICAL LINEARIZATION PROCESS

A MATLAB program (***LIN.m***) was written to calculate the Jacobian matrices for the set of nonlinear state equations. The linearization algorithm chooses smaller and smaller perturbations in the independent variable and then compares three successive approximations to these partial derivatives. If these approximations agree within a certain tolerance, then the algorithm is terminated. Otherwise, the size of the perturbation is made smaller. The linearized model is derived for straight and level flight at the specified velocity and altitude with a zero banking angle. In this case, the longitudinal and the lateral subsystems are decoupled.

The linearized model about a trim point is:

$$\dot{X} = AX + BU$$
$$Y = CX + DU \tag{6-4}$$

Also, the state variables are defined as:

$$X = \begin{bmatrix} V_t \\ Alt \\ \alpha \\ \theta \\ Q \\ \beta \\ \phi \\ P \\ R \end{bmatrix} \tag{6-5}$$

The control variables are defined as:

$$U = \begin{bmatrix} \delta_{Thtl} \\ \delta_e \\ \delta_a \\ \delta_{rud} \end{bmatrix} \tag{6-6}$$

The output variables are defined as:

$$y = \begin{bmatrix} a.\ n. \\ q \\ \alpha \end{bmatrix} \tag{6-7}$$

The following flow chart shows the process of linearization and the simulation of the GHV (see Figure 79). The result of the linearization process gives us a linearized model of the GHV at each trim point. The model can be used for any control and navigation research problem. Considering the fact that the speed range of this vehicle

is very wide, the capability of the controller to stabilize, guide, navigate, and control the vehicle needs to be checked using multiple linear models at different trim points.

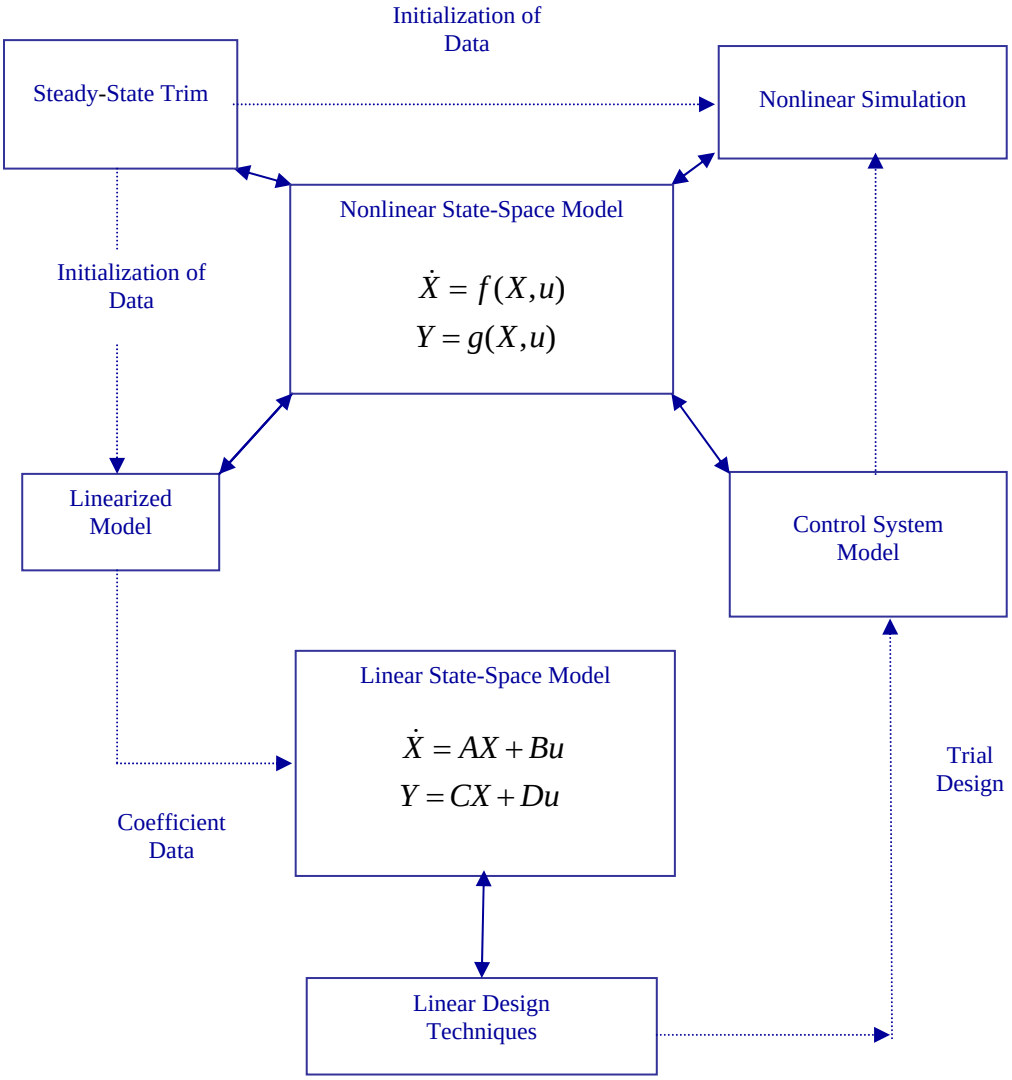

Figure 79: Linearization Flow Chart

The following are example A, B, C, and D matrices for the GHV model trimmed at Mach = 5.0 and Alt = 65,000 ft. in straight and level flight.

$$A = \left[\begin{array}{ccccc|cccc}
-1.604E\text{-}04 & 5.768E\text{-}04 & -6.238E+03 & -3.121E+01 & 1.940E\text{-}14 & 0.000E+00 & 0.000E+00 & 0.000E+00 & 0.000E+00 \\
1.737E\text{-}01 & 0.000E+00 & -4.851E+03 & 4.851E+03 & 0.000E+00 & 0.000E+00 & 0.000E+00 & 0.000E+00 & 0.000E+00 \\
-2.197E\text{-}06 & 3.333E\text{-}07 & -1.845E\text{-}01 & -1.101E\text{-}03 & 1.000E+00 & 0.000E+00 & 0.000E+00 & 0.000E+00 & 0.000E+00 \\
4.191E\text{-}06 & -2.584E\text{-}13 & -1.250E+01 & 0.000E+00 & -2.035E\text{-}02 & 0.000E+00 & 0.000E+00 & 0.000E+00 & 0.000E+00 \\
0.000E+00 & 0.000E+00 & 0.000E+00 & 0.000E+00 & 0.000E+00 & 0.000E+00 & 0.000E+00 & 0.000E+00 & 0.000E+00 \\
\hline
2.165E\text{-}23 & 3.616E\text{-}24 & 5.094E\text{-}19 & 0.000E+00 & 0.000E+00 & -1.014E\text{-}01 & 6.198E\text{-}03 & 3.606E\text{-}02 & -9.994E\text{-}01 \\
0.000E+00 & 0.000E+00 & 0.000E+00 & 0.000E+00 & 0.000E+00 & 0.000E+00 & 0.000E+00 & 1.000E+00 & 2.138E\text{-}01 \\
-5.020E\text{-}21 & 7.888E\text{-}22 & 1.324E\text{-}16 & 0.000E+00 & 0.000E+00 & -2.300E+00 & 0.000E+00 & -2.737E\text{-}02 & 3.306E\text{-}02 \\
2.838E\text{-}21 & -4.466E\text{-}22 & -8.166E\text{-}17 & 0.000E+00 & 0.000E+00 & 5.095E\text{-}01 & 0.000E+00 & 3.057E\text{-}03 & -2.406E\text{-}02
\end{array}\right]$$

$$B = \begin{bmatrix}
3.692E+01 & -2.935E\text{-}03 & 0.000E+00 & 1.585E\text{-}03 \\
0.000E+00 & 0.000E+00 & 0.000E+00 & 0.000E+00 \\
-2.665E\text{-}04 & 6.915E\text{-}05 & 0.000E+00 & 2.378E\text{-}19 \\
0.000E+00 & 0.000E+00 & 0.000E+00 & 0.000E+00 \\
0.000E+00 & 1.839E\text{-}03 & 0.000E+00 & 0.000E+00 \\
0.000E+00 & 0.000E+00 & 9.142E\text{-}09 & 5.622E\text{-}05 \\
0.000E+00 & 0.000E+00 & 0.000E+00 & 0.000E+00 \\
0.000E+00 & 0.000E+00 & -5.635E\text{-}03 & 4.673E\text{-}03 \\
0.000E+00 & 0.000E+00 & 7.183E\text{-}06 & -2.141E\text{-}03
\end{bmatrix}$$

$$C = \begin{bmatrix}
3.415E\text{-}04 & -5.241E\text{-}05 & -1.248E+01 & 0.000E+00 & 0.000E+00 & 0.000E+00 & 0.000E+00 & 0.000E+00 & 0.000E+00 & 0.000E+00 \\
0.000E+00 & 0.000E+00 & 0.000E+00 & 0.000E+00 & 1.000E+00 & 0.000E+00 & 0.000E+00 & 0.000E+00 & 0.000E+00 & 0.000E+00 \\
0.000E+00 & 0.000E+00 & 5.730E+01 & 0.000E+00 & 0.000E+00 & 0.000E+00 & 0.000E+00 & 0.000E+00 & 0.000E+00 & 0.000E+00
\end{bmatrix}$$

$$D = \begin{bmatrix}
0.000E+00 & -1.074E\text{-}02 & 0.000E+00 & -1.074E\text{-}02 \\
0.000E+00 & 0.000E+00 & 0.000E+00 & 0.000E+00 \\
0.000E+00 & 0.000E+00 & 0.000E+00 & 0.000E+00
\end{bmatrix}$$

6.3. Vehicle Dynamic Behavior and Modal Decomposition

The complete set of modes of a GHV are illustrated by modal decomposition using the linear GHV model. Not all nine states in the full A matrix will be needed. The altitude is reduced which does not affect the dynamics. There is also a clear decoupling of the lateral and longitudinal dynamics in this flight condition.

GHV Longitudinal Modes

The MATLAB “eig” function is used to produce the following results. The longitudinal dynamics for the GHV in the steady state pull-up condition at Mach = 5.0 is given by

$$A_{Long} = \begin{bmatrix} \overset{V_T}{-1.6040\times10^{-4}} & \overset{\alpha}{-6.2380\times10^{3}} & \overset{\theta}{-3.1210\times10^{1}} & \overset{Q}{1.9400\times10^{-14}} \\ -2.1970\times10^{-6} & -1.8540\times10^{-1} & -1.1010\times10^{-3} & 1\times10^{0} \\ 0 & 0 & 1\times10^{0} & 0 \\ 4.1910\times10^{-6} & -1.2500\times10^{-6} & 0 & -2.0350\times10^{-2} \end{bmatrix}$$

The four states give rise to two complex-conjugate pairs of eigenvalues, which correspond to two stable oscillatory modes. These eigenvalues are:

Table 9: Longitudinal Modes

Eigenvalue	Damping	Freq. (rad/sec)	Time (sec)	Model
-5.69e-004 + 8.23e-003i	6.90E-02	8.25E-03	7.62E+02	Phugoid
-5.69e-004 - 8.23e-003i	6.90E-02	8.25E-03	7.62E+02	Phugoid
-1.02e-001 + 3.53e+000i	2.90E-02	3.53E+00	1.78E+00	Short-Period
-1.02e-001 - 3.53e+000i	2.90E-02	3.53E+00	1.78E+00	Short-Period

The periods of these modes are separated by more than two orders of magnitude so they are easily identifiable as the short-period and the Phugoid modes.

GHV Lateral-Directional Modes

The MATLAB “eig” function is used to produce the following results. The lateral-directional dynamics for the GHV in the steady state pull-up condition at Mach = 5.0 are given by

$$A_{L-D} = \begin{bmatrix} \overset{\beta}{-1.0140\times10^{-1}} & \overset{\phi}{6.1980\times10^{-3}} & \overset{P}{3.6060\times10^{-2}} & \overset{R}{-9.9900\times10^{-1}} \\ 0 & 0 & 1\times10^{0} & 2.1380\times10^{-1} \\ -2.3000\times10^{0} & 0 & -2.7370\times10^{-2} & 3.3060\times10^{-2} \\ 5.0950\times10^{-1} & 0 & 3.0570\times10^{-3} & -2.4060\times10^{-2} \end{bmatrix}$$

The four states give rise to two complex-conjugated pairs of eigenvalues, which correspond to two stable oscillatory modes. These eigenvalues are:

Table 10: Lateral-Directional Modes

Eigenvalue	Damping	Freq. (rad/sec)	Time (sec)	Mode
-1.85e-002 + 6.81e-003i	9.38E-01	1.97E-02	1.59E+02	Lateral Phugoid
-1.85e-002 - 6.81e-003i	9.38E-01	1.97E-02	1.59E+02	Lateral Phugoid
-5.80e-002 + 7.68e-001i	7.53E-02	7.70E-01	4.08E+00	Dutch Roll
-5.80e-002 - 7.68e-001i	7.53E-02	7.70E-01	4.08E+00	Dutch Roll

Interestingly a lateral Phugoid type mode (a combination of the roll and spiral modes to form a second oscillatory mode) appears in some parts of the flight envelope. The formation of this coupled roll-spiral mode is attributed to the large positive yawing moment due to roll rate (C_{nP}) (see Appendix A), low natural roll damping, and moderate adverse yawing moment due to aileron deflection. A low damped Dutch roll mode is discovered. The vehicle's rudder produces both rolling and yawing moments, and a rudder pulse may excite this mode.

6.4. Summary

In this chapter, the 6-DOF equations of motion for the GHV using the results from Chapters 2 through 5 are developed. The nonlinear equations are linearized and the linear model of the GHV for LTI control purposes is generated. The linear model can be used for a variety of control and navigation research problems. The linearization process is computerized and can be done efficiently at any other trim point throughout the trajectory. The nonlinear equations of motion can be used for more advanced control law development and verification efforts.

Chapter 7: Summary and Conclusions

This research develops the six degrees of freedom (6-DoF) modeling and simulation of a generic hypersonic vehicle including a ramjet/scramjet propulsion system and an aerodynamic database. The mathematical models of the vehicle's aerodynamics and propulsion system are implemented within a conceptual design frame. The integrated aero-propulsion model is the first published analytical model for a generic hypersonic vehicle that includes regenerative cooling effects. The propulsion system model is applicable to hypersonic missiles, manned aircraft, unmanned aerial vehicle systems and access-to-space systems. The experimental investigation of the aerodynamic characteristics of the cone-shaped body configuration is used as the core of the aerodynamic model. The gaps within the wind tunnel data are filled using the best available CFD results. The model is built from aerodynamic, propulsion, atmospheric, and mathematical modules. The modular structure of the simulation helps to change any module efficiently according to the design criteria. The linear model of the GHV is developed, and it can be used for controls and navigation research. The linearized model of the generic hypersonic vehicle includes all pertinent lateral-directional states. This is the exception to published hypersonic vehicle models in the open lecture. The combined longitudinal and lateral-directional models of the GHV can be used for controls and navigation research. The developed aerodynamic and propulsion systems for the GHV allow a trajectory to be optimized for the vehicle.

Chapter 8: Recommendations and Future Work

Aerodynamic heating and skin friction are very important aspects of hypersonic aerodynamics. This research did not cover aerodynamic heating and skin friction effects. In future research, it is highly recommended to use CFD codes capable of solving for viscous flow. The underbody geometry and the configuration of the vehicle needed to be optimized. The amount of air captured by the inlet or spilled out is a direct function of the cowl's position. The optimized configuration minimizes the loss of air at the inlet at hypersonic speeds. Using a 3-D numerical simulation of the flow can improve the accuracy of the simulation. Studies of sidewall and compression inlets are essential for a successful aero-propulsive system design. The low performance of ramjet engines at low speeds demonstrates the importance of research on rocket based and turbojet base combined cycle engines. The performance problem of hypersonic propulsion systems can partially be addressed by reducing the ramjet take-over flight Mach number. In the combustion chamber, improved axial mixing "efficiency" and swirled injection fuel nozzle can increase the mixing rate dramatically. In this research, optimization techniques are applied only to the supersonic-hypersonic portion of the flight trajectory. Trajectory design for the re-entry phase is another research subject. Materials and structures are two major areas where intensive research need to be done. Hypersonic vehicles impose distinctive challenges to GNC. The next generation of guidance and control algorithms must address these challenges. In particularly GNC algorithms with applicability to multi-mission/multiple-Mach regimes are required.

References

[1] Dr. Schweikart, Larry, “The Hypersonic Revelution, Vol. II & III,” Air Force History and Museums Program, Bolling AFB, DC 20332-1111, 1998.

[2] http://www.nasa.gov/ (January 19,2007)

[3] http://www.pr.afrl.af.mil/ (January 19, 2007)

[4] Chavez, F., and Schmidt, D., “Analytical Aeropropulsive/Aeroelastic Hypersonic Vehicle Model with Dynamic Analysis,” Journal of Guidance, Control, and Dynamics, Vol. 17, No. 6, Nov.–Dec. 1994, pp. 1308–1319.

[5] Bolender, Michael A., and Doman, David B., “Nonlinear Longitudinal Dynamical Model of an Air-Breathing Hypersonic Vehicle,” JOURNAL OF SPACECRAFT AND ROCKETS Vol. 44, No. 2, March–April 2007.

[6] Zipfel, Peter H., “Modeling and Simulation of Aerospace Vehicle Dynamics,” AIAA Educational Series, 2000.

[7] Shaughnessy, John D., Pinckney S. Zane, McMinn, John D., Cruz, Christopher I., and Kelley, Marie-Louise, “Hypersonic Vehicle Simulation Model, Winged-Cone Configuration,” NASA Technical Memorandum 102610, NASA Langley, 1991.

[8] Pelham, Phillips, W., Brauckmann, Gregory J., Mico, John R. and, Woods, William C., “Experimental Investigation of the Aerodynamic Characteristics for a Winged-Cone Concept,” NASA Langley Research Center, 1987.

[9] Choi, Sang Bum, “Investigation of the Aerodynamic Characteristics of the Generic Hypersonic Vehicle, Winged-Cone Configuration, by STARS CFD Codes,” MFDCLAB, Los Angeles, California, 2005.

[10] Pelham, Phillips, W., Brauckmann, Gregory J., and Woods, William C. “Experimental Investigation of the Aerodynamic Characteristics for a Winged-Cone Concept,” AIAA 87-49098.

[11] Hayes, W. D., “Linearized Supersonic Flow,” North America Aviation, Inc. Report No. AL-222, 1947.

[12] Hayes, W. D., and Probstein, R. F., “Hypersonic Flow Theory, Academic Press, 1959.

[13] Whitcomb, Richard T., “A Study of the Zero-Lift Drag-Rise Characteristics of Wing-Body Combinations Near the Speed of Sound,” NACA Report 1273, 1956.

[14] Gupta, K. K., “STARS-A General-Purpose Finite Element Computer Program for Analysis of Engineering Structure,” NASA reference publication 1129, 1984.

[15] Gupta, K. K., “STARS—An Integrated, Multidisciplinary, Finite-Element, Structural, Fluids, Aeroelastic, and Aeroservoelastic Analysis Computer Program,” NASA Technical Memorandum 4795, 1997.

[16] Coleman, T. F., and Li, Y., "An Interior, Trust Region Approach for Nonlinear Minimization Subject to Bounds," SIAM Journal on Optimization, Vol. 6, pp. 418-445, 1996.

[17] Coleman, T. F., and Li, Y., "On the Convergence of Reflective Newton Methods for Large-Scale Nonlinear Minimization Subject to Bounds," Mathematical Programming, Vol. 67, Number 2, pp. 189-224, 1994.

[18] Heiser, William H., and Pratt, David T., “Hypersonic Airbreathing Propulsion,” AIAA, 1994.

[19] Farokhi, Saeed, “Airbreathing Jet Engines,” Aerospace Engineering Department, The University of Kansas, Lawrence, Kansas, 2005.

[20] Curran, E. T., and Stull, F. D., “The Utilization of Supersonic Combustion Ramjet Systems at Low Mach Number,” Aero Propulsion Laboratory, RTD-TDR63-4097, January 1964.

[21] Waltrup, P. J., “The Dual Combustor Ramjet; a Versatile Propulsion System for Hypersonic Tactical Missile Application,” AGARD Conf. Proc. 526, 1992.

[22] Sutton, George P., and Biblarz, Oscar, “Rocket Propulsion Elements,” John Wiley & Sons, Inc., 2001.

[23] Kerrebrock, J. L., “Aircraft Engines and Gas Turbines,” The MIT Press, Cambridge, Massachusetts, London, England, 1992.

[24] Leitmann, G., “Optimization Techniques,” Academic Press, 1962.

[25] Robinett, Rush D. III, Wilson, David G., Eisler, G. Richard, and Hurtado, John E., “Applied Dynamic Programming for Optimization of Dynamical Systems,” SIAM, 2005.

[26] Bryson, Arthur. E., “Dynamic Optimization,” Addison-Wesley, 1999.

[27] Lewis, Frank L., and Stevens, Brian L., “Aircraft Control and Simulation,” Wiley, 1992.

[28] Roskam, Jan, “Airplane Flight Dynamics and Automatic Flight Control, Part I,” DAR Corporation, 1997.

[29] Blakelock, John H., “Automatic Control of Aircraft and Missiles,” Wiley, 1991.

[30] Dierckx, Paul, “Curve and Surface Fitting with Splines,” Oxford University, 1995.

[31] Philip, George, “Numerical Methods of Curve Fitting,” Cambridge [Eng.] University Press, 1961.

[32] Keshmiri, S., Colgren R. D., and Mirmirani, M., “Development of an Aerodynamic Database for a Generic Hypersonic Air Vehicle,” AIAA 2005-35352.

[33] Keshmiri, S., Mirmirani, Maj D., and Colgren, Richard, “Six-DOF Modeling and Simulation of a Generic Hypersonic Vehicle for Conceptual Design Studies,” AIAA-2004-4805, August 2004.

[34] Tauber, M. E., and Menees, G. P., “Aerothermodynamics of Transatmospheric Vehicles,” AIAA paper n086-1257, 1987.